Study of the reactivity of radical species of peroxyl type of atmospheric interest

Mirna Shamas

THÈSE

Présentée à

L'Université de Lille

Laboratoire de PhysicoChimie des Processus de Combustion et de l'Atmosphère

En vue de l'obtention du grade de

Docteur de l'Université de Lille

École Doctorale des Sciences de la Matière, du Rayonnement

et de l'Environnement

Par

Mirna Shamas

Study of the reactivity of radical species of peroxyl type of atmospheric interest
Etude de la réactivité d'espèces radicalaires de type peroxyle d'intérêt atmosphérique

Thèse préparée et soutenue publiquement le 14 Octobre 2022 devant la commission d'examen composée de :

Terry Dillon	Professeur, University of York - Department of Chemistry	Rapporteur
Estelle Roth	Maître de conférences, Université de Reims - GSMA	Rapporteure
Max R. Mc Gillen	Chargé de recherche, ICARE Orléans	Examinateur
Emmanouil Romanias	Maître de conférences, IMT Nord Europe - CERI EE	Examinateur
Denis Petitprez	Professeur, Université de Lille - PC2A	Président de jury
Laure Pillier	Chargée de recherche, Université de Lille - PC2A	Directrice de thèse
Christa Fittschen	Directrice de recherche, Université de Lille - PC2A	Co-directrice de thèse

Acknowledgements

I would like first to thank my supervisor Laure Pillier for her guidance, help, and patience throughout my PhD. I deeply appreciate her support as well as her advice and encouragement to be better each time. I would like also to thank my co-supervisor, Christa Fittschen. I am extremely grateful for everything she has taught me, it has been a pleasure working with her. Many thanks to Coralie Schoemaecker for her kindness, advices, and encouragement.

My sincere thanks to the members of the jury: Denis Petitprez, Terry Dillon, Estelle Roth, Max R. McGillen and Emmanouil Romanias for accepting to evaluate this thesis work. Their remarks and comments added value to my manuscript.

I would like to thank Benjamin Hanoune, director of the PC2A laboratory, as well as all the technical and administrative staff of the laboratory who allowed me to work in very good conditions. Many thanks to Sebastien and Amaury for their help.

I would like also to thank the members of CERLA, especially Benedicte for her help and kindness. I deeply appreciate her support.

I would like to deeply thank my colleagues and friends in the lab. Thanks to Mohamed, Mona, Florent, Cuihong and Chuanliang for their help, continuous support and for the good friendly times we have spent together. Also thanks a lot to my friends Khaled and Mikel.

My greatest thanks go to my dear sister Nesrine who was beside me during these three years, who was my friend, my colleague in the lab and my true supporter. Thanks for everything!

It is a privilege to express my sincere appreciation to all my family members especially my brothers Hussien, Mohamad, Hasan, Abbas and my beloved sister Layal and my brother-in-law Ali who showed me endless love and support. Finally, if add up all the expressions showing appreciation, gratitude and thankfulness they will never be enough to thank my parents for their great sacrifices.

Table of Contents

List of Figures

List of Tables

Introduction

Air pollution has long been considered as one of the biggest global health and environmental challenges. It ranks among the top risks for mortality as it accounts for 7 million deaths each year from exposure to ambient and household air pollution (WHO). Along with harming human health, air pollution is affecting the environment because of its contribution to smog conditions, acid rain, stratospheric ozone depletion and global warming climate change. These consequences on the environment and the human health cause the air pollution to be a major issue that needs to be tackled at a global level through legislation and international agreements such as Paris Agreement of 2015. These agreements aim to limit global warming and are based on complex climate models that aim to predict the future of the climate. These models are based on various physical and chemical processes occurring in the atmosphere. In order to improve these models and develop optimum strategies to deal with these global challenges, it is necessary to observe the atmospheric constituents and to understand their transformation by chemical reactions through experimental work carried out in the laboratory.

The atmospheric oxidation reactions are initiated by the hydroxyl radical (OH) which reacts with almost all of the volatile organic compounds (VOCs) leading to the formation of secondary pollutants. The reactions of the products formed with oxygen leads to the formation of peroxy RO_2 and hydroperoxy HO_2 radicals. These radical species have a short life time (~ 100 s for HO_2) and strongly influence the local environment in which they are generated. While the reactivity of these peroxy radicals is well known in polluted environments (high NO_X concentrations), it is still poorly known in remote environments containing low concentrations of NOx (ex: tropical forests, marine boundary layer). These radicals, RO_2 and HOx (OH and HO_2), react with each other in remote environments, however, very few studies exist on the rate constants of these reactions. Thus, due to the lack of knowledge of these radical reactions, the concentrations of certain species in the atmosphere are not correctly predicted by the models.

The objective of this thesis is to study the kinetics of some of these peroxy radicals to better understand the radical + radical reactions in clean atmosphere. Providing experimental data on such reactions improves the understanding of atmospheric radical chemistry and thus the models for

predicting the climate will be more accurate. Two experimental set-ups have been used in this work:

- A fast discharge flow reactor coupled to three complementary techniques: the continuous-wave Cavity Ring-Down Spectroscopy (cw-CRDS) for the measurement of the HO_2 radical, the Laser Induced Fluorescence (LIF) for the detection of the OH radical and Mass spectrometry with Molecular Beam sampling (MB/MS) for the measurement of stable reaction products and radical species. This fast flow reactor was continued to be developed in the frame of this work to study radical + radical reactions. It was originally designed to complement an existing photolysis cell set-up.

- A laser photolysis cell coupled to a double cw-CRDS paths for the simultaneous measurements of RO_2 and HO_2 radicals was used to study the $C_2H_5O_2$ self-reaction.

This manuscript is divided into four chapters:

Chapter 1 provides a general description of the atmosphere and the radical chemistry in the troposphere with a focus on the reactions involving peroxy radicals in a clean environment. Furthermore, experimental techniques for carrying out kinetic studies for radical reactions is also described.

Chapter 2 describes in detail the principle of the experimental techniques used: Laser Induced Fluorescence (LIF), continuous wave-Cavity Ring Down Spectroscopy (cw-CRDS), and Mass Spectrometry analysis associated with Molecular Beam (MB/MS). A description of the fast flow reactor and the photolysis cell is also presented.

Chapter 3 presents a summary of the previous work done during the PhD of Florent Kravtchenko to validate the recently developed experimental set-up consisting of a fast flow reactor coupled to LIF, cw-CRDS, and MB/MS. During the validation of this set-up, an unexplained OH re-formation phenomenon was disturbing the kinetic measurements of the rate constants of well-known reactions between OH radicals and stable species (propane, ethane, methanol). At the end of Florent Kravtchenko's PhD, some answers have been given but questions remain, we have tried to answer them during my PhD. This section will therefore display the different further tests carried out to explain the OH re-formation phenomenon done during my PhD work.

Chapter 4 concerns the kinetic and the spectroscopic study of the ethyl peroxy radical using the laser photolysis cell coupled to a double cw-CRDS paths. The results obtained include: absorption cross-section of the $C_2H_5O_2$ radical by two different approaches, absorption spectrum of $C_2H_5O_2$ radical, rate constant and branching ratios of the $C_2H_5O_2$ self-reaction.

Chapter 1: Bibliographic Study and Detection Techniques for Radical Chemistry Studies

The first chapter highlights the motivations that led to the study of the radical chemistry in a clean environment. First, a general description of the atmosphere and the radical chemistry in the troposphere is provided. Then, the reactions involving peroxy radicals in a clean environment are detailed. Experimental techniques for carrying out kinetic studies for radical reactions is also described.

1.1. Bibliographic study on radical reactions in the troposphere

1.1.1. Structure of the atmosphere

The atmosphere is a layer composed of mainly gas constituents that surrounds the Earth. It is made up of different layers: the troposphere, stratosphere, mesosphere, thermosphere, and the exosphere (Seinfeld & Pandis, 2016). These layers are divided according to the variation of the average temperature profile with altitude, as shown in Figure 1.

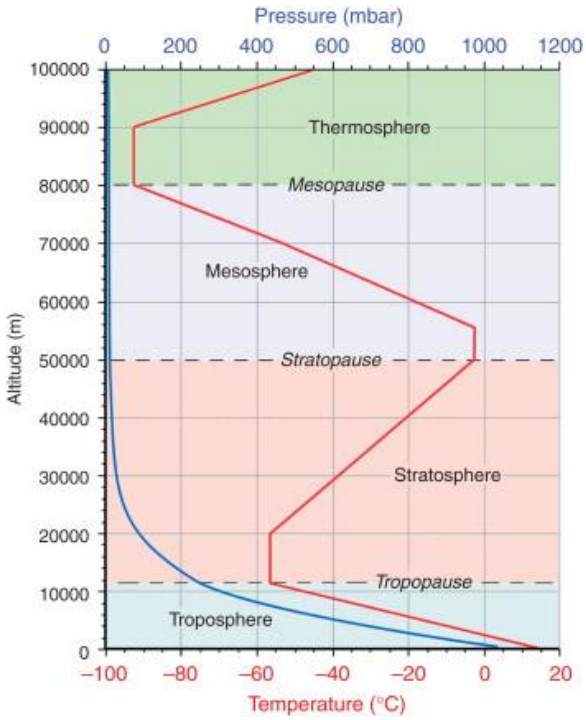

Figure 1: Schematic representation of the different layers of the atmosphere (Kambezidis, 2012)

The troposphere is the lowest layer of the atmosphere extending from the earth's surface up to an altitude of 15 km. This layer is characterized by decreasing temperature with height (about 6.5 °C / km) until the tropopause, the boundary layer between the troposphere and the stratosphere, where the temperature stabilizes. The stratosphere extends from the tropopause to the stratopause (around 50 km altitude) which is the boundary layer between the stratosphere and the mesosphere. In this layer, the temperature increases with altitude due to the absorption of the solar UV radiation by the stratospheric ozone and the formation of ozone. The mesosphere extends from the stratopause to the mesopause (around 80-90 km altitude) which is the boundary layer between the mesosphere and the thermosphere. In this layer, the temperature decreases with altitude reaching a temperature of -100 °C at the mesopause. The thermosphere extends from the mesopause to the thermopause (around 640 km altitude) which is the boundary layer between the thermosphere and the exosphere. It is characterized by high temperature due to the absorption of the solar UV radiation. The exosphere is the outermost layer of the atmosphere and extends up to several thousand kilometers. In this layer, the gaseous molecules with sufficient energy can escape from the Earth's gravitational attraction.

The Earth's atmosphere is composed of 78.1% N_2, 20.9% O_2, 0.93% Ar and 0.04% CO_2. Water vapor, which is the next most ambient constituent, is variable and can reach up to 3% of the composition of the atmosphere. The remaining gas constituents, called trace gases, are composed of volatile compounds with concentrations below 0.1%. These trace gases are either of biogenic origin emitted from sources such as forests and oceans or of anthropogenic origin emitted from human activities. After being released in the atmosphere, these trace gases can be transformed or removed by different processes such as wet or dry deposition, transport or chemical transformation. For example, chemical oxidation controls the atmospheric lifetime of certain greenhouse gases, in particular methane. The chemical aging of particles and gases through oxidation and photolysis can enhance the production of aerosols and toxic products. Thus, it is important to explore the oxidative species and reactions in the atmosphere in order to develop the modeling of atmospheric chemistry and to better predict the evolution of the oxidizing capacity of the atmosphere.

1.1.2. Radical chemistry in the troposphere

Hydroxy OH, hydroperoxy HO_2, and peroxy RO_2 radicals play a key role in atmospheric chemistry. Investigating the processes of formation and consumption of these radical species is important in order to understand the current pollution phenomena.

Peroxy radicals RO_2 (with R= H, CH_3, C_2H_5, …) are intermediate species formed from the oxidation processes of Volatile Organic Compounds (VOCs) in the atmosphere. Biogenic and anthropogenic VOCs can be removed in the atmosphere by photolysis or by chemical reactions with other species such as OH radical or to a minor extend with Cl atoms, NO_3 or O_3.

The OH radical plays a very important role in the troposphere where it is considered to be the main oxidant. The concentration of the OH radical controls the level of species contributing to global warming or the formation of photochemical pollutants. OH radical will oxidize essentially every organic species emitted to form an alkyl radical R, which in the presence of oxygen, will form the peroxy radical RO_2.

A simplified scheme involving reactions between OH, HO_2, and RO_2 radicals in the presence of nitrogen oxides (NOx), is shown in Figure 2. This radical reactivity cycle controls the oxidizing capacity of the atmosphere, and the formation of tropospheric ozone and secondary pollutants (sulfuric and nitric acids, peroxyacetyl nitrates (PAN), particles, secondary organic aerosols (SOA), etc…).

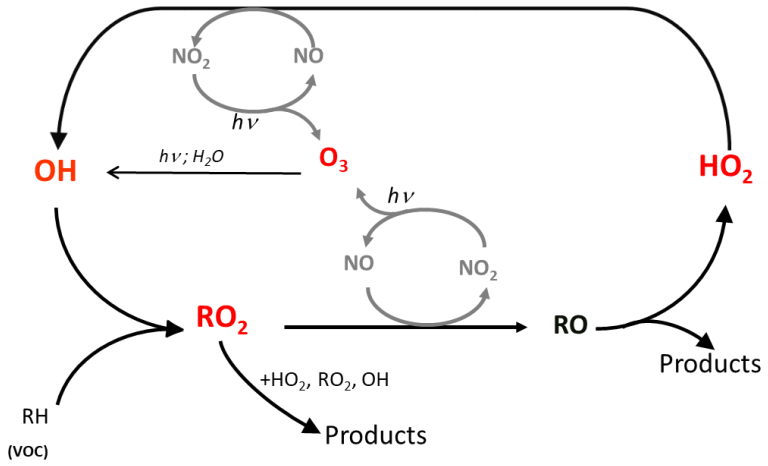

Figure 2: Simplified radical reactivity cycle in the atmosphere

The tropospheric chemistry of OH, HO_2, and RO_2 radicals has been widely described in the literature, in particular in several review articles (Jenkin et al., 2019; Orlando & Tyndall, 2012). The main source of daytime OH radical is through the photolysis of ozone O_3 ($\lambda < 310$ nm) to form an excited oxygen atom $O(^1D)$ that reacts with water vapor to form OH.

$$O_3 + h\upsilon_{<310nm} \rightarrow O(^1D) + O_2(^1\Delta g) \quad \text{(R 1)}$$

$O(^1D)$ atoms are quenched by collisions with other molecules M, which are mostly N_2 and O_2 in the atmosphere.

$$O(^1D) + M \rightarrow O(^3P) + M \quad \text{(R 2)}$$

Quenching of $O(^1D)$ atoms is in direct competition with its reaction with water. About 10% of the produced $O(^1D)$ reacts with water in the lower troposphere where the water mixing ratio is 1.5% (Showman & Dowling, 2014) to form two OH radicals, and the $O(^3P)$ will react with O_2 to recycle O_3.

$$O(^1D) + H_2O \rightarrow 2\ OH \quad \text{(R 3)}$$

$$O(^3P) + O_2 \rightarrow O_3 \quad \text{(R 4)}$$

The formation of the OH radical exists in other pathways such as the photolysis of nitrous acid HONO (R 5). As well, OH radicals can be formed from the photolysis of hydrogen peroxide H_2O_2 (R 7) that is formed from HO_2 (R 6.

$$HONO + h\upsilon_{<400nm} \rightarrow OH + NO \quad \text{(R 5)}$$

$$HO_2 + HO_2 \rightarrow H_2O_2 + O_2 \quad \text{(R 6)}$$

$$H_2O_2 + h\upsilon_{<360nm} \rightarrow 2\ OH \quad \text{(R 7)}$$

Then, various reaction pathways exist for OH radicals including the reactions with CO to form HO_2 and, as mentioned before, the reactions with VOCs to form RO_2 radicals.

$$OH + CO + O_2 \rightarrow HO_2 + CO_2 \quad \text{(R 8)}$$

$$OH + RH + O_2 \rightarrow RO_2 + H_2O \quad \text{(R 9)}$$

The main sink for the OH radical in polluted environments comes from the reaction with NO_2 resulting in the production of nitric acid HNO_3.

$$OH + NO_2 + M \rightarrow HNO_3 + M \quad \text{(R 10)}$$

OH and HO_2 radicals have a short lifetime in the atmosphere with ~ 1 s and ~ 100 s respectively due to their high reactivity. Their chemistry does not involve transport and their concentrations rely on the chemical composition and the balance between sources and sinks in the local environment. Thus, the concentrations of OH and HO_2 radicals in the troposphere alter with location and weather conditions. The concentrations of OH range from 10^5 to 10^7 molecules cm^{-3}, while those of HO_2 range from 10^7 to 10^8 molecules cm^{-3}. The $[HO_2]$ / [OH] ratio is a crucial parameter for quantifying the oxidizing capacity of the atmosphere, i.e. the amount of OH available to initiate the oxidation reactions with many VOCs.

The formed RO_2 radicals can be consumed by various reaction pathways depending on the concentration of NOx (NO and NO_2).

In polluted environments, areas that are "NOx-saturated" with respect to the production of oxidants, in particular ozone (Wennberg, 2013), RO_2 radicals react predominantly with NO forming NO_2. Then, the photolysis of NO_2 will lead to the formation of O_3.

$$RO_2 + NO \rightarrow RO + NO_2 \quad \text{(R 11)}$$

The alkoxyl radical RO formed will react with O_2 in the atmosphere to form the molecule $R_{-H}=O$ (where R_{-H} is the radical R with one H less), and the hydroperoxyl radical HO_2, which in the presence of NO reforms the OH radical (see Figure 2).

$$HO_2 + NO \rightarrow OH + NO_2 \quad \text{(R 12)}$$

$$RO + O_2 \rightarrow R_{-H}=O + HO_2 \quad \text{(R 13)}$$

In clean atmospheres, areas with low NOx concentrations, another case exists for the consumption pathway of the RO_2 radicals. Areas with low NOx concentrations are regions far from all human activities such as tropical forests, or the marine boundary layer. In these regions, the RO_2 radicals will react preferentially with other RO_2 radicals (including HO_2) and OH radical. RO_2 radicals can also undergo other phenomena such as isomerization, photolysis or even heterogeneous reactions. RO_2 and HO_2 radicals will be able to follow termination reactions leading to stable products like the alkyl hydroperoxide ROOH and the hydrogen peroxide H_2O_2 or the alkoxyl radical RO.

$$RO_2 + RO_2 \rightarrow 2\ RO + O_2 \quad \text{(R 14)}$$

$$HO_2 + HO_2 \rightarrow H_2O_2 + O_2 \quad \text{(R 15)}$$

$$RO_2 + HO_2 \rightarrow ROOH + O_2 \quad \text{(R 16)}$$

$$HO_2 + OH \rightarrow H_2O + O_2 \quad \text{(R 17)}$$

1.1.3. Radical chemistry in a clean atmosphere

1.1.3.1. $RO_2 + HO_2$ reactions

The reactions between RO_2 and HO_2 radicals are considered to be an important sink process for organic peroxy radicals in the troposphere. Although this reaction is typically supposed to generate hydroperoxides ROOH as a major product which is considered to be a stable species in the troposphere, other studies show that these reactions can lead also to three different reaction pathways (Hasson et al., 2012):

$$RO_2 + HO_2 \rightarrow ROOH + O_2 \quad \text{(R 18a)}$$

$$RO_2 + HO_2 \rightarrow ROH + O_3 \quad \text{(R 18b)}$$

$$RO_2 + HO_2 \rightarrow RO + OH + O_2 \quad \text{(R 18c)}$$

The pathway (R 18c) leads to the production of OH radical, making it possible to initiate new radical reactions (propagation process). Therefore, knowledge in the kinetics and mechanisms of such important peroxy radical reactions is essential for understanding the oxidation mechanism of VOCs present in the atmosphere.

The simplest RO_2 radical, methyl peroxy radical CH_3O_2, is formed from the oxidation of tropospheric methane CH_4. It is the dominant peroxy radical in the remote troposphere. The reaction $CH_3O_2 + HO_2$ is well known.

The first measurement of the rate constant between CH_3O_2 and HO_2 was performed using molecular modulation absorption spectroscopy where the radical kinetics was studied by the measurement of the absorption of CH_3O_2 and HO_2 at a fixed wavelength (Cox & Tyndall, 1980). The CH_3O_2 was formed by photolysis of Cl_2 in the presence of CH_4 and O_2 and was measured from absorption in the UV at 250 nm. The HO_2 was formed by the reaction between H_2 + Cl in the presence of O_2 and was measured from absorption at 210 nm. The rate constant of this reaction was determined to be: k (298 K) = 6.5 ± 1.0 × 10^{-12} $cm^3molecule^{-1}s^{-1}$. Other measurements performed by absorption spectroscopy were in agreement with the value mentioned above where

the rate constant was determined to be: k (298 K) = 6.2 ± 1.0 × 10^{-12} $cm^3molecule^{-1}s^{-1}$ (Lightfoot et al., 1990) and k (298 K) = 5.13 ± 0.55 × 10^{-12} $cm^3molecule^{-1}s^{-1}$ (Boyd et al., 2003). However, a value lower by a factor of 2 was mentioned in the literature: k (298 K) = 2.9 ± 0.4 × 10^{-12} $cm^3molecule^{-1}s^{-1}$ (Dagaut et al., 1988a). The difference comes from the values of the absorption cross-sections of CH_3O_2 and HO_2 used by the various authors, which have a direct influence on the measurement of the rate constant. Another measurement for the rate constant was performed using the turbulent flow technique with a chemical ionization mass spectrometry (CIMS) detection system (Raventos-Duran et al., 2007a). In this case, the CH_3O_2 radical was generated by the reaction of F with CH_4 in the presence of O_2, and the HO_2 radical was formed by the reaction of H with O_2. The H and F atoms were formed by the dissociation of H_2 and F_2 using a microwave discharge.

For the CH_3O_2 + HO_2 reaction, the two different reaction pathways are:

$$CH_3O_2 + HO_2 \rightarrow CH_3OOH + O_2 \quad \text{(R 19a)}$$

$$CH_3O_2 + HO_2 \rightarrow HCHO + O_2 + H_2O \quad \text{(R 19b)}$$

The values in the literature agree on the predominance of the pathway (R 19a) as a major reaction pathway with a yield of 92% (Wallington & Japar, 1990a).

Ethane is one of the most abundant non-methane hydrocarbons, and its atmospheric oxidation leads to the formation of the ethyl peroxy radical, $C_2H_5O_2$. There are several measurements for the rate constant of $C_2H_5O_2$ + HO_2.

The first measurement of the rate constant between $C_2H_5O_2$ and HO_2 was performed in a photolysis cell (Cattell et al., 1986). The $C_2H_5O_2$ and HO_2 radicals were generated simultaneously by photolysis of Cl_2 in the presence of C_2H_6-CH_3OH-O_2-N_2 mixture. The $C_2H_5O_2$ was measured from absorption in the UV at 260 nm, and the HO_2 was measured at 210 nm or in the mid-infrared at 1117 cm^{-1}. The rate constant of this reaction was determined to be: k (298 K) = 6.3 ± 0.9 × 10^{-12} $cm^3molecule^{-1}s^{-1}$. Other measurements were performed in an absorption photolysis cell where the rate constant was determined to be: k (298 K) = 5.3 ± 1.0 × 10^{-12} $cm^3molecule^{-1}s^{-1}$ (Dagaut et al., 1988b), k (298 K) = 5.1 × 10^{-12} $cm^3molecule^{-1}s^{-1}$ (Noell et al., 2010), k (298 K) = 7.27 × 10^{-12} $cm^3molecule^{-1}s^{-1}$ (Maricq & Szente, 1994), k (298 K) = 8.14 x 10^{-12} $cm^3molecule^{-1}s^{-1}$ (Boyd et al., 2003), and k (298 K) = 1.10 ± 0.21 × 10^{-11} $cm^3molecule^{-1}s^{-1}$ (Fenter et al., 1993). The difference between these values may also be due to the difference in the value of the absorption cross-sections

of $C_2H_5O_2$ and HO_2. Another measurement for the rate constant was performed using the turbulent flow technique with CIMS detection system (Raventós-Duran et al., 2007b) where the rate constant obtained was: k (298 K) = 4.0 ± 0.6 × 10^{-12} $cm^3molecule^{-1}s^{-1}$. Despite several measurements of the rate constant of $C_2H_5O_2$ + HO_2, there is no good agreement of this rate constant in the literature which motivates this study.

For the $C_2H_5O_2$ + HO_2 reaction, the two different reaction pathways are:

$$C_2H_5O_2 + HO_2 \rightarrow C_2H_5OOH + O_2 \quad \text{(R 20a)}$$

$$C_2H_5O_2 + HO_2 \rightarrow CH_3CHO + O_2 + H_2O \quad \text{(R 20b)}$$

As for the reaction of CH_3O_2 + HO_2, the data in the literature agree on the predominance of the pathway (R 20a) as a major reaction pathway leading to the formation of C_2H_5OOH. The use of FTIR allows the direct measurement of products that makes it possible to determine the branching ratios of the two pathways. Using this method, the yield of the pathway (R 20a) was determined to be 102 ± 6% (Wallington & Japar, 1990b), and it was validated twice using the same method (Hasson et al., 2004; Spittler et al., 2000).

For alkyl radicals containing more than two carbon atoms: $C_3H_7O_2$ and $C_4H_9O_2$, there is only two theoretical studies (Hou et al., 2005; Johnson et al., 2004). However, these studies do not make it possible to determine the reaction products. The rate constant for $C_3H_7O_2$ + HO_2 at 298 K is 1.72 × 10^{-11} $cm^3molecule^{-1}s^{-1}$ and that for $C_4H_9O_2$ + HO_2 at 298 K is 1.63 × 10^{-11} $cm^3molecule^{-1}s^{-1}$ (Johnson et al., 2004). These values seem very high and should be confirmed for these two radicals.

Thus, the reaction for simple RO_2 radicals with HO_2 mainly leads to the formation of the hydroperoxide species ROOH. However, contradictory results were observed concerning the branching ratios of the different pathways in the case of more complex RO_2 radicals, in particular carbonyl radicals presenting a double bond C=O.

The simplest carbonyl RO_2 radical, namely the acetyl peroxy radical $CH_3C(O)O_2$, is an important species in the atmosphere resulting from the degradation and oxidation of several VOCs. The $CH_3C(O)O_2$ radical can be formed by various pathways, one of which is the oxidation of methyl

vinyl ketone (MVK) (Tuazon & Atkinson, 1989). This radical can be also formed by the thermal decomposition of peroxyacetyl nitrate (PAN) (Groß et al., 2014).

In a clean environment, the reaction between $CH_3C(O)O_2$ and HO_2 is important, and leads to three reaction pathways:

$$CH_3C(O)O_2 + HO_2 \rightarrow CH_3C(O)O_2H + O_2 \quad \text{(R 21a)}$$

$$CH_3C(O)O_2 + HO_2 \rightarrow CH_3C(O)OH + O_3 \quad \text{(R 21b)}$$

$$CH_3C(O)O_2 + HO_2 \rightarrow CH_3C(O)O + OH + O_2 \quad \text{(R 21c)}$$

The pathway (R 21c) leads to the formation of OH radical which can initiate the further oxidation of volatile organic trace gases. This pathway also leads to the formation of $CH_3C(O)O$ which can rapidly decompose into CH_3 and CO_2 where CH_3 in the presence of O_2 can lead to the formation of a new CH_3O_2 radical (Groß et al., 2014). Thus, this pathway is radical-propagating and sustains the oxidation capacity of the atmosphere. Therefore, it is important to know the overall rate constant and the branching ratios for these three reaction channels.

The first measurement of the rate constant between $CH_3C(O)O_2$ and HO_2 was performed in a photolysis cell (Moortgat et al., 1989). The $CH_3C(O)O_2$ and HO_2 radicals were generated by flash photolysis of Cl_2-CH_3CHO-CH_3OH-O_2-N_2 mixture. The $CH_3C(O)O_2$ and HO_2 were measured from absorption in the UV at 270 nm and 210 nm respectively. The rate constant of this reaction was determined to be: k (298 K) = $1.3 \pm 0.3 \times 10^{-11}$ $cm^3molecule^{-1}s^{-1}$. This study showed that this reaction leads only to the first two reaction pathways (R 21a) and (R 21b) and the branching ratio for channel (R 21b) was 0.33 ± 0.07. The branching ratio was in good agreement with Niki et al. (Niki et al., 1985) who determined for this reaction the product distribution by FTIR and estimated 75% and 25% for the yields of reactions (R 21a) and (R 21b) respectively. Other measurements for the branching ratios also demonstrated that the reaction (R 21a) lead only to the first two reaction pathways (Crawford et al., 1999; Horie & Moortgat, 1992; Orlando et al., 2000). However, other experimental and theoretical studies showed the importance of the reaction pathway (R 21c) leading to the formation of OH (Hasson et al., 2004).

In the experimental study done by Hasson et al. (Hasson et al., 2004), the radical species were created by the photolysis of a mixture of synthetic air, acetaldehyde, methanol, and Cl_2 in a

simulation chamber at 800 Torr and 298 K. The stable species formed during the reaction were measured using a combination of long-path Fourier Transform Infrared Spectroscopy (FTIR) and High-Performance Liquid Chromatography (HPLC) with fluorescence detection. The best fit of the kinetic modeling with the experimental data determines a branching ratio for the channel (R 21c) of 0.40 ± 0.16 corresponding to an overall rate constant k (298 K) = 2.2×10^{-11} $cm^3molecule^{-1}s^{-1}$. However, other reproducible experimental data determined a branching ratio for channel (R 21c) of 0.3 and a rate constant k (298 K) = 1.4×10^{-11} $cm^3molecule^{-1}s^{-1}$. This method has been improved by adding benzene C_6H_6 to the reaction medium in order to scavenge the OH radicals formed, and thus detect the phenol C_6H_5OH used as a primary diagnostic for OH radical formation (Jenkin et al., 2007). This reaction yields a branching ratio of 0.43 ± 0.10 for the channel (R 21c) corresponding to k (298 K) = 1.4×10^{-11} $cm^3molecule^{-1}s^{-1}$. Using the same method, Le Crâne et al. (Le Crâne et al., 2006) showed a much lower value of the branching ratio for the pathway leading to the formation of OH (< 0.1). This difference was explained by Jenkin et al. (Jenkin et al., 2007) by the fact that the kinetics of HOC_6H_6 radical formed from the reaction between benzene and OH was not properly taken into account and this underestimates the importance of channel (R 21c).

The first direct observation of OH as a product of the $CH_3C(O)O_2 + HO_2$ reaction was performed by Dillon and Crowley (Dillon & Crowley, 2008) using pulsed laser photolysis coupled with Laser Induced Fluorescence (PLP-LIF). The rate constant of this reaction is k (298 K) = $1.4 \pm 0.5 \times 10^{-11}$ $cm^3molecule^{-1}s^{-1}$ and the value of the branching ratio of the channel (R 21c) was 0.50 ± 0.20. Another measurement for the branching ratio of the pathways (R 21b) and (R 21c) was done using a combination of laser induced fluorescence (LIF) for the measurement of OH concentration and a transient absorption spectroscopy (TAS) technique for the measurement of O_3 concentration (Groß et al., 2014). A higher branching ratio for the channel (R 21c) was obtained: 0.61 ± 0.09 at 298 K and pressure independent. As well, the reaction $CH_3C(O)O_2 + HO_2$ was studied in a series of experiments conducted at 750 Torr and 293 K in the HIRAC simulation chamber (Winiberg et al., 2016). For the first time, the three reaction pathways were measured directly and simultaneously by using LIF-based FAGE instrument (Fluorescence Assay by Gas Expansion), FTIR and UV photometric O_3 analyzer. The results yield the following branching ratios: (R 21a) = 0.37 ± 0.10, (R 21b) = 0.12 ± 0.04 and (R 21c) = 0.51 ± 0.12. Recently, Hui et al. (Hui et al., 2019) studied the branching ratio leading to the formation of OH in a photolysis cell at 100 Torr and between 230

and 298 K. IR and UV absorption spectroscopy were used to detect directly HO_2, OH and CH_3O_2 radicals. The result of this study yields a branching ratio of 0.48 ± 0.09 at 294 K.

Thus, the value of the rate constant of (R 21) in the literature data vary between $1.4 \pm 0.5 \times 10^{-11}$ $cm^3molecule^{-1}s^{-1}$ and $2.4 \pm 0.4 \times 10^{-11}$ $cm^3molecule^{-1}s^{-1}$ where the value recommended by the IUPAC committee is $2.0 \pm 0.2 \times 10^{-11}$ $cm^3molecule^{-1}s^{-1}$ at 298 K. The values of the branching ratio of the pathway (R 21c) vary according to the authors between 0.1 and 0.6. Taking into account the last four studies to date, for which the OH was measured directly, the values seem to agree with the uncertainties between 0.4 and 0.6 (Dillon & Crowley, 2008; Groß et al., 2014; Hui et al., 2019; Winiberg et al., 2016).

The reaction between $CH_3C(O)O_2$ and HO_2 is temperature dependent. Taking this reaction into account in a global chemistry model, it has been estimated that it can cause a significant increase in the OH levels in the forested tropical areas up to 11% (Winiberg et al., 2016).

Finally, considering the case of the acetonyl peroxy radical $CH_3C(O)CH_2O_2$ which is formed from the degradation of a large number of emitted VOCs in the troposphere. It is generated directly from the oxidation of acetone, which is both an emitted VOC and a degradation product of several hydrocarbons, including many important monoterpenes. $CH_3C(O)CH_2O_2$ is also predicted to be generated from the breakdown of diverse complex carbonyl compounds, formed as degradation products of long-chain alkanes. Thus, this radical plays a potentially widespread role in atmospheric chemistry (Jenkin et al., 2008).

The reaction between $CH_3C(O)CH_2O_2$ and HO_2 leads to two reaction pathways:

$$CH_3C(O)CH_2O_2 + HO_2 \rightarrow CH_3C(O)CH_2OOH + O_2 \quad \text{(R 22a)}$$

$$CH_3C(O)CH_2O_2 + HO_2 \rightarrow CH_3C(O)CH_2O + OH + O_2 \quad \text{(R 22b)}$$

The first kinetic study for the reaction between $CH_3C(O)CH_2O_2$ and HO_2 was performed in a photolysis cell where the $CH_3C(O)CH_2O_2$ radical was formed via the reaction between Cl atoms and acetone in the presence of oxygen (Bridier et al., 1993). The measurement of the radicals was ensured by UV absorption and a rate constant k (298 K) = $9.0 \pm 1.0 \times 10^{-12}$ $cm^3molecule^{-1}s^{-1}$ was determined. However, this study showed that this reaction leads only to the first reaction pathway (R 22a) forming the associated hydroperoxide $CH_3C(O)CH_2OOH$.

Another study confirmed the formation of $CH_3C(O)CH_2OOH$ and showed that this reaction leads also to pathway (R 22b) where the product yields were measured using a combination of FTIR and HPLC (Hasson et al., 2004). The appearance of pathway (R 22b) was deduced from the observation of the formation of products such as paracetic acid (PAA) $CH_3C(O)OOH$, methyl hydroperoxide CH_3OOH and carbon dioxide CO_2. Indeed, if the pathway (R 22a) was the only possible reaction pathway, these compounds should not be detectable (Hasson et al., 2004). The results showed that the branching ratio for channel (R 22a) was 0.33 ± 0.10 while that for channel (R 22b) was 0.67 ± 0.20. These results suggest that this reaction mainly leads to a propagation path. Thus, this disagrees with the previous study of Bridier et al. arising new studies for this reaction.

Another measurement for the branching ratio of the reaction pathway forming OH (R 22b) was performed in a simulation chamber at 296 K and 700 Torr (Jenkin et al., 2008). The phenol that is formed by adding benzene in the presence of OH was measured by FTIR. The detection of phenol makes it possible to determine the branching ratio of reaction (R 22b) and it was estimated to be 0.15 ± 0.08. A direct measurement for the OH formation was performed using a pulsed laser photolysis system coupled with LIF (Dillon & Crowley, 2008) where the results showed a value of 0.15 ± 0.10. The result of this study was in a good agreement with the value of Jenkin et al. mentioned previously. In 2012, a correction was made to the work of Hasson et al. (Hasson et al., 2004), leading to a new value for the yield of pathway (R 22b) that was 0.25 ± 0.13 (Hasson et al., 2012).

A recent measurement for the rate constant and branching ratio for this reaction was performed using pulsed laser photolysis coupled with infrared wavelength modulation spectroscopy and UV absorption spectroscopy (Zuraski et al., 2020). The HO_2 and OH were simultaneously monitored by near-IR and mid-IR modulation spectroscopy, respectively, while $CH_3C(O)CH_2O_2$ was monitored by UV absorption. The overall rate constant for this reaction was found to be $(5.5 \pm 0.5) \times 10^{-12}$ $cm^3molecule^{-1}s^{-1}$ that is lower than the previous reported value $9.0 \pm 1.0 \times 10^{-12}$ $cm^3molecule^{-1}s^{-1}$ (Bridier et al., 1993) and the branching fraction of the OH yield was directly measured as 0.30 ± 0.04 that is higher than those found in the previous studies. The authors detail the reasons for this difference.

In summary, the literature data on the yield of the pathway (R 22b) leading to the formation of OH vary between 0.15 and 0.3, although too few studies exist. Concerning the rate constant, only two are currently available (Bridier et al., 1993; Zuraski et al., 2020).

In general, the literature has demonstrated that the reactions between simple RO_2 radicals (R= CH_3, C_2H_5) and HO_2 lead to the formation of relatively stable species, the associated hydroperoxides. However, more studies should be done on reactions between more complex RO_2 and HO_2, for a better understanding of chemistry in a clean atmosphere.

1.1.3.2. RO_2 + OH reactions

Recently, the reaction of RO_2 with OH radicals has been suggested as a possible fate for RO_2 radicals in clean environments but, to date, only few studies deal with these reactions.

In a modeling work, Archibald et al. (Archibald et al., 2009) have investigated the impact of the reaction between RO_2 and OH on the composition of trace gases in the marine boundary layer. In this study, they simulated the impact of such a reaction where the peroxy radicals were studied up to C_4. Three reaction pathways were simulated leading to the following products for the simplest RO_2 radicals, CH_3O_2:

$$CH_3O_2 + OH \rightarrow CH_2O_2 + H_2O \quad \text{(R 23a)}$$

$$CH_3O_2 + OH \rightarrow CH_3O + HO_2 \quad \text{(R 23b)}$$

$$CH_3O_2 + OH \rightarrow CH_3OH + O_2 \quad \text{(R 23c)}$$

Three scenarios were proposed by varying the value of the rate constant for all RO_2 + OH reactions between 0.5, 1.0 and 1.5 × 10^{-10} cm^3s^{-1}. For all scenarios they found a negligible effect on the O_3, NOx and OH concentrations in the marine boundary layer. However, a substantial increase in the mixing ratios of formic acid, HCOOH, was observed if the major pathway would be (R *23*(R 23a) and a strong increase in the mixing ratio of CH_3OH was observed if the major pathway would be (R 23c). In addition, the impact on the concentrations of RO_2 and HO_2 radicals was very minor for all scenarios.

Even though this study reveals a possible, non-negligible impact of the reactions between RO_2 and OH on the composition of remote atmospheres, the further study concerning this reaction was only carried out in 2014 where Bossolasco et al. (Bossolasco et al., 2014) measured for the first time the rate constant of a reaction between RO_2 and OH radical. The study of the reaction between CH_3O_2

and OH was performed in a photolysis cell coupled to cw-CRDS for the measurement of CH_3O_2 and LIF for the measurement of OH.

$$CH_3O_2 + OH \rightarrow \text{Products} \qquad \text{(R 23d)}$$

The CH_3O_2 was formed from the photolysis of CH_3I in the presence of O_2, and the OH radical was formed from the photolysis of H_2O_2. The rate constant turned out to be very fast, k (298 K) = 2.8 ± 1.4 × 10^{-10} $cm^3molecule^{-1}s^{-1}$. Fittschen et al. (Fittschen et al., 2014) have included this reaction into the Leeds Master Chemical Mechanism (MCM) (Whalley et al., 2010) using data from a field campaign at Cape Verde Island, representative for the tropical remote ocean, and it was found that this reaction represents about 30% of the overall sink for CH_3O_2.

Following the work of Bossolasco et al., another measurement for the rate constant of the CH_3O_2 + OH reaction was performed in a photolysis cell coupled with UV absorption spectroscopy (Yan et al., 2016). The CH_3O_2 radicals were generated from the photolysis of acetone in the presence of oxygen and the OH radicals were formed from the photolysis of N_2O in the presence of H_2O. By fitting the absorption-time profiles to a complex mechanism, a rate constant k (298 K) = 8.7 ± 1.7 × 10^{-11} $cm^3molecule^{-1}s^{-1}$ was obtained, more than a factor of 3 slower than Bossolasco et al.

In order to elucidate such a large difference, the rate constant was measured again by Assaf et al. (Assaf et al., 2016) using the same experimental set-up as Bossolasco et al.

The CH_3O_2 and OH radicals were generated simultaneously from the photolysis of XeF_2 in the presence of CH_4 and H_2O. A rate constant k (298 K) = 1.6 ± 0.4 × 10^{-10} $cm^3molecule^{-1}s^{-1}$ was obtained, a value that is almost lower by a factor of 2 than that measured by Bossolasco et al., but still nearly a factor of 2 higher compared to that measured by Yan et al. Studies have shown that the high value obtained by Bossolasco et al. was due to the reactivity between the OH radicals and the iodine atoms when using CH_3I as precursor for CH_3O_2 radicals. However, the difference between the results of Assaf et al. and Yan et al. (Assaf et al., 2016; Yan et al., 2016) was not explained. The rate constants obtained in these two studies depend directly on the absorption cross section of the CH_3O_2 radicals used for the determination of its absolute concentration. Yan et al. used a UV-absorption spectroscopy, in a wavelength range where the absorption cross sections of peroxy radicals are assumed to be well known, while Assaf et al. used cw-CRDS in the near IR-region, in a wavelength range that is much less explored. Recently (Fittschen, 2019), the value of

the absorption cross section of CH_3O_2 measured by Assaf et al. (Assaf et al., 2016) has been recalculated taking into account rapid reactions that may interfere with the measurement of the absorption cross section of CH_3O_2. As the rate constant of the CH_3O_2 + OH reaction depends directly on the absorption cross section, a new value was determined: k (298K) = 1.0 ± 0.4 × 10^{-10} $cm^3molecule^{-1}s^{-1}$ that was in agreement with that of Yan et al. The impact on CH_3O_2 sink is then proportionally reduced (around 10 %) but still not negligible.

The high rate constant of this reaction makes it important to determine the reaction products in order to know its impact on the composition of the atmosphere. A summary of the current knowledge on the reaction products for the reaction CH_3O_2 + OH is presented in Figure 3.

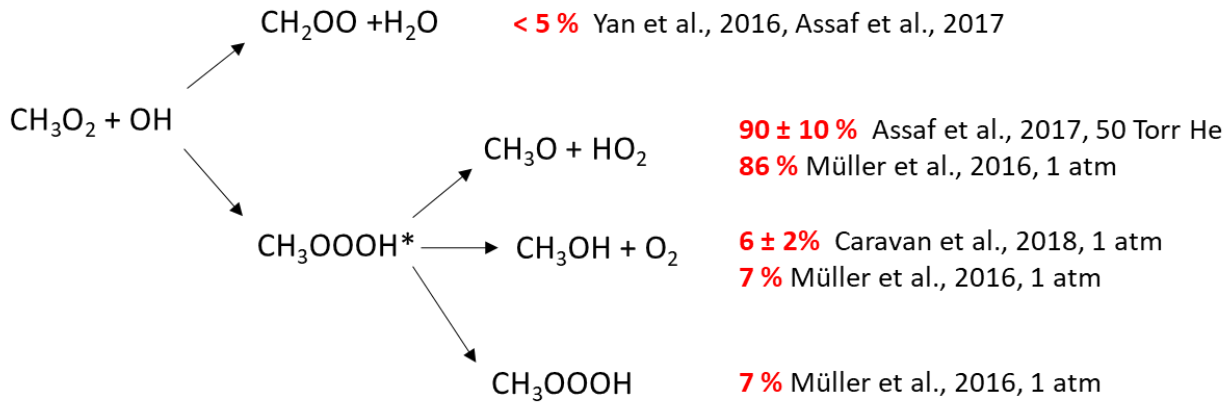

Figure 3: Summary of current knowledge on the reaction products for the reaction CH_3O_2 + OH

[From (Fittschen, 2019)]

Müller et al. (Müller et al., 2016) have investigated this reaction by means of theoretical calculations and showed that the dominant initial product is the singlet trioxide intermediate, CH_3OOOH.

$$CH_3O_2 + OH \rightarrow CH_3OOOH \qquad \text{(R 23e)}$$

This intermediate species can be stabilized or rapidly converted to a pre-product complex ($CH_3O\ldots OOH$) which breaks down into CH_3O and HO_2 (R 23b), with a small contribution to the formation of CH_3OH + O_2 (R 23c). The formation of a Criegee intermediate through pathway (R 23a) remains a minority, which had been found experimentally by Yan et al. (Yan et al., 2016) and Assaf et al. (Assaf et al., 2018b). Recent work has reported direct measurement of the methanol

yield (R 23c) using multiplexed photoionization mass spectrometry (MPIMS) and an atmospheric simulation chamber coupled to proton-transfer reaction time-of-flight mass spectrometry (PTR-TOF-MS) (Caravan et al., 2018). From simulation of the laser photolysis experiments, a yield of 9 ± 5% and 6 ± 2% was obtained from experiments in the low and high pressure reactor, respectively, for the channel (R 23c). The study also found evidence for a non-negligible yield of the stabilized trioxide, CH_3OOOH (R 23e) at high pressure, while no signal was detected during the low pressure measurements. These values are in good agreement with the calculations of Müller et al. (Müller et al., 2016), who predicted a yield of 7% at 760 Torr and 0.02% at 30 Torr. However, the measurements carried out in the atmospheric simulation chamber showed a yield for the channel (R 23c) of 17 ± 3% that are not in agreement with the laser photolysis experiment. It has been assumed that the trioxide, CH_3OOOH, is detected by PTR-TOF-MS at the mass of methanol CH_3OH. Thus, by considering that the yield of the pathway leading to the formation of CH_3OH measured in the simulation chamber corresponds to the sum of the yields of CH_3OH and CH_3OOOH, the theoretical calculations and the measurements in the photolysis cell and the chamber are in agreement.

The reactions of larger peroxy radicals ($C_2H_5O_2$, $C_3H_7O_2$, $C_4H_9O_2$) could also play a role in remote biogenic environments. The reaction of $C_2H_5O_2$ + OH has also been studied:

$$C_2H_5O_2+OH\rightarrow \text{Products} \qquad \text{(R 24)}$$

The rate constant of $C_2H_5O_2$+OH was measured by Farago et al. (Faragó et al., 2015) in the same set-up as (Bossolasco et al., 2014). The OH radicals were generated from the photolysis of H_2O_2 and the $C_2H_5O_2$ radicals were generated from the photolysis of $(COCl)_2$ in the presence of C_2H_6. After comparing the experimental data with a simulation model, the rate constant obtained was $k_{C2H5O2+OH}= (1.2 \pm 0.3).10^{-10}$ $cm^3molecule^{-1}s^{-1}$. This value was further confirmed by Assaf et al. (Assaf et al., 2017b), who also measured the rate constants for the two next-larger peroxy radicals, $C_3H_7O_2$ and $C_4H_9O_2$.

$$C_3H_7O_2+OH\rightarrow \text{Products} \qquad \text{(R 25)}$$

$$C_4H_9O_2+OH\rightarrow \text{Products} \qquad \text{(R 26)}$$

The peroxy radicals were created with the same method as for $C_2H_5O_2$, by the photolysis of $(COCl)_2$ in the presence of the corresponding alkane giving the rate constants $k_{C3H7O2+OH}= (1.4 \pm 0.3).10^{-10}$ $cm^3molecule^{-1}s^{-1}$ and $k_{C4H9O2+OH}= (1.5 \pm 0.3).10^{-10}$ $cm^3molecule^{-1}s^{-1}$.

Liu et al. (Liu et al., 2017) investigated theoretically for the first time the products of the reaction between $C_2H_5O_2$ and OH, showing that the dominant pathway leads to the formation of the trioxide C_2H_5OOOH, which directly decomposes to the products C_2H_5O and HO_2. The only experimental investigation of the product yields of larger peroxy radicals with OH was carried out by Assaf et al. (Assaf et al., 2018a), showing that the HO_2 yield strongly decreases when alkyl chain length increases: ϕ_{CH3O2} = (0.90 ± 0.1), ϕ_{C2H5O2} = (0.75 ± 0.15), ϕ_{C3H7O2} = (0.41 ± 0.08) and ϕ_{C4H9O2} = (0.15 ± 0.03). A theoretical model has been used to explain the clear decrease in HO_2 yield with the increase in the size of the alkyl group by increasing the stabilization of the corresponding trioxide. Thus, the trioxide seems to be the nearly exclusive product of the reaction between OH and RO_2 radicals containing more than three carbon atoms such as peroxy radicals obtained from the oxidation of the biogenic hydrocarbons.

The chemistry involving RO_2 and OH radicals is very complex and is a very recent research issue, the reactions of RO_2 + OH radicals have been for the first time included in an atmospheric chemistry model by Jenkin et al. (Jenkin et al., 2019). The CH_3O_2 + OH reaction mainly leads to the formation of CH_3O and HO_2 showing that the formation of methanol (R 23a) in a clean environment remains little influenced by this reaction (Caravan et al., 2018). The reactions involving OH with RO_2 radicals having more than two carbon atoms mainly leads to the formation of ROOOH trioxide, a species that can accumulate in a clean atmosphere (the atmospheric lifetime of ROOOH is estimated to be minutes to hours). A very recent study (Berndt et al., 2022) showed that from the isoprene-derived RO_2 radicals reacting with OH, there is an annual ROOOH production of up to ~ 10 million metric tons.

1.1.3.3. RO_2 + RO_2 reactions

Reactions between RO_2 radicals can take many forms called permutation reactions. These reactions include self-reactions (R 27) and cross-reactions (R 28) with other peroxy radicals $R'O_2$, for which different reaction pathways may occur (Jenkin et al., 2019; Orlando & Tyndall, 2012).

$$RO_2 + RO_2 \rightarrow RO + RO + O_2 \quad \text{(R 27a)}$$

$$RO_2 + RO_2 \rightarrow R_{-H}=O + ROH + O_2 \quad \text{(R 27b)}$$

$$RO_2 + RO_2 \rightarrow ROOR + O_2 \quad \text{(R 27c)}$$

$$RO_2 + R'O_2 \rightarrow RO + R'O + O_2 \quad \text{(R 28a)}$$

$$RO_2 + R'O_2 \rightarrow R_{-H}=O + R'OH + O_2 \quad \text{(R 28b)}$$

$$RO_2 + R'O_2 \rightarrow R'_{-H}=O + ROH + O_2 \quad \text{(R 28c)}$$

$$RO_2 + R'O_2 \rightarrow ROOR' + O_2 \quad \text{(R 28d)}$$

Many studies on RO_2 self-reactions exist (CH_3O_2, $C_2H_5O_2$, $C_3H_7O_2$, $C_4H_9O_2$, $CH_3C(O)O_2$, $C_2H_5C(O)O_2$, $HOCH_2O_2$…), but only the $C_2H_5O_2$ self-reaction, that was studied in this work, will be detailed in this part.

The $C_2H_5O_2$ self-reaction has several product pathways that either lead to stable products (R 29b and (R 29c, where (R 29c is thought to be minor) or maintain the radical pool through formation of HO_2 radicals ((R 29a) followed by (R 30) in the presence of O_2):

$$C_2H_5O_2 + C_2H_5O_2 \rightarrow C_2H_5O + C_2H_5O + O_2 \quad \text{(R 29a)}$$

$$C_2H_5O_2 + C_2H_5O_2 \rightarrow C_2H_5OH + CH_3CHO + O_2 \quad \text{(R 29b)}$$

$$C_2H_5O_2 + C_2H_5O_2 \rightarrow C_2H_5O_2C_2H_5 + O_2 \quad \text{(R 29c)}$$

$$C_2H_5O + O_2 \rightarrow CH_3CHO + HO_2 \quad \text{(R 30)}$$

$$C_2H_5O_2 + HO_2 \rightarrow C_2H_5OOH + O_2 \quad \text{(R 20a)}$$

Then, the investigation of the $C_2H_5O_2$ self-reaction (R 29a) is complicated by secondary reactions forming HO_2 through reaction (R 30) and HO_2 will react with $C_2H_5O_2$ (R 20a). The rate constant of (R 20a) is higher than that of (R 29a) and this accelerates the $C_2H_5O_2$ decays. As a result, measuring the rate constant k_{29} from the observed $C_2H_5O_2$ decays depends on the branching ratio $r' = k_{29a} / k_{29}$ used in the data treatment: for a given experimental $C_2H_5O_2$ decay the retrieved rate constant k_{29} will decrease with increasing branching ratio.

Earlier studies on the kinetics of $C_2H_5O_2$ self-reaction have either used time resolved UV absorption spectroscopy for the determination of the rate constant (Adachi & Basco, 1979; Anastasi et al., 1983; Atkinson & Hudgens, 1997; Bauer et al., 1992; Cattell et al., 1986; Fenter et al., 1993; Munk et al., 1986; Niki et al., 1982; Noell et al., 2010; Wallington et al., 1989, 1988) or, for the determination of the branching ratio, end product studies by FTIR (Niki et al., 1982; Wallington et al., 1989)or by gas chromatography (Anastasi et al., 1983).

The determination of the branching ratio by direct observations of the HO_2 yield is not possible in UV absorption studies since the steady-state HO_2 concentration, that builds-up from the (R 29a)/ (R 30) reaction sequence, is rather low due to the fast consumption of HO_2 through (R 20a). So, even if a relative selectivity between $C_2H_5O_2$ and HO_2 can be obtained by UV absorption, "clean" $C_2H_5O_2$ decays can be obtained when studying (R 29a), while the corresponding HO_2 profiles cannot be extracted. A correction of the HO_2 profile for contribution of $C_2H_5O_2$ would induce very large error bars since even at short wavelengths the much higher $C_2H_5O_2$ concentration compared to HO_2 concentration will always makes up the major fraction of the absorption signal. Therefore, time-resolved UV absorption studies used the branching ratio r', determined from end-product studies, to extract the rate constant k_{29} from the observed $C_2H_5O_2$ decays (k_{29obs} using $k_{29} = k_{29obs}/(1+r')$). This way, UV absorption measurements came to a fairly good agreement for the value of the overall rate constant and end-product studies also came to a relatively good agreement on the branching ratio. So, it was agreed in almost all studies that the radical channel (R 29a) is the major path with a branching fraction of $r' = 0.63$ and a total rate constant of $k_{29} = 7.6\times10^{-14}$ cm^3 $molecule^{-1}s^{-1}$ is currently recommended by the IUPAC committee (Atkinson et al., 2006a).

The most recent work of Noell et al. (Noell et al., 2010) used for the first time a more selective method to characterize the above reactions. The $C_2H_5O_2$ radicals were still detected by UV absorption but the HO_2 radicals were detected in a selective way using wavelength modulation spectroscopy in the near-infrared (NIR) region. The UV detection of $C_2H_5O_2$ allowed the determination of k_{29obs} that was similar to the previous studies. In addition, they measured the time resolved profile of secondary HO_2 formed through reaction (R 30) allowing the real time determination of r' and thus obtaining the rate constant k_{29} by a more reliable method than the previous studies. Interestingly, this work found a branching fraction of only $r' = 0.28$ for the radical path which is in large disagreement with the earlier recommendations where the radical path was

found to be the major path. Using this branching ratio leads to an overall rate constant of k_{29} = 1.19×10^{-13} cm^3s^{-1}, around 56% higher than the value recommended by IUPAC.

To our knowledge, no new measurements on the $C_2H_5O_2$ self-reaction have been carried out after this interesting finding of the important disagreement between the recommended IUPAC values and the results from Noell et al. It seems therefore important to reinvestigate this reaction with another selective detection method. This was performed in this work and will be presented in Chapter 4 of this manuscript.

The rate constants for the self-reaction of methyl peroxy radical, CH_3O_2, was also determined to be k = 3.5×10^{-13} $cm^3molecule^{-1}s^{-1}$ at 298 K that is currently recommended by the IUPAC committee (Atkinson et al., 2006a). The self-reaction of the simple peroxy radicals (CH_3O_2 and $C_2H_5O_2$) are slower than those between RO_2 and HO_2. However, for bigger and more complex peroxy radicals such as carbonyl peroxy radicals (of the $CH_3C(O)O_2$ type), the rate constants of the self-reactions are higher, of order of 10^{-11} / 10^{-12} $cm^3molecule^{-1}s^{-1}$. This shows that any substituent on the peroxy radicals tends to increase the rate constants dramatically (Bridier et al., 1993; Maricq & Szente, 1996). For example, the rate constant for the acetylperoxy ($CH_3C(O)O_2$) self-reaction was recently measured to be k = $(1.3 \pm 0.3) \times 10^{-11}$ $cm^3molecule^{-1}s^{-1}$ using laser photolysis coupled to two cw-CRDS (Assali & Fittschen, 2022). However, these reactions are still little known.

Cross reactions, reactions between different RO_2, mostly involving the CH_3O_2 radical and another radical, were also studied. The rate constant for the reaction CH_3O_2+ $C_2H_5O_2$ at 298 K is 2×10^{-13} $cm^3molecule^{-1}s^{-1}$ (Villenave & Lesclaux, 1996) and it is in the same order of magnitude of the rate constant of the reaction CH_3O_2 + CH_3O_2. The reactions of CH_3O_2 + carbonyl radical showed again that these reactions are faster than that with simple peroxy radicals. The rate constant for the reaction CH_3O_2 + $CH_3C(O)O_2$ is in the order of 10^{-11} $cm^3molecule^{-1}s^{-1}$ and that for the reaction CH_3O_2 + $CH_3C(O)CH_2O_2$ is in the order of 10^{-12} $cm^3molecule^{-1}s^{-1}$ (Bridier et al., 1993; Villenave & Lesclaux, 1996). Recently, the rate constant for the cross reaction CH_3O_2 + $CH_3C(O)O_2$ has been found as k = $(2.0 \pm 0.4) \times 10^{-11}$ $cm^3molecule^{-1}s^{-1}$ (Assali & Fittschen, 2022). The rate constants for a given RO_2 self-reaction is generally found to be similar to that of a cross reaction with CH_3O_2 (or $C_2H_5O_2$), suggesting that these particular peroxy radical cross reactions can play a significant role in the oxidation processes of the hydrocarbons in the troposphere.

Studying radical chemistry is difficult and requires many tools. Field campaign measurements allow the comparison of the experimental results with the simulation models. However, the experimental and modelled results are often in disagreement. Field campaigns in tropical forested environments showed an overestimation of the measurements over the models indicating that the chemistry of peroxy radicals in clean environment is not well understood (Whalley et al., 2011). In order to better understand this difference, laboratory kinetic measurements have to be carried out for precise determination of the reaction rate constants and products branching ratios.

1.2. Techniques for radical measurements

The detection of radicals is difficult because of their high reactivity with gases and surfaces. Highly sensitive techniques are needed to detect such species. Several techniques for the measurement of OH and HO_2 radicals were reviewed in details (Heard & Pilling, 2003). These techniques are based either on spectroscopic techniques with Laser Induced Fluorescence (LIF), Cavity-Ring Down Spectroscopy (CRDS), Differential Optical Absorption Spectroscopy (DOAS), or on chemical techniques with Chemical Ionization Mass Spectrometry (CIMS) and Peroxy Radical Chemical Amplification (PERCA). In the following section, some of the experimental techniques allowing the quantification of HO_x and RO_2 and the measurement of the rate constant for reactions involving these radicals will be presented.

1.2.1. Spectroscopic methods

This part will describe only the techniques used in this work, Laser Induced Fluorescence (LIF) and Cavity-Ring Down Spectroscopy (CRDS).

1.2.1.1. Laser Induced Fluorescence (LIF)

One of the most commonly used techniques is the Laser Induced Fluorescence (LIF), which allows the measurement of radical species such as the OH radical. This technique is based on the spontaneous emission of photons by the radicals undergoing radiative relaxation from their excited state towards their ground state after the absorption of a laser radiation. This technique has been used in this work and it will be described more in details in Chapter 2.

The LIF can also be used for indirect detection of HO_2 and RO_2 radicals by the FAGE (Fluorescence Assay by Gas Expansion) technique. With this technique the OH radicals are directly

measured by LIF while the HO_2 radicals are converted into OH radicals that can be detected by LIF. Thus, HO_2 is measured simultaneously in a second detection cell containing NO in excess that is added to the sampled gas leading to the conversion of HO_2 into OH. It is also possible to measure RO_2 radicals that can be converted to OH via the reaction with NO producing HO_2 which will further be converted to OH (Amedro et al., 2012; Chao et al., 2019). The limit of detection for OH radicals is around 10^5 cm^{-3} and for HO_2 radicals is around 10^6 cm^{-3} (Amedro et al., 2012), which makes the FAGE technique well-adapted for field measurements due to its high sensitivity.

1.2.1.2. Cavity Ring-Down Spectroscopy (CRDS)

Most of the previous studies of peroxy radicals have been carried out by UV absorption spectroscopy. For example, the absorption spectrum of CH_3O_2 radicals has been determined several times (Nielsen et al., 2002; Wallington et al., 1992) and an absorption cross-section of 4.6×10^{-18} cm^2 at 240 nm has been obtained. However, the selectivity in the UV region is poor because the absorption spectra of the RO_2 radicals are broad and the spectra of many different species are overlapping. The peroxy radicals can also be measured in the near-infrared (NIR) region. The development of resonant cavities with highly reflective mirrors improves the sensitivity of these techniques by increasing the optical path length. Among the techniques that are based on increasing the path length is the CRDS. This method has been applied in laboratory kinetics studies for the detection of organic peroxy radicals. It is based on the measurement of the photon lifetime in an optical cavity. Peroxy radicals were detected by CRDS technique (Pushkarsky et al., 2000) in the near-infrared region where they show a more structured and characteristic absorption features. For example, the absorption spectrum of CH_3O_2 has been measured (Farago et al., 2013) in the wavelength range 7470 – 7500 cm^{-1} and an absorption cross-section of 4.38×10^{-20} cm^2 at 7488.18 cm^{-1} has been obtained. Since then, several measurements for the absorption spectra and cross-sections for different species have been carried out in the near-infrared region. The CRDS technique allows direct measurement of the OH, HO_2, and CH_3O_2 radicals (Assaf et al., 2016). Using this technique makes it possible to reach a low limit of detection of around 10^{10} cm^{-3} for HO_2 for example (Thiebaud et al., 2007). This technique has been used in this work and it will be described more in details in Chapter 2.

1.2.2. Experimental Techniques for rate constant measurements

1.2.2.1. Atmospheric Simulation Chamber

The atmospheric simulation chamber is used to study reactions of atmospheric interest under controlled conditions that are close to real atmospheric conditions (temperature, pressure, irradiation). The atmospheric simulation chambers are numerous and different according to their shape, volume, as well as the material used, which is the main characteristic of the simulation chamber. The temperature and pressure ranges used are also different. The method of analysis of different species and in particular the radicals vary from one simulation chamber to another. Different techniques can be used to measure radical species in an atmospheric simulation chamber (Djehiche et al., 2011; Malkin et al., 2010; Winiberg et al., 2016).

In general, large simulation chambers are made up of Teflon and are naturally irradiated by the solar flux, for example HELIOS (Ren et al., 2017), SAPHIR (Rohrer et al., 2005), and EUPHORE (Zádor et al., 2006). The smallest chambers (with a volume of the order of m^3) are mostly made up of Teflon and few are made up of Quartz or Pyrex and use artificial light sources to mimic the solar irradiation (Doussin et al., 1997). Moreover, some simulation chambers are made up of steel or aluminum giving these chambers the facility for performing temperature and pressure variable experiments, for example HIRAC (Glowacki et al., 2007) and CHARME (Fayad, thesis 2019). In these cases, light for photochemical studies is provided by UV lamps located in or outside the simulation chambers. The wide variety of simulation chambers makes it possible to have a very complementary panel.

1.2.2.2. Relative rate technique

This method is based on measuring simultaneously two or more reactant species relative to each other. The ratio of the decay rate of the investigated reactant with an oxidant (OH radical or Cl atom as examples) and the decay rate with a reference species gives the rate constant of the reactant with the oxidant:

$$\text{OH or Cl} + \text{Reactant} \rightarrow \text{Product 1} \qquad \text{(R 31)}$$

$$\text{OH or Cl} + \text{Reference} \rightarrow \text{Product 2} \qquad \text{(R 32)}$$

The concentration of the oxidant (OH or Cl) is considered as constant between the reactions (R 31) and (R 32) and the rates can be written as:

$$\frac{-d[\text{Reactant}]}{dt} = k(\text{R } 31)[\text{Radical}][\text{Reactant}] \qquad \text{Equation 1}$$

$$\frac{-d[\text{Reference}]}{dt} = k(\text{R } 32)[\text{Radical}][\text{Reference}] \qquad \text{Equation 2}$$

Then, the integration of Equation 1 and Equation 2 lead to

$$\ln\left\{\frac{[\text{Reactant}]_{t=0}}{[\text{Reactant}]_t}\right\} = \frac{k(\text{R } 31)}{k(\text{R } 32)} \ln\left\{\frac{[\text{Reference}]_{t=0}}{[\text{Reference}]_t}\right\} \qquad \text{Equation 3}$$

The concentration of the reactant and the reference compound are measured as a function of time where the plot of $\ln\left\{\frac{[\text{Reactant}]_{t=0}}{[\text{Reactant}]_t}\right\}$ as a function of $\ln\left\{\frac{[\text{Reference}]_{t=0}}{[\text{Reference}]_t}\right\}$ give a straight line with a slope of $\frac{k(\text{R } 31)}{k(\text{R } 32)}$. Then it will be possible to determine the rate constant k(R 31) from the known rate constant of the reference reaction k(R 32). The disadvantage of this method is that unknown secondary reactions may occur, leading to systematic errors in the measurement of the rate constant. This technique is often used in simulation chambers for rate constant measurements (Chen et al., 2003; Thüner et al., 2004).

1.2.2.3. Flash photolysis technique

This technique is based on forming radicals in a cell from the precursors through a photolysis pulse, either by a pulsed laser or a pulsed flash lamp. The evolution of the radical concentration can subsequently be followed by time-resolved detection technique. The time scale of the investigated reaction is determined by the duration of the photolysis pulse which should be short compared to the reaction time. It can be in the order of a nanosecond in the case of a laser pulse or in the order of millisecond in the case of the UV lamps.

The flash photolysis technique has many advantages. The reactants are produced from well-mixed precursors, so there is no mixing time reducing the time resolution. The reaction time zero is easy to determine and corresponds to the photolysis pulse. Also, the reactants are generated at the center of the cell by the laser and thus the recombination reactions at the walls are generally minimized. However, a suitable precursor is not always easily available and the co-photolysis products can cause secondary reactions which are difficult to be taken into account. This technique is widely

used in the literature for the study of radical reactions (Assaf et al., 2016; Lightfoot et al., 1990; Noell et al., 2010). This technique has been used in this work and it will be described in Chapter 2.

1.2.2.4. Fast flow technique

The radicals are generated continuously by an electric or microwave discharge or by UV photolysis within a fast flow tube. The reactor consists of a fixed tube and a moveable injector where two radicals can be generated separately either in the fixed tube or in the injector. By varying the position of the moveable injector into the flow tube, it is possible to vary the reaction time between the two radicals. The radicals are highly diluted in a neutral gas, most often nitrogen or helium. The flow velocity along the tube is in the order of 10 $m.s^{-1}$. In this technique, the temperature range usually varies between 200 and 900 K (Morin et al., 2017) and the pressure can vary between 0.5 and 10 Torr (for laminar low pressure flow tube). This technique has been used in this work and it will be described more in details in Chapter 2.

The fast flow technique has many advantages. The reactants and the products can be detected by a wide variety of methods. This advantage arises from the steady-state nature of the flow system in which the progress of the reaction is frozen at any fixed observed point along the tube. As the concentration of the reactant is constant at that point, there is no limitation on the speed of the detector which is in contrast with the measurements in a photolysis cell that require a time-resolved detection technique (Howard, 1979). Another advantage for the discharge flow technique is the great versatility it provides for working with a wide variety of reactants. Also, working at low pressure provides better spectroscopic resolution and most of the rate constants for radical reactions are independent of pressure. The radicals can be generated separately that makes it possible to control the precursors and thus reduce the secondary chemistry. However, it is necessary to well define the time zero of the reaction (which corresponds to the moment when the reaction starts, i.e. at the end of the mixing time) between the species coming from the reactor and the injector in order not to distort the measurement. In addition, contributions from heterogeneous reactions on the walls can be significant and need to be taken into account, but this effect can be minimized by coating the inner surface with an unreactive substance or by varying the diameter of the reactor. This technique is widely used in the literature for the study of radical reactions (Bedjanian et al., 2001; Morin et al., 2017; Raventós-Duran et al., 2007b).

A comparison of the flash photolysis and the discharge flow techniques that have been used in this work is summarized in

Table 1.

Table 1: Comparison of flow tube and flash photolysis techniques

	Fast flow tube	Flash photolysis
Detection versatility	Wide variety	Requires fast detector
Reactant versatility	Wide variety	limited
Heterogeneous reactions	Can be significant	none
Reaction time zero	Need to be well defined	Correspond to the laser pulse

1.3. Conclusion

This chapter has described the structure of the atmosphere with emphasis on the radical chemistry in the troposphere. Experimental techniques for carrying out kinetic studies in the laboratory have also been described. In this work, two experimental set-ups have been used to study radical + radical reactions: a fast flow reactor that was continued to be developed in the frame of this work and which is designed to complement an existing photolysis cell set-up. The fast flow reactor is coupled to three complementary techniques: the cw-CRDS for the measurement of the HO_2 radical, the LIF for the detection of the OH radical and Mass spectrometry with Molecular Beam sampling (MB/MS) for the measurement of stable reaction products and radical species. The coupling of these three techniques to a flow reactor allows the study of the reactions of radical + radical type. On the other hand, the laser photolysis cell is coupled to a double cw-CRDS paths for the simultaneous measurements of RO_2 and HO_2 radicals and it was used for the kinetic and spectroscopic study of the ethyl peroxy radical. The complementarity of these two set-ups, the fast flow reactor and the photolysis cell, can be of great interest for a better understanding of radical + radical reactions in a clean atmosphere. These two set-ups will be described in details in the following chapter.

Chapter 2: Experimental Set-up

In this chapter, the two experimental set-ups used in this work will be detailed. First, the principle of the experimental techniques used will be described: Laser Induced Fluorescence (LIF), continuous wave-Cavity Ring Down Spectroscopy (cw-CRDS), and Mass Spectrometry analysis associated with Molecular Beam (MB/MS). Then, the fast flow reactor and the photolysis cell will be described. The fast flow reactor coupled to LIF, cw-CRDS, and MB/MS was developed during F. Kravtchenko's PhD (Kravtchenko, thesis 2019) and the photolysis cell coupled to two CRDS paths was developed during E. Assaf's PhD (Assaf, thesis 2017).

2.1. Principle of the techniques

2.1.1. Laser Induced Fluorescence (LIF)

Laser Induced Fluorescence (LIF) is one of the most sensitive and selective analytical technique used to measure the relative concentration of radicals and minor species. It is applied widely for the measurements of atmospheric trace gases, such as OH (Amedro et al., 2012).

Most atoms and small molecules absorb strongly in the ultraviolet region causing their excitation from the ground electronic state E_1 to excited electronic state E_n. After excitation, the molecule relaxes to a lower energy level. This can occur by emission of a photon, and can be divided into two categories: phosphorescence and fluorescence depending on the electronic configuration of the excited states.

Fluorescence is the spontaneous emission of a photon between states having the same spin $E_n \rightarrow E_1$ with the excited state having a very short lifetime of the order of a few hundred nanoseconds at low pressure. It is an allowed transition with the electron staying in the same multiplicity manifold. Intersystem crossing (ISC) is another process where phosphorescence is generated. Intersystem crossing is when the molecule undergoes relaxation from a singlet excited state to a lower energy triplet excited state. Then, relaxation from the triplet excited state to the singlet ground state causes emission of photons. This decay requires a change of multiplicity. Hence, it has a very low rate but it occurs due to spin-orbit coupling (So & Dong, 2001). The lifetime of the phosphorescence is typically between microseconds and a few seconds. Non-radiative deactivation processes including internal conversion (IC), vibrational relaxation or quenching can also occur.

Absorption and fluorescence spectra are unique and allow to characterize selectively a particular compound. Detection and analysis of the fluorescence signal enables to know the population density of the excited rovibronic energy level, which is proportional to the concentration of the species considered. However, fluorescence techniques are in general less efficient for large molecules because quenching, ISC and IC relaxations become increasingly competitive processes with spontaneous emission. A simplified Jablonski diagram, shown in Figure 4, summarizes these different excitation and relaxation processes of excitement and relaxation.

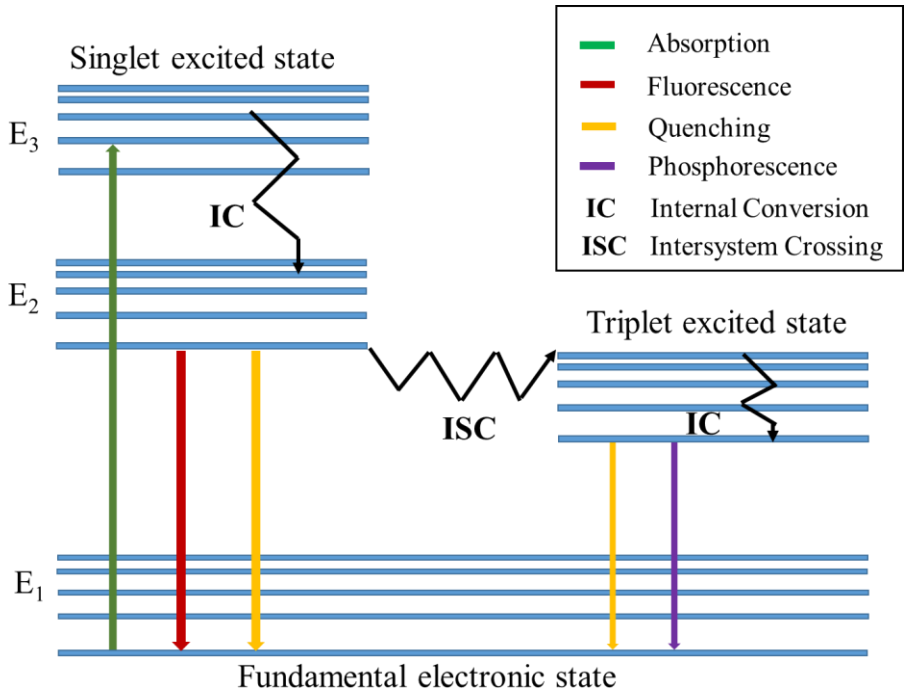

Figure 4: Jablonski energy diagram

If we take the case of a simple diagram with two energy levels E_1 and E_2, the variation of the population of the excited level E_2, during a laser pulse, is expressed according to the following law:

$$\frac{dN_2}{dt} = N_1 B_{12} U_v - N_2(B_{21} U_v + A_{21} + Q_{21}) \qquad \text{Equation 4}$$

with:

N_1 the population of the fundamental level E_1

N_2 the population of the excited level E_2

B_{12} the Einstein coefficient of absorption (in $m^3J^{-1}s^{-2}$)

U_υ the spectral energy density of the laser at the frequency υ (in $Jm^{-3}s$)

B_{21} the Einstein coefficient of stimulated emission (in $m^3J^{-1}s^{-2}$)

A_{21} the Einstein coefficient of spontaneous emission (Fluorescence) (in s^{-1})

Q_{21} the rate of collisional relaxation (Quenching) (in s^{-1})

If we assume that t_0 corresponds to the start of the laser pulse, then at t_0 only the fundamental level is populated ($N_{1(t=t0)} = N_1^0$; $N_{2(t=t0)} = 0$ and $N_1 + N_2$ = constant = N_1^0). Then the solution to Equation 4 is:

$$N_2 = N_1^0 . \frac{B_{12}U_\upsilon}{(B_{12}+B_{21}).U_\upsilon + A_{21} + Q_{21}} . [1 - \exp((B_{12} + B_{21})U_\upsilon + A_{21} + Q_{21})\ t] \qquad \text{Equation 5}$$

The first term corresponds to the maximum population density of level E_2 which can be reached. The second term describes the pumping kinetics τ_p, defined by the following equation:

$$\tau_p = \frac{1}{(B_{12}+B_{21}).U_\upsilon + A_{21} + Q_{21}} \qquad \text{Equation 6}$$

By replacing τ_p with its expression in Equation 5, we get:

$$N_2 = N_1^0 . B_{12}U_\upsilon . \tau_p . \left[1 - exp\left(\frac{t}{\tau_p}\right)\right] \qquad \text{Equation 7}$$

The fluorescence signal from the excitation is expressed as follows:

$$S_F \propto A_{21} . N_2 . h\upsilon_{21} \qquad \text{Equation 8}$$

According to Equation 7, by plotting the evolution of N_2 as a function of time, two excitation regimes are possible: the linear regime and the stationary regime. These regimes vary depending on the duration of the excitation laser pulse compared to the pumping time.

The linear time regime is observed when the duration of the laser pulse t is very short compared to the pumping time τ_p. This regime is generally obtained when working at low pressure and fairly low laser energy. In Equation 7, if we approximate the exponential by its limited development of order 1, then:

$$N_2 = N_1^0 . B_{12}U_\upsilon . \tau_p . \left[1 - \left(1 - \frac{t}{\tau_p}\right)\right] \qquad \text{Equation 9}$$

Then,

$$N_2 = N_1^0.B_{12}U_v.t \qquad \text{Equation 10}$$

The population of N_2 is then linear in time and directly proportional to the concentration and independent of quenching.

The steady state is reached when the pumping time τ_p is very short with respect to the time of the laser pulse t. From Equation 7, if $t >> \tau_p$ then:

$$N_2 = N_1^0.\ B_{12}U_v.\ \tau_p = \frac{N_1^0.B_{12}U_v}{(B_{12}+B_{21}).U_v+A_{21}+Q_{21}} \qquad \text{Equation 11}$$

So,

$$N_2 = N_1^0.\frac{B_{12}}{(B_{12}+B_{21})}.\frac{1}{1+\frac{U_v^S}{U_v}} \qquad \text{Equation 12}$$

With:

U_v^S the saturation energy density

$$U_v^S = \frac{A_{21}+Q_{21}}{B_{12}+B_{21}} \qquad \text{Equation 13}$$

In steady state, the evolution of the N_2 population as a function of the energy density of the laser pulse U_υ also breaks down into two regimes: the linear energy regime and the saturated regime.

The linear energy regime is characterized by a linear increase in the N_2 population as a function of laser energy. This regime is obtained when $U_\upsilon << U_v^S$. Thus, Equation 12 becomes:

$$N_2 = N_1^0.\frac{B_{12}}{(B_{12}+B_{21})}.\frac{U_v}{U_v^S} = N_1^0.\frac{B_{12}U_v}{A_{21}+Q_{21}} \qquad \text{Equation 14}$$

In this case, the population N_2 is dependent on Q_{21}, the quenching rate. The signal of fluorescence is thus proportional to:

$$S_F \propto N_1^0.\ B_{12}U_v.\frac{A_{21}}{A_{21}+Q_{21}}.h\upsilon_{21} \qquad \text{Equation 15}$$

The term $\frac{A_{21}}{A_{21} + Q_{21}}$ corresponds to the quantum fluorescence yield, that is the number of photons emitted per excited molecule and is directly dependent on the quenching rate Q.

The saturated energy regime is obtained when $U_\upsilon >> U_\upsilon^S$. In this case:

$$N_2 = N_1^0 . \frac{B_{12}}{(B_{12} + B_{21})} \quad \text{Equation 16}$$

The population of the excited state N_2 then becomes independent of the saturation energy U_υ^S and therefore Q_{21} quenching rate and the spectral energy density of the laser U_υ.

These different regimes are valid for the analysis of simple diatomic species at low pressure, like OH radicals. In our case, we work in regime stationary in time and linear in energy.

The fluorescence signal observed depends on the energy of the laser, but also on the following parameters: V (the measurement volume), **Ω** (the solid collection angle) and G (the gain related to the optical device). The expression of the photon flux is presented in the equation below:

$$S_F = G . N_2 . \frac{A_{21}\Omega}{4\pi} . V \quad \text{Equation 17}$$

Using the expression of population density N_2 (Equation 5) and placing in low excitation regime ($(B_{12} + B_{21}) U_\upsilon < (A_{21} + Q_{21})$), the value of the flux of fluorescence photons collected becomes:

$$S_F = \frac{G.\Omega.V}{4\pi} N_1^0 . B_{12} . U_\upsilon \frac{A_{21}}{A_{21} + Q_{21}} . \left[1 - \exp\left(\frac{t}{\tau_{eff}}\right)\right] \quad \text{Equation 18}$$

with τ_{eff} the fluorescence lifetime:

$$\tau_{eff} = \frac{1}{A_{21} + Q_{21}} \quad \text{Equation 19}$$

Thus, the collected fluorescence signal is directly proportional to the density of N_1^0 population of the E_1 ground state of the OH radical before the laser pulse. Most of the time, the LIF technique is used to measure the relative concentration of a species. This is because for an absolute measurement this technique requires the knowledge of the quenching parameters of all the

molecules present in the reaction medium, as well as all the parameters of the experimental device (values of G, V and Ω).

2.1.2. Continuous wave Cavity Ring Down Spectroscopy (cw-CRDS)

The Cavity Ring Down Spectroscopy technique is a highly sensitive absorption technique which allows the quantitative measurement of molecular or radical species. It is inspired by an experiment intended to precisely determine the reflection coefficient of highly reflecting mirrors by following the decay time of an optical cavity (Herbelin et al.,1980).

The first studies using this type of mirrors in an enhanced cavity configuration were developed to measure their reflectivity. In 1984, the exponential decrease in the intensity of light transmitted by a resonant cavity was observed for the first time (Anderson et al., 1984). A relation was established between the light decay of the cavity and the losses through the mirrors which allow to determine their reflectivity. The first study on cavity ring down spectroscopy was carried out in 1988 by verifying that the light decay is not only due to the losses through the mirrors but also to absorption of species inside the cavity (O'Keefe & Deacon, 1988). It was shown that this technique could be used to measure precisely and directly the absorption coefficient of a given species by using a pulsed laser.

In the majority of absorption spectroscopic techniques, the molecular absorption is deduced from the variation of light intensity passing through an absorbing medium. In the case of CRDS, the molecular absorption is deduced from the decay rate of the intensity of light stored between two highly reflecting mirrors. In 1996, the possibility of using continuous light sources, such as laser diodes, was studied (Lehmann, 1996).

There are two cases arising from the injection of a laser pulse into a CRDS cavity depending on two spectroscopic parameters: the spectral width of the laser line and the Free Spectral Range (FSR) between the modes of the cavity. The two cases are:

- A laser source with a broad spectral width that is greater than the FSR of the cavity (Figure 5A). In this case, at least one mode of the cavity will always be in resonance with the frequency of the laser. This is the case when pulsed laser sources are used.

- A laser source with a narrow spectral width that is less than the FSR of the cavity (Figure 5B). In this case, it is necessary to selectively excite a mode of the cavity to obtain a CRDS signal. The most suitable mode to excite is the TEM_{00} modes since it is the one with the lowest spatial shift limiting the losses by absorption, diffraction and diffusion. To excite the TEM_{00} modes, the length of the cavity is modulated by a piezoelectric transducer on which one of the two mirrors of the cavity is placed. This allows the mode of the cavity to get into resonance with the frequency of the laser. This is the case when continuous laser sources are used (cw-CRDS).

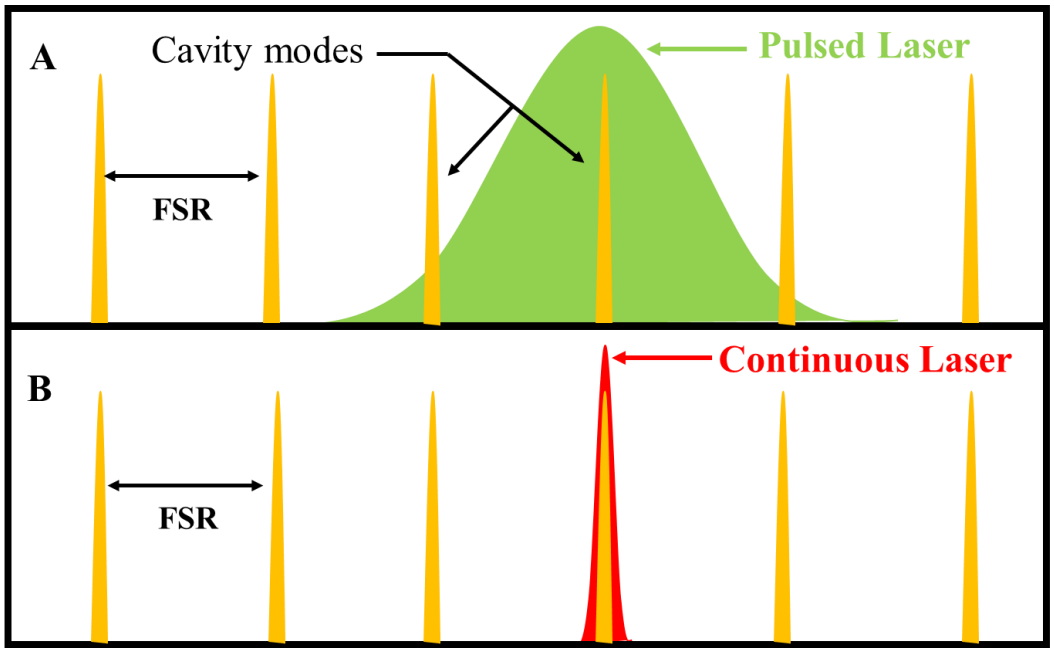

Figure 5: Schematic representation of the spectral width of the line of a pulsed laser (A) and a continuous laser (B) with respect to the modes of the cavity

In this work, the cw-CRDS technique was used, that is with a continuous source (laser diode). This technique was developed by Romanini et al. (Romanini et al., 1997). To measure the decay time, a laser pulse is trapped into an optical cavity composed of two mirrors with a radius of curvature Rc and a coefficient of reflectivity R, separated by a distance L. By taking into account the resulting losses at each round trip due to the mirror transmission and the intra-cavity absorption that is described by Beer-Lambert's law, the temporal evolution of the signal can be described by:

$$I(t) = I_0.\exp\left(-\frac{t}{\tau}\right) \qquad \text{Equation 20}$$

with:

I_0 the intensity transmitted at time t_0

I(t) the intensity transmitted over time

τ the ring down time (lifetime of photons in the cavity)

The principle of the CRDS technique is illustrated in Figure 6.

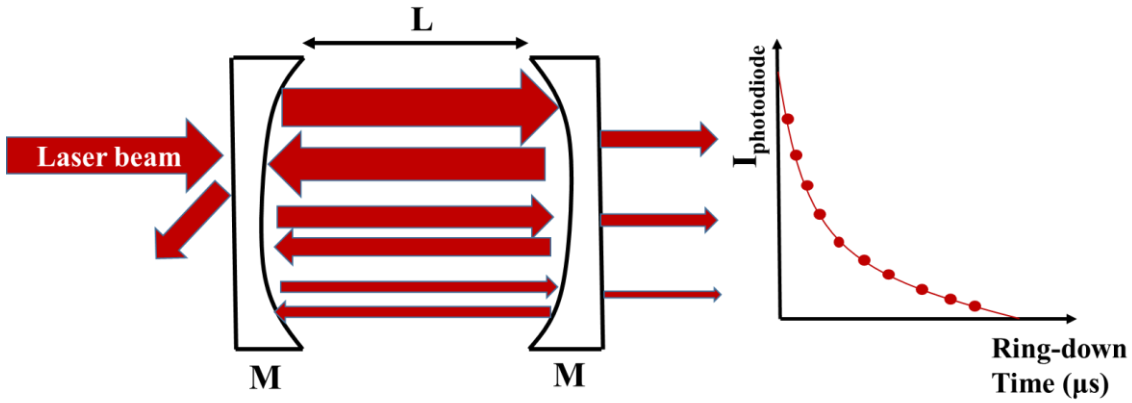

Figure 6: Scheme of the principle of the CRDS technique

The laser beam is injected through the front mirror and only a small fraction of photons enters inside the cavity due to the high reflectivity of the mirrors. The other part is reflected at the entrance of the cavity. Then the beam is reflected on both mirrors and, at each round trip, a part of the light is transmitted outside the cavity. The back and forth between the two mirrors continues until there are no more photons in the cavity. A detector is placed behind the rear mirror to measure the intensity of the transmitted light after each round trip.

When the cavity is empty, *i.e.*, in absence of absorbing species, the decay time τ_0 is measured directly by CRDS and is equal to:

$$\tau_0 = \frac{L}{c.(1-R)} \qquad \text{Equation 21}$$

with:

L the distance between the two mirrors (cm)

R the reflectivity coefficient of the mirrors

c the speed of light (cm s^{-1})

When absorbing species are present in the cavity, the decay time τ is shorter. This is because of photon losses due to absorption. Hence, in this case, the decay time τ is defined as:

$$\tau = \frac{L}{c.\ (1 - R + \sigma(\lambda).\ N.\ l)} \qquad \text{Equation 22}$$

with:

σ (λ) the absorption cross section of the species studied (cm^2)

N the concentration of the absorbent species (molecules cm^{-3})

l the length of the absorbent medium (cm)

Then, by using Equation 21 and Equation 22, the absorption coefficient α (λ) (cm^{-1}) can be defined as:

$$\alpha(\lambda) = \frac{R_l}{c}\left(\frac{1}{\tau} - \frac{1}{\tau_0}\right) = N \times \sigma(\lambda) \qquad \text{Equation 23}$$

with:

R_l the ratio between the length of the cavity L and the length of the absorbent medium l.

The absorption spectrum of the species can be obtained by measuring the absorption coefficient α (λ) as a function of the wavelength. By knowing the absorption cross section σ (λ) of a species at a given wavelength, its absolute concentration can be calculated by measuring τ_0 and τ.

2.1.3. Molecular Beam/Mass Spectrometry (MB/MS)

Mass spectrometry associated with a molecular beam sampling (MB/MS) is a technique that permits the detection of both, stable molecules and radicals, by measuring their mass. The operating principle of a mass spectrometer is based on the action of an electromagnetic field on a charged particle. Therefore, mass spectrometry analysis requires initially the formations of ions. In our case, the ionization is done by electron impact (in general at 70 eV).

Let M be a molecule and e^- the electrons created by electronic impact:

$$M + e^- \rightarrow M^+ + 2\ e^- \qquad \text{(R 33)}$$

The molecule M is ionized through interactions with the electrons whose energy exceeds the molecule's ionization energy and form a M^+ ion. This ion can then fragment depending on its internal energy. The signal in mass spectrometry corresponds to the ions and fragments detected. The ionization energy of a molecule is the minimum energy that the electron must have to ionize the molecule. For most molecules the probability to get ionized is relatively low if the energy of the electron is just slightly above the molecule's ionization energy (Hansen et al., 2009). The ionization probability increases with larger electron energies. In our experiments, the energy of the electrons is fixed at 70 eV but this energy can be adjusted depending on the molecule to be measured.

2.2. Fast flow reactor

2.2.1. Description

The fast flow reactor technique is known to be well adapted to the study of the kinetics of elementary reactions and radical + radical reactions. Indeed, this device makes it possible to set up two microwave discharges in order to generate the two radicals to be studied separately. Rate constants are generally measurable in the range 10^{-14} - 10^{-10} $cm^3molecule^{-1}s^{-1}$ in a temperature range usually varying from 200 to 900 K (Morin et al., 2017). This technique is used at low pressure (0.5-10 Torr). The determination of the kinetic parameters is usually done using the pseudo-first order approximation where one of the reactants is in excess relative to the other so that the concentration of the excess species can be considered constant during the reaction.

The reactor, shown schematically in Figure 7 and Figure 8, consists of a fixed cylindrical stainless steel tube of length 75 cm and internal diameter 2.5 cm. Inside the reactor there is an injector; it is a glass tube with length 77 cm and internal diameter 0.8 cm (1.2 cm external diameter). The radicals are generated either in the injector or in the fixed tube. Using the moveable injector allows the variation of the reaction time between the two reactants. A double injector configuration is also used depending on the method of generation of the radical species. In this case, an internal glass (or quartz) injector with length 95 cm and an internal diameter 0.5 cm (external diameter 0.7 cm) is introduced into the main glass injector (Figure 10). This double injector configuration is used when OH radicals are formed from the reaction of fluorine atoms and H_2O (see section 2.2.3.1).

The reactor and the external glass injector are coated internally with Halocarbon® wax (polymer of chlorotrifluoroethylene) in order to minimize the heterogeneous loss of radicals on the walls. Note that the reactive uptake coefficient of OH radicals by halocarbon wax is 5.14×10^{-4} (Slade & Knopf, 2013). The internal injector is not coated due to the small internal diameter 0.5 cm.

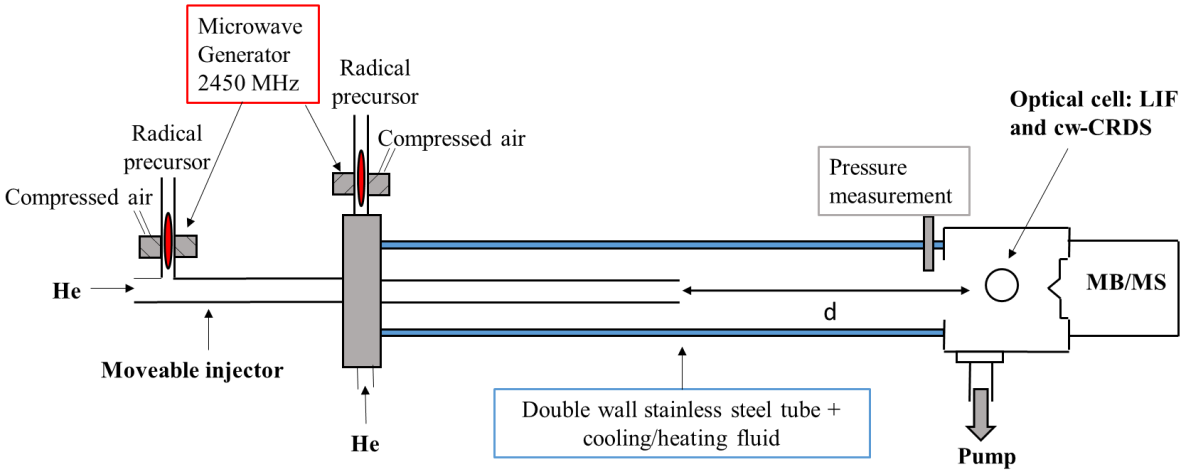

Figure 7: Schematic diagram of the flow reactor

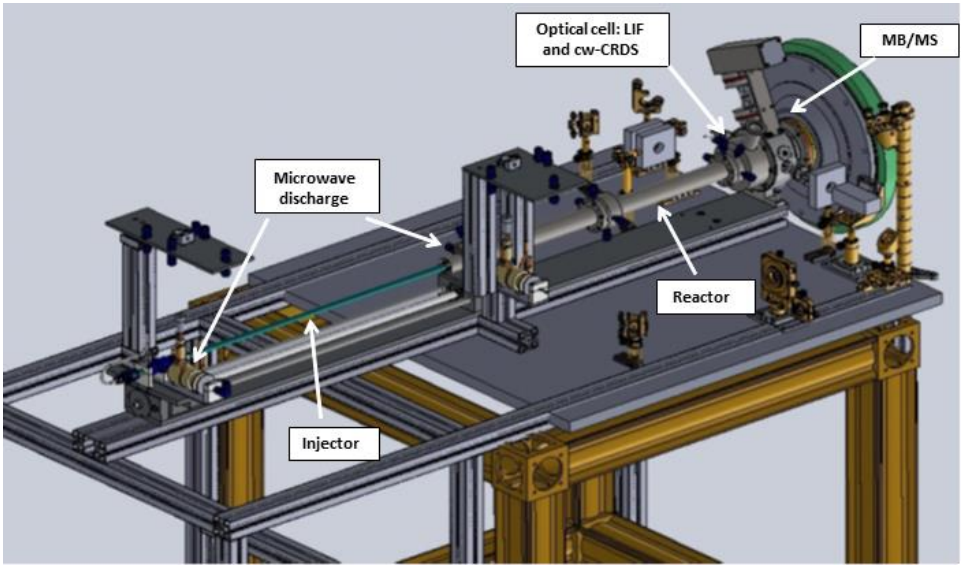

Figure 8: 3D representation of the reactor (Kravtchenko, thesis 2019)

Radicals are generated by microwave discharges (2450 MHz – 200W max, Sairem GMS200W). The pressure in the reactor is maintained between 0 and 10 Torr by using a 120 m^3 h^{-1} oil pump

(Pfeiffer UNO 120 A). Pumping occurs at the end of the reactor, after the optical cell and the flow passes through a part specially designed to prevent the return of the gas flow in the reactor. The gas flow is trapped using liquid nitrogen traps located between the reactor and the pump in order to protect the pump from corrosive species (such as F_2).

The pressure in the reactor is controlled by a Baratron© pressure gauge (capacitive pressure sensor MKS type 122 A). The reactants used are highly diluted in a neutral gas, helium in our case. The various gases introduced into the reactor and the injector are controlled by mass flow regulators (Tylan or Bronkhorst) previously calibrated.

To control the temperature in the reactor, it is enclosed in a double walled cylinder with a cooling or heating circulation system using a cryothermostat (Lauda Proline RP 855). The end of the reactor includes an optical cell with five optical accesses to allow measurements by laser techniques: Laser Induced Fluorescence (LIF) and cw-CRDS and a sampling cone for mass spectrometry.

2.2.2. Flow conditions

It is necessary to characterize the flow properties in the reactor in order to be placed in the condition of a plug flow.

2.2.2.1. Knudsen number and Reynolds number

A flow can be characterized by two dimensionless numbers: The Knudsen number and the Reynolds number. The Knudsen number determines whether the flow is viscous or molecular. In the case of viscous flow, Reynolds number makes it possible to determine whether it is laminar or turbulent.

Knudsen number is defined as:

$$Kn = \frac{L_m}{r} \qquad \text{Equation 24}$$

With:

L_m the mean free path of a molecule (in cm)

r the radius of the reactor; here r = 1.25 cm

Depending on the Kn value, the flow in the reactor can be of three different types:

If $Kn < 10^{-2}$, the flow is viscous.

If $Kn > 10^{2}$, the flow is molecular.

If $10^{-2} < Kn < 10^{2}$, the flow is said to be transitional.

The mean free path L_m is defined by:

$$L_m = \frac{< c >}{Z} \qquad \text{Equation 25}$$

With:

$< c >$ the average speed of movement due to thermal agitation (in m s^{-1})

Z the frequency of collisions (in s^{-1}).

The frequency of collisions is defined by:

$$Z = \frac{\sqrt{2}\,\pi\sigma_{He}^{\,2} < c > P}{k_B T} \qquad \text{Equation 26}$$

So,

$$L_m = \frac{k_B\, T}{\sqrt{2}\,\pi\sigma_{He}^{\,2}\, P} \qquad \text{Equation 27}$$

With:

k_B the Boltzmann constant in (J K^{-1}): $k_B = 1.38 \times 10^{-23}$ J.K^{-1}

T temperature (in K)

σ_{He} the effective collision diameter (in m): $\sigma_{He} = 2.57 \times 10^{-10}$ m

P pressure (in Pa)

In our experimental conditions, the pressure in the reactor is around 2 Torr (266.6 Pa) and the temperature is 293 K. Thus, $Kn \approx 2 \times 10^{-3}$ which is a value less than 10^{-2}. Hence, the flow in our reactor is viscous and the gas can be assimilated to a continuous medium where intermolecular interactions predominate.

Reynolds number is defined as:

$$Re = \frac{2\,\rho\, v\, r}{\mu} \qquad \text{Equation 28}$$

With:

ρ the density of the carrier gas (in g cm^{-3}), in our case the carrier gas is helium: $\rho_{He} = 2.18 \times 10^{-7}$ g.cm^{-3} at 298 K and 1 Torr.

v the flow velocity (in cm s^{-1})

r the radius of the reactor (in cm), here r = 1.25 cm

μ the dynamic viscosity of the carrier gas (in g $cm^{-1}s^{-1}$), for helium $\mu_{He} = 1.94 \times 10^{-4}$ g $cm^{-1}s^{-1}$ at 298 K.

If Re < 2000, the flow is laminar characterized by slow diffusion due to molecular agitation.

If Re > 2000, the flow is turbulent characterized by rapid diffusion leading to a disordered movement of the molecules.

Take as limit values low v = 1000 cm s^{-1} and high v = 3000 cm s^{-1}, these values correspond to the conditions that are used. In the case where v = 1000 cm s^{-1}, the Reynolds number Re = 2.81. When v = 3000 cm s^{-1}, Re = 8.43. These values are well below the threshold value of 2000, the flow in the reactor is therefore laminar.

2.2.2.2. Velocity distribution law

For a viscous and laminar flow, the radial velocity distribution is parabolic. In fact, the flow speed is not constant at all points. The flow speed at the walls is lower than that at the center of the reactor since the friction forces are higher at the walls. The speed is determined by the following expression:

$$v = 2\,v\left(1 - \frac{R_z{}^2}{r^2}\right) \qquad \text{Equation 29}$$

With:

R_z the distance between the point considered and the axis of the tube (in cm).

v the flow velocity (in cm s^{-1})

Thus, the speed is zero at the walls and maximum at the center of the reactor, as shown schematically in Figure 9.

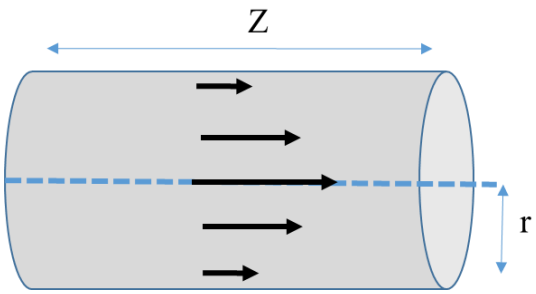

Figure 9: Radial velocity distribution in a reactor of viscous and laminar flow- with Z the length of the reaction zone and r the radius of the flow tube

The distance traveled at the inlet of the reactor is called the entry length and it is used to determine when the flow conditions are perfectly respected. It is defined by the Langhaar's formula (Langhaar, 1942):

$$l_e = 0.116.r.Re \qquad \text{Equation 30}$$

For example, in our experimental conditions, with r = 1.25 cm and Re between 2 and 8, the entry length is between 0.25 and 1.25 cm, corresponding to a homogenization time of less than 1 ms.

2.2.2.3. Approximation of the plug flow

The flow is said to be of plug type when the concentration of the species involved in any volume dV of the flow is uniform along the radius. It is possible to obtain a radial gradient of zero or very weak, if the species have a large radial distribution. This is due to the supply of reactants from the center to the wall. This hypothesis is verified if the following inequality is true:

$$\frac{k'r^2}{D_{coeff}} \leq 2 \qquad \text{Equation 31}$$

With:

k' the pseudo-first order rate constant (in s^{-1})

D_{coeff} the diffusion coefficient of the species measured in helium (in cm^2s^{-1}).

If we consider the OH radical, the diffusion coefficient of OH in helium $D_{coeff\,/\,OH}$ at 2 Torr is 380 cm^2s^{-1}. By taking a value of k'= 250 s^{-1}, the ratio is 1.027, which is less than 2. Thus the inequality

is validated and the flow can be considered as plug flow type. Hence, the gas between two straight sections of the reactor flows uniformly at a flow rate v.

Then, the reaction time t can be defined by the following relation:

$$t = \frac{d}{v} \qquad \text{Equation 32}$$

With:

d (in cm) the distance between the end of the injector and the measured point (*i.e.* the center of the optical cell).

2.2.2.4. Poiseuille's law

For a laminar flow at low pressure, the Poiseuille's law makes it possible to determine the pressure gradient in the absence of friction at the walls. This law is defined as:

$$\frac{\Delta P}{z} = \frac{8\, v\, \mu}{r^2} \qquad \text{Equation 33}$$

In our experimental conditions, we determine a maximum pressure drop (when v = 3000 cm s^{-1}) of the order of 2 millitorr cm^{-1}. This pressure gradient was therefore neglected for our measurements.

2.2.3. Generation of radicals

2.2.3.1. Generation of OH radicals

Two methods were used to generate the OH radicals in the flow reactor.

In the first method, OH radicals were formed from the reaction of fluorine atoms and H_2O. The fluorine atoms were produced in the microwave discharge from a mixture of 1% F_2 in helium:

$$F_2 \xrightarrow[\text{discharge}]{\text{microwave}} 2\ F \qquad \text{(R 34)}$$

The dissociation rate of F_2 was estimated by (Bedjanian et al., 2013) between 70 and 90%. In our case, we measured it by mass spectrometry following the signal at mass 38 which corresponds to F_2 with and without discharge, the dissociation rate obtained was 74% ± 12% (Kravtchenko, thesis 2019).

To reduce fluorine atoms reacting with the glass surface inside the microwave discharge, an alumina tube was used.

Thus by adding H_2O (in excess), the OH radicals are created rapidly:

$$F + H_2O \rightarrow OH + HF \qquad \text{(R 35)}$$

with $k = 1.4 \times 10^{-11}$ $cm^3 molecule^{-1} s^{-1}$ (Atkinson et al., 2006b) at T = 240 - 380 K.

The H_2O is introduced into the injector from a flask containing liquid H_2O placed in a temperature-regulated water bath maintained at 293 K. After the flask, there is a needle valve and a pressure gauge (Pfeiffer 0 - 2 bar) to control the pressure inside the flask. The saturated vapor pressure of H_2O at 293 K is 17.3 Torr. Thus, at this pressure, the H_2O vapor is in equilibrium with the liquid phase and H_2O in the gas phase can enter the injector. The H_2O concentration is controlled by the opening of the needle valve and it is determined by cw-CRDS at 6627.715 cm^{-1}. Using this method of OH generation, the configuration with the double injector is required, as shown in Figure 10.

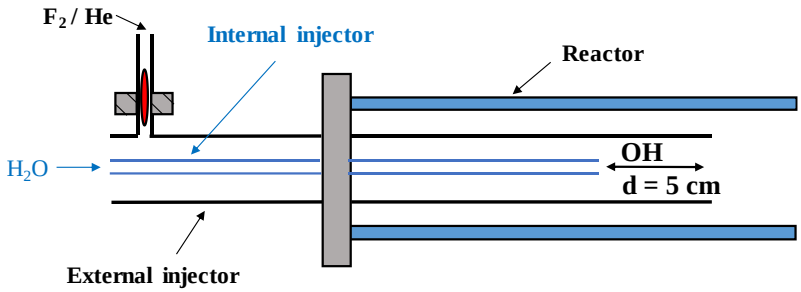

Figure 10: Schematic view of the double injector for OH radicals generation

F atoms are introduced into the external injector, while H_2O is introduced into the internal injector. This configuration makes it possible to minimize the losses of the radicals at the walls of the injector by generating the OH radicals at the end of the external injector where the time for OH formation is 2.3 ms (the distance between the ends of both injectors is 5 cm and v = 22 $m.s^{-1}$).

The concentration of F atoms was estimated from the reaction of $F + Cl_2 \rightarrow FCl + Cl$ ($k = 1.6 \times 10^{-10}$ $cm^3 molecule^{-1} s^{-1}$) (Appelman & Clyne, 1975). F atoms were introduced into the injector with $[F] = 5 \times 10^{12}$ molecules cm^{-3} and Cl_2 was introduced into the reactor with $[Cl_2] = 3 \times 10^{13}$ molecules cm^{-3}. Thanks to mass spectrometry, the signal for Cl_2 at mass 70 and the signal for FCl at mass 54

were monitored simultaneously. Measuring the conversion of Cl_2 into FCl showed that the concentration of F atoms consumed [F] = [FCl] (3.5×10^{12} molecules cm^{-3}) is close to the one expected (4.9×10^{12} molecules cm^{-3}).

The second method of OH generation involves the reaction of hydrogen atoms and NO_2. Similarly, the first step is to form the hydrogen atoms by microwave discharge from a mixture of 5% of H_2 in Ar:

$$H_2 \xrightarrow{\substack{microwave \\ dicharge}} 2\ H \qquad \text{(R 36)}$$

The dissociation rate of H_2 is lower than that of F_2, and is around 20% (Raventos-Duran et al., 2007a). We also estimated this dissociation rate (see Chapter 3 section 3.7.1.).

Thus by adding NO_2 (in excess) to the hydrogen atoms, the OH radicals are formed rapidly:

$$H + NO_2 \rightarrow OH + NO \qquad \text{(R 37)}$$

with $k = 1.47 \times 10^{-10}$ $cm^3 molecule^{-1} s^{-1}$ (Su et al., 2002) for T = 195-2000 K.

Using this method of OH generation, the configuration with the single injector was used, as shown in Figure 11.

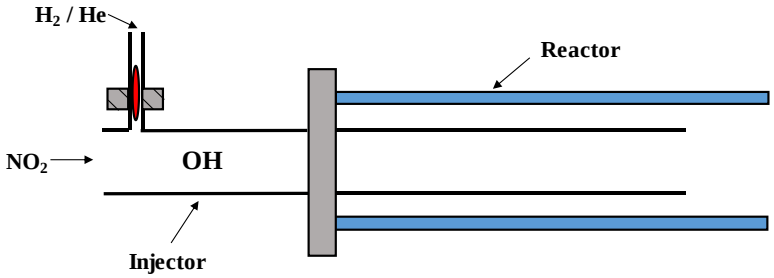

Figure 11: Schematic view of the single injector for OH radicals generation

Indeed, after testing the configuration of the double injector, the signal for OH was very weak (Kravtchenko, thesis 2019). Surprisingly, the H atoms seem more reactive to the outer walls of the internal injector than the F atoms. By using the single injector, the generation of the OH radicals was easier.

2.2.3.2. Generation of OD radicals

During our study, we also worked with the deuterated OD radical. The generation of this radical is very similar to that of the OH radical. The first step is the same, via the reaction (R 34). The second step is to replace H_2O with D_2O in the flask. And in the same way, D_2O (in excess) will react with F to form OD:

$$F + D_2O \rightarrow OD + DF \qquad (R\ 38)$$

with $k = 3.5 \pm 1.5 \times 10^{-12}$ $cm^3molecule^{-1}s^{-1}$ (Stevens et al., 1989).

This OD generation method is also performed with the configuration of the double injector.

2.2.4. Measuring the rate constant of a reaction

2.2.4.1. Determination of the pseudo-first order rate constant k'

The pseudo-first order approximation is used to determine the kinetic parameters. In this case, one of the two reactants is in excess relative to the other so that its concentration is considered to be constant during the reaction. For a bimolecular reaction of type A + B → products, the expression of the rate of disappearance of the reactants A and B is as follows:

$$-\frac{d[A]}{dt} = -\frac{d[B]}{dt} = k.[A].[B] \qquad \text{Equation 34}$$

with:

k the rate constant (in $cm^3molecule^{-1}s^{-1}$)

[A] and [B] the concentrations of species A and B respectively (in molecules cm^{-3})

If species B is in excess, with $[B]_0 > 10\ [A]_0$, then:

$$-\frac{d[A]}{dt} = k'.[A] \qquad \text{Equation 35}$$

with:

k' the pseudo-first order rate constant: $k' = k.[B]_0$.

The free radical can recombine at the reactor walls with a rate constant k_{wall}. So, the pseudo-first order rate constant k' is expressed by:

$$k' = k.[B]_0 + k_{wall} \qquad \text{Equation 36}$$

k_{wall} is obtained by measuring the concentration of the radical studied as a function of the reaction time in the absence of the excess reactant. The value of k_{wall} depends on the species as well as the nature of the material constituting the reactor, and on its surface condition. In our case, even though the reactor is coated with halocarbon wax to reduce the heterogeneous loss of the radicals, the recombination on the walls is not negligible. Since the k_{wall} can change from one day to another, k_{wall} determination is carried out at the same day when we want to determine the rate constant of a reaction.

After integrating Equation 35, we obtain the following equation:

$$\ln\frac{[A]}{[A]_0} = -k't + \text{constant} \qquad \text{Equation 37}$$

k' is obtained by measuring the logarithmic decrease of species A as a function of the reaction time for different concentrations of the excess species $[B]_0$, as shown in Figure 12. k' is the slope of the straight line obtained.

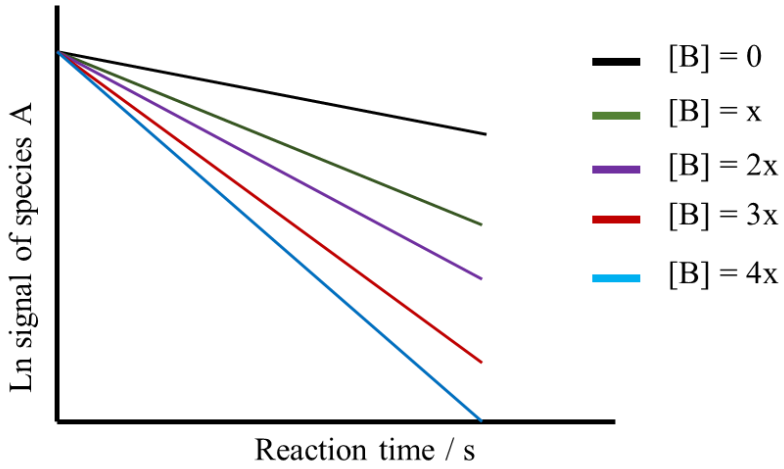

Figure 12: Logarithmic decrease of species A as a function of reaction time for different concentrations of excess species B

2.2.4.2. Determination of the real rate constant k

The real rate constant k is obtained by plotting k' as a function of the concentration [B] as shown in Figure 13. The value of k is the slope of the straight line obtained and the intercept corresponds

to the value of k_{wall}. To fully validate the kinetics, the k_{wall} value obtained experimentally (for [B] = 0) should be close to that obtained graphically by extrapolating the line in Figure 13 to zero.

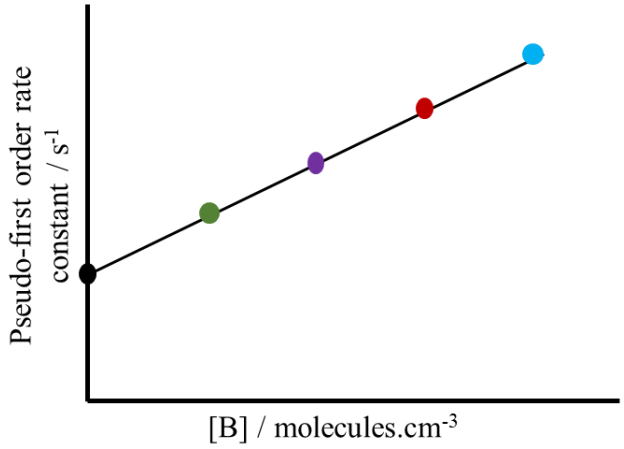

Figure 13: Determination of the rate constant

2.2.5. Purity of reactants

The source of the compounds used and their purity are given in Table 2.

Compound	Purity	Source
He	> 99.999%	Air Liquide
F_2	1% in He	Air Liquide
Cl_2	1% in He	Praxair
H_2	1% in He and 5% in Ar	Air Liquide
CH_4	>99.5%	Air Liquide
C_2H_6	>99.95%	Air Liquide
C_3H_8	>99.5% and 5% in N_2	Air Liquide / Messer
CH_3OH	>99.9%	Sigma-Aldrich
NO_2	1% in He	Messer
NO	2% in Ar	Messer
O_2	>99.9%	Air Liquide

Table 2: Purity and source of compounds used in experiments.

2.2.6. Experimental Implementation of LIF

As described in part 1.2.1.1. in Chapter 1, the LIF technique consists in collecting the photons emitted spontaneously by the species undergoing radiative relaxation from their excited state E_2 towards the fundamental state E_1. During this work, the LIF technique is used to detect the OH radicals. This radical is excited from the ground vibrational level (v " = 0) of the electronic ground state E_1 (state $X^2\Pi$) to the first vibrational level (v '= 1) of excited electronic state E_2 (state $A^2\Sigma$) at 282 nm (line $Q_1(1)$), using a tunable dye laser (Quantel TDL 50) pumped at 532 nm by a pulsed Nd-YAG laser (Quantel YG981, frequency: 10 Hz).

The emission of the dye laser is generated by a solution of rhodamine 590 in pure ethanol that fluoresces at 564 nm. The frequency of the fluorescence emission of the dye is then doubled by a doubling crystal in order to obtain a wavelength of 282 nm. A pinhole is placed at the laser outlet in order to take only the central part of the laser beam, with a diameter of about 0.6 cm and an energy of about 1 mJ. A small part of the beam is reflected on a photodiode by a microscope slide placed on the optical path of the laser beam. This allows to monitor the fluctuations of the laser energy. Then the laser beam is sent into the optical cell using a periscope because the optical axis of the LIF is not parallel to the optical table and arrives at an angle of about 30°, as shown in Figure 14. The red shifted fluorescence is collected perpendicular to the laser axis near 308 nm using two lenses and an interference filter (308 ± 5 nm) and detected by a photomultiplier (Hamamatsu R928).

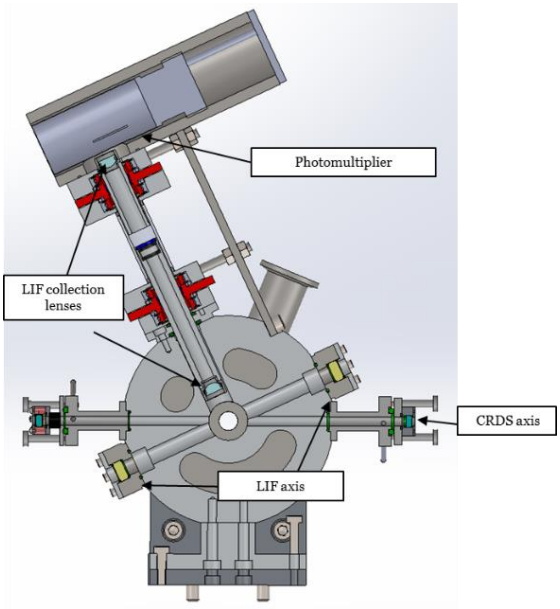

Figure 14: Schematic view of the LIF experimental set-up (Kravtchenko, thesis 2019)

The value of the OH LIF signal corresponds to the integral of the decay of the fluorescence signal (blue part in Figure 15) at the peak of the $Q_1(1)$ at 282 nm. The collected signal is processed using an oscilloscope and it is integrated using a Labview program where the integration time is of the order of 1.5 µs. The measurements are generally carried out by averaging the signals over 100 laser pulses (to obtain a better signal-to-noise ratio).

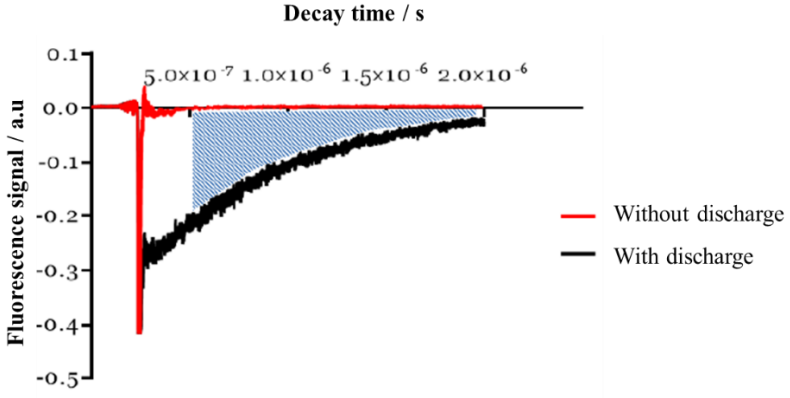

Figure 15: Integration of the fluorescence signal, average over 100 pulses of the excitation laser

Another radical species was also studied by LIF: the radical OD. The excitation of the radical OD is done on the same vibrational band as for OH, but at a different wavelength that is close to 287

nm. For this species, the emission of the dye laser is generated by a mixture of rhodamine 590 and rhodamine 610 diluted in pure ethanol and is used to move the dye emission peak towards the longer wavelengths. The rest of the device is the same, the collection always taking place at 308 ± 5 nm.

2.2.7. Experimental Implementation of cw-CRDS

During this work, the cw-CRDS technique was mainly used to measure the concentration of HO_2 radicals for which the absorption cross-section is very high ($\approx 10^{-19}$ cm^2) in the near infrared region (around 1506.4 nm or 6638.2 cm^{-1}).

The laser source used is a continuous infrared laser diode (Fitel FOL15DCWB-A81-W1509) placed in a frame (ILX Lightwave LDM-4980 Series). This laser diode is centered at 6629 ± 17cm^{-1} with a maximum output of 20 mW and controlled by two controllers: a temperature controller (ILX Lightwave LDT-5412), and a current controller (ILX Lightwave LDX-3525B). In order to control the wavelength, 1% of the laser source energy is directed to a wavemeter (Burleigh WA-1100) and 99% is sent to the CRDS cavity. An optical fibered acousto-optical modulator (AOM) (Gooch & Housego T-M110-0.2C2J-3-F2P) is connected to the laser diode. The modulator is a switch that differentiates the diffraction order of the laser. It is used to cut off very rapidly the light source to observe the decay time. The order 0 cannot extinguished completely because it is not diffracted by the AOM. Thus, the order 1 is used because this order can be extinguished completely and rapidly.

The laser beam, which is divergent from the exit of the fiber, passes through a focus lens (f = 10 mm), then into two return mirrors until it reaches the entrance mirror of the optical cavity (Figure 16). For the resonance to occur, the laser emission should coincide with one mode of the cavity (mono-mode excitation TEM_{00}); this is done by periodic modulation of the cavity length using a piezo-electric transducer (full displacement: 5 μm) on which the entrance mirror of the cavity is glued. When resonance occurs, the light builds up inside the cavity causing an increase in the light intensity transmitted at the exit of the cavity. When the intensity reaches a preset threshold value, the AOM stops injecting the laser beam into the cavity allowing the exponential decrease of the transmitted intensity.

A lens (f = 40 mm) is used to focus the beam on an avalanche photodiode converting the signal into current. A homemade amplifier threshold detector converts the current signal into voltage. It triggers the AOM when the cavity comes into resonance and the photodiode signal passes a user-defined threshold. The length of the cavity corresponding to the distance between the two mirrors is 23.3 cm. A helium flow (~ 200 sccm) is injected at the surfaces of the mirrors in order to protect them from deposit. This reduces the absorption path length compared to the cavity length and was determined to be equal to the flow reactor diameter, i.e. 2.5 cm (Kravtchenko, thesis 2019).

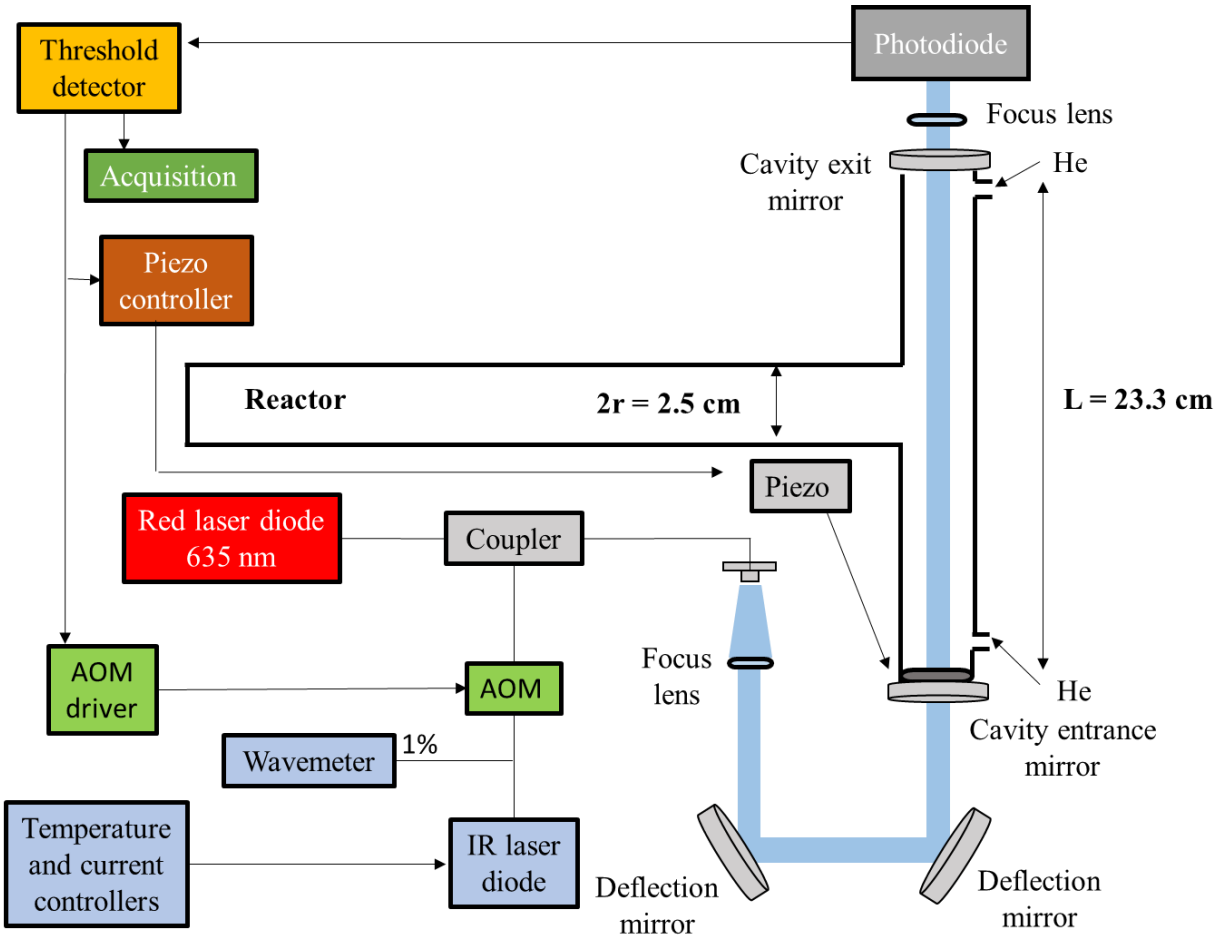

Figure 16: Schematic view of the cw-CRDS experimental setup

Aligning the CRDS cavity, which is the alignment of the IR beam in the center of the mirrors, is the most delicate step in setting up the technique. Wedged mirrors are used in order to avoid interferences from the back surface of the mirrors which can disturb the CRDS signals by creating

intermediate resonant cavities. However, the inclination of the outer faces of the mirrors by 0.5° will cause a deflection of the incident beam when traveling through the mirror. This will add steps to the alignment procedure compared to a procedure with plane mirrors that is more common on CRDS devices. Alignment is done using a fibered visible laser diode (635 nm) coupled to the IR beam. The diode at 635 nm is used to allow the complete alignment of the cavity since the IR beam is very attenuated at the exit of the mirror due to the high reflection of the CRDS mirrors, making that the IR beam is no longer visible after the mirror. Hence, the diode at 635 nm is necessary to obtain a correct alignment. At the end of this alignment, the IR laser can be put in place to detect the signal on the photodiode. In order to perform the alignment correctly, the beam of the IR laser and that of the visible diode must be perfectly collinear at the exit of the fiber.

2.2.8. Experimental Implementation of MB/MS

The gas is sampled through a 45° quartz cone (orifice diameter 600 μm) that is located 5 cm from the LIF/cw-CRDS optical axis. The molecular beam is generated by a differential pumping between three stages using turbomolecular and diaphragm pumps (with pressure of $10^{-5}/10^{-6}/10^{-7}$ Torr in each stage). These different stages are located after the optical cell allowing the pressure to be lowered quickly by differential pumping. The beam thus formed is directed towards the mass spectrometer to analyze the different species. The formation of the molecular beam permits a central sampling of the gas flow that represents the reaction medium. Isentropic expansion is generated, it causes a sharp decrease in the gas temperature and an increase in its speed. All these factors make it possible to “freeze” the progress of the reaction, so that the gas flow carried to the mass spectrometer is representative of the reaction medium analyzed. Figure 17 shows the different parts of the pumping stages.

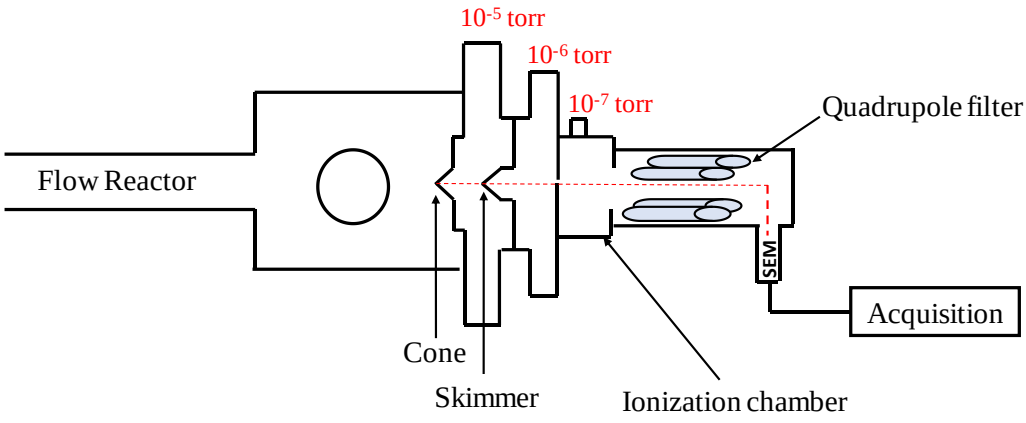

Figure 17:Schematic view of the MB/MS experimental setup

The molecular beam is formed in the first pumping stage thanks to the quartz sampling cone pierced in its center (600 µm). In our experimental conditions, the pressure in the first stage is around 10^{-5} Torr with a pressure of 2 Torr inside the reactor. Pumping is performed by two turbomolecular pumps (Pfeiffer TMU 260 – flow 210 L s^{-1}) whose primary vacuum is ensured by diaphragm pumps (Vacuubrand MD 4T – flow 3.3 m^3h^{-1}). These two turbomolecular pumps in the 1st stage are used to make it possible to obtain a vacuum that is strong enough to improve the quality of the molecular beam. Each of the two pumping groups is controlled by an electronic controller (Pfeiffer TCP 380). The pressure is measured by a Pirani gauge and a cold cathode Penning gauge (Pfeiffer PKR 250). A stainless steel skimmer, placed at 9.25 cm from the sampling cone, marks the end of the first stage.

The skimmer (diameter of 800 µm) is placed between the first and the second stage to sample the center of the beam. At the second stage the pressure is lower than that of the first stage; it is around 10^{-6} Torr. Pumping is performed by a single turbomolecular pump (Pfeiffer TMU 260) and a primary pump (Vacuubrand MD 4T) controlled by an electronic controller (Pfeiffer TCP 380). The pressure is measured with a cold cathode Penning gauge (Pfeiffer IKR 250).

Between the 2nd and the 3rd stages, the molecular beam is collimated through a 10 mm orifice. The pressure in the 3rd stage is around 10^{-7} Torr, and the pumping is carried out with the same equipment as for the 2nd stage. The alignment of the three orifices of the different stages must be precise to

allow the molecular beam to move freely up to the ionization chamber of the mass spectrometer. This alignment was done using a He / Ne laser.

In order to analyze the species present in the molecular beam, three steps are necessary: generate ions, separate the ions according to their mass / electronic charge ratio (m / z), then detect and quantify the ions generated.

Ions are generated in the ionization chamber by electronic impact (0 - 150 eV) using an electrically heated iridium filament. After the ionization chamber, the ionized species present in the molecular beam are analyzed by a quadrupole mass spectrometer (Hiden HAL / 3F RC). The quadrupole mass filter is composed of four parallel cylindrical molybdenum electrode bars that permit the separation of species according to their mass. Detection is ensured by a secondary electron multiplier with a sensitivity of the order of 10^{-15} mbar.

Mass spectrometry signals are obtained using the MASsoft 7 software. This allows different acquisition modes. The MID (Multiple Ion Detection) mode was preferentially used allowing to monitor a given mass as a function of time. This mode allows better sensitivity for weak signals. Indeed, by using the scanning mode to scan all the masses in a determined m/z range, the optimization is done for the highest signal. As a result, the sensitivity on weak masses is reduced. To determine the reaction products, the scanning mode will be used to identify all the species present and the MID mode will be used to study more closely one or more detected species.

2.3. Flash photolysis cell

The laser photolysis reactor is coupled to two continuous wave-Cavity Ring Down Spectroscopy absorption paths (cw-CRDS) (Assaf et al., 2017a; Parker et al., 2011; Thiébaud & Fittschen, 2006; Votava et al., 2012). The setup consists of a 0.79 m long flow reactor made of stainless steel along which the photolysis beam propagates and where the cw-CRDS techniques are installed. A schematic view of the experimental set-up is represented in Figure 18.

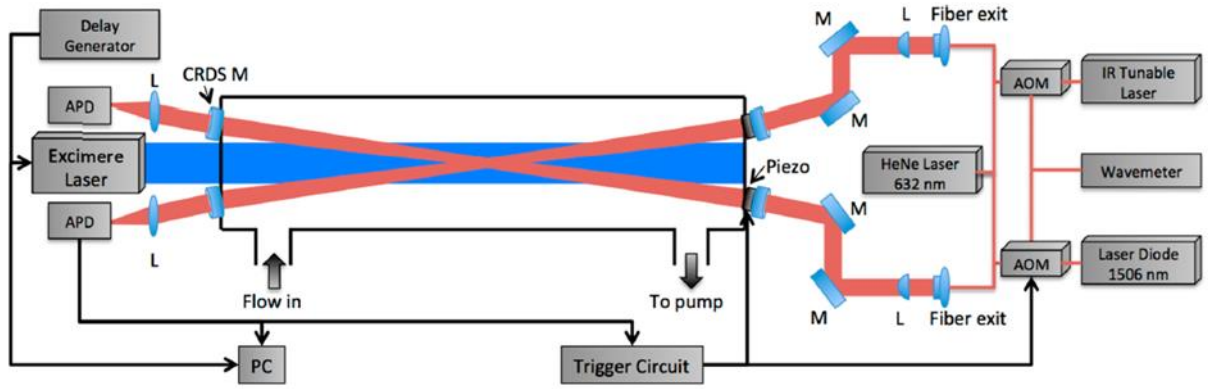

Figure 18:Schematic view of the experimental set-up. APD: Avalanche photo diode, AOM: Acousto-optic modulator, M: mirror, L: lens

A delay generator (Princeton Research 9650) is used to synchronize the experiment. It triggers the data acquisition of both cw-CRDS systems (National Instruments PCI-6259) and, after a delay of typically 1s, the photolysis laser (Excimer Lambda Physik LPX 202i, XeF at 351 nm) is triggered. The excimer beam width is delimited to 2 cm and passes through the reactor longitudinally. The two identical cw-CRDS absorption paths are installed in a small angle with respect to the photolysis path where an overlap with the photolysis beam of 0.288 m is achieved. Both beam paths were tested for a uniform overlap with the photolysis beam before performing the experiments. For this purpose, both cw-CRDS systems were operated to simultaneously measure HO_2 concentrations. The HO_2 concentrations were equivalent to better than 5%, showing that the photolysis laser was well aligned, i.e., both light paths probed a very similar photolysed volume in the reactor (Assaf, thesis 2017). A helium flow is injected at the surfaces of the mirrors in order to prevent them from being contaminated. Two distributed feed-back (DFB) laser diodes providing near-IR laser beams in different wavelength ranges are used for the detection of two species ($C_2H_5O_2$ at 7596.4 cm^{-1} (1316.4 nm) and HO_2 at 6638.2 cm^{-1} (1506.4 nm)). The laser beams are then injected into an acousto-optical modulator (AOM). The order 1 from the AOM is injected into the CRDS cavity, thus allowing to switch off rapidly and completely the beam entering the CRDS cavity while the order 0 is injected into a wavemeter (Burleigh) having an accuracy of 0.01 cm^{-1}. At the exit of the fiber, the beams pass one focal lens (L) and two mirrors M and are deflected into the cavities. Each cavity is formed by two highly reflective concave mirrors with a reflectivity R > 99.995% (Layertec) with the outer surfaces slightly wedged (tilt angle 0.5°). In order to align the cavity, a

HeNe laser should be used since the surfaces of the mirrors are wedged. A HeNe laser is coupled into the fiber at the exit of the AOM and the transmissibility of the mirrors at around 600 nm is high enough to visualize the beam at the exit of the cavity, allowing its alignment. The periodic modulation of the cavity length is done using a piezo-electric transducer on which the entrance mirror of the cavity is placed on. When the cavity length is in resonance with the laser emission wavelength, the light builds up inside the cavity causing an increase in the light intensity transmitted at the exit of the cavity. This transmitted intensity is focused by a lens (5 cm) on an avalanche photodiode (Perking Elmer C30662E) converting the signal into current. As soon as the photodiode signal exceeds a user-defined threshold, the AOM stops injecting the laser beam into the cavity allowing the exponential decrease of the transmitted intensity. A home-made tracking system is used to increase the occurrence of ring-down events and thus the sensitivity of the measurements (Votava et al., 2012). Then, the ring-down times τ retrieved from the exponential fit of the decay of light intensity are converted to absorbance α from the equation shown before:

$$\alpha = \frac{R_L}{c}\left(\frac{1}{\tau} - \frac{1}{\tau_0}\right) = N \times \sigma \qquad \text{Equation 23}$$

where τ_0 and τ are the ring-down time before and after the photolysis pulse, respectively; σ is the absorption cross section of the absorbing species; R_L is the ratio between cavity length (79 cm) and absorption length (28.8 cm); c is the speed of light.

2.4. Conclusion

This chapter has described the two complementary experimental set-ups used in this work with the coupling of the detection techniques. The fast flow reactor is coupled to the cw-CRDS for the measurement of the HO_2 radical, the LIF for the detection of the OH radical and MB/MS for the measurement of stable reaction products and radical species. The laser photolysis cell is coupled to a double cw-CRDS absorption paths for the measurement of RO_2 and HO_2 radicals. The experiments done using the fast flow reactor will be described in the following chapter.

Chapter 3: Tests to Understand the OH Re-formation Phenomenon

In this chapter, a summary of the previous work done to validate the recently developed experimental set-up consisting of a fast flow reactor coupled to LIF, cw-CRDS, and MB/MS will be presented. Then, the different tests carried out to explain the OH re-formation phenomenon observed in the previous work will be detailed.

3.1. Previous work

The experimental set-up was validated by the measurement of the rate constants of well-known reactions between OH radicals and stable species during the PhD of Florent Kravtchenko (Kravtchenko, thesis 2019). The OH radicals were generated in the double injector via the reaction of H_2O with F atoms that were produced using a microwave discharge of fluorine (1% F_2/He), as described in the experimental part. Reactions were studied under pseudo-first order conditions where the stable molecule (introduced in the reactor) was present in large excess over the OH radicals and thus the OH radicals were expected to decay in an exponential way. The rate constants were measured at 293 K and 2 Torr, with a total flow velocity of 22 m s^{-1}.

3.1.1. Study of reactions between OH and stable species

Several reactions were studied between OH radicals and different stable species (alkanes, alcohol). The OH fluorescence signal was monitored as a function of reaction time for different concentrations of alkanes (propane and ethane) and an alcohol (methanol). The reaction of the OH radical with these three stable species showed a non-exponential behavior of the OH decays. This non-linearity problem appeared when the OH consumption reached 80% in the case of alkanes and 50% in the case of methanol, as shown in Figure 19 and Figure 20, respectively. However, the rate constants obtained using only the linear part of the decay (filled symbols in Figure 19 and Figure 20) for propane $k_{C3H8+OH} = (1.1 \pm 0.28) \times 10^{-12}$ $cm^3 molecule^{-1} s^{-1}$ and for methanol $k_{CH3OH+OH} = (9.07 \pm 2.28) \times 10^{-13}$ $cm^3 molecule^{-1} s^{-1}$ were in good agreement with data from the literature (Baulch et al., 1985; Meier et al., 1984). The rate constant was measured for different concentrations of fluorine atoms (from 5×10^{11} to 5×10^{12} molecules cm^{-3}) for both alkanes and methanol showing the same problem of non-linearity on the OH decays.

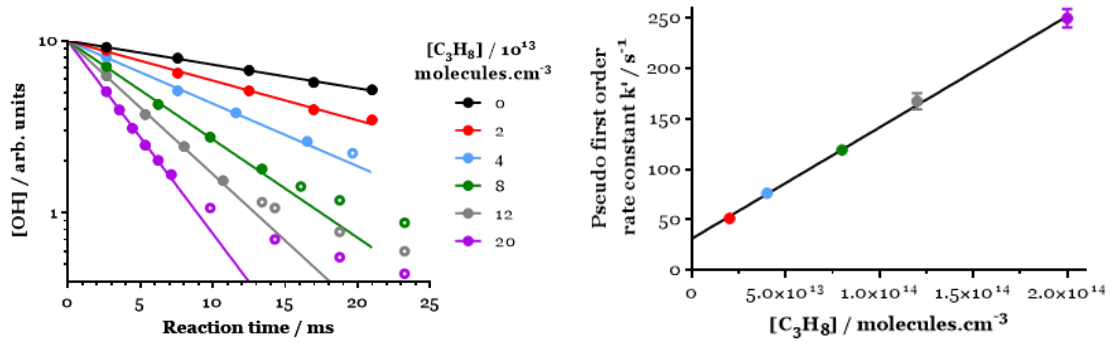

Figure 19: Reaction C_3H_8 + OH:

a) OH fluorescence signal (logarithmic scale) as a function of reaction time, for [F] = 8×10^{11} molecules cm^{-3}, [H_2O]= 2×10^{14} molecules cm^{-3}, [C_3H_8] = 0 – 2×10^{14} molecules cm^{-3}; b) Pseudo-first order rate constant as a function of [C_3H_8]

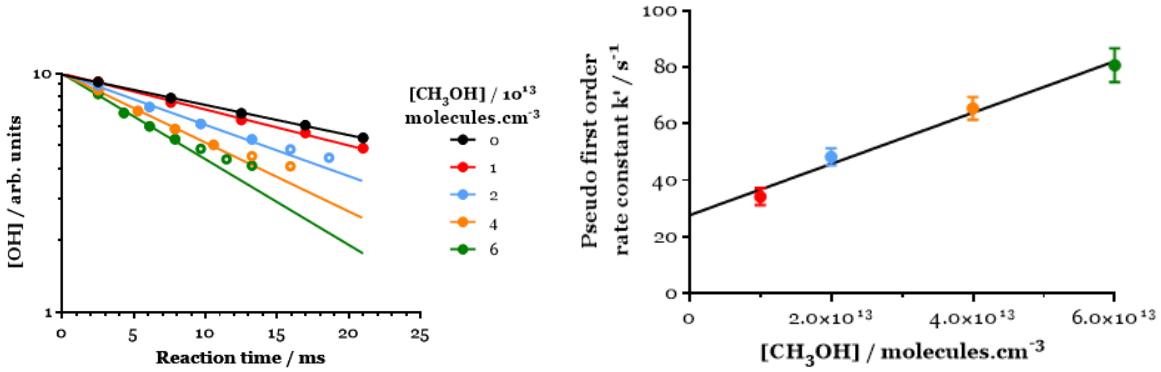

Figure 20: Reaction CH_3OH + OH:

a) OH fluorescence signal (logarithmic scale) as a function of reaction time, for [F] = 8×10^{11} molecules cm^{-3}, [H_2O]= 2×10^{14} molecules cm^{-3}, [CH_3OH] = 0 – 6×10^{13} molecules cm^{-3}; b) Pseudo-first order rate constant as a function of [CH_3OH]

To better understand this phenomenon that might be due to a re-formation of OH radicals from the product of the reaction between OH and a stable molecule containing H atoms, the reaction between OH and a species not containing H atoms: carbon monoxide CO, was studied. The results showed a linear OH decay (logarithmic scale) over the entire reaction time range for all concentrations of CO and a value of the rate constant k_{CO+OH} = (1.59 ± 0.40) × 10^{-13} $cm^3molecule^{-1}s^{-1}$ that was in perfect agreement with data from the literature (Howard & Evenson, 1974; Mulcahy and Smith, 1971).

In an attempt to understand this phenomenon, different hypotheses were investigated:

- *Interferences on the OH LIF signal?*
  This hypothesis was dismissed by systematically scanning the OH $Q_1(1)$ line with measurement of the background with no discharge and measurement off resonance: the signal at longer reaction times is definitely due to OH radicals. Quenching effect was also investigated by measuring the fluorescence decay times at different conditions of concentration and reaction time.

- *Re-formation of OH by photolysis of the reactants or products of the reaction with the LIF excitation laser?*
  This was explored by changing the laser energy (from 0.1 to 3.5 mJ/pulse) and pulse frequency (1 and 10 Hz), in both cases the non-linearity problem still appeared with the same intensity.

- *Heterogeneous reactions on the reactor walls and the optical cell?*
  To change the surface of the reactor walls (normally coated with halocarbon wax), a Teflon tube was introduced into the reactor and Fluoropel (Cytonix Corp., PFC800-1%) was used to coat the optical access arms of the optical cell, both with no improvement on the measurements.

- *Problem of mixing between reactants?*
  This hypothesis was also dismissed by doing different tests at different flow velocities and changing the gas arrival ports in the reactor, with no change in the results.

None of the different tests carried out could explain the observed non-exponential OH decays. All tests seem to show that the OH radicals are reformed along the reaction path within the reactor. In order to understand the observed non-exponential OH decays, the same reactions were studied with their deuterated homologues.

3.1.2. Reactions with deuterated species

The C_3H_8 + OD and CH_3OH + OD reactions were studied and the OD decays were monitored by LIF as a function of reaction time for different concentrations of propane and methanol. The results showed a linear OD decays (logarithmic scale) for all reaction times and for all concentrations of propane and methanol. The rate constants were obtained for both reactions, $k_{C3H8+OD} = (1.56 \pm 0.39) \times 10^{-12}$ $cm^3molecule^{-1}s^{-1}$ (no value in the literature) and $k_{CH3OH+OD} = (8.9 \pm 2.3) \times 10^{-13}$ $cm^3molecule^{-1}s^{-1}$ that is in a good agreement with the value given by McCaulley et al. (McCaulley et al., 1989): $k=(9.5 \pm 1.2) \times 10^{-13}$ $cm^3molecule^{-1}s^{-1}$ at 298 K. During both reactions, OH radicals were also measured by LIF showing OH formation in both cases. Moreover, the results showed that the re-formation of OH relative to its consumption is more intense in the case of CH_3OH compared to C_3H_8 which can possibly explain the fact that the non-exponential behavior appears more rapidly in the case of methanol. The formation of OH seemed then to be linked to the stable reactant containing H atoms (C_3H_8 and CH_3OH).

Then, the CD_3OD + OH reaction was studied to see if the problem appears in this case on the OH signal. The results showed linear OH decays over the entire reaction time and CD_3OD concentration range. A value for the rate constant was estimated, $k_{CD3OD+OH} = (2.5 \pm 0.7) \times 10^{-13}$ $cm^3molecule^{-1}s^{-1}$ at 293 K and lies in the range given in the literature (McCaulley et al., 1989). However, measuring OD radicals during this reaction showed a formation of OD that seems to arise from the CD_3OD. To complete this study, the reaction between CD_3OD and OD was also investigated. The study of this reaction showed a non-linear OD decay for concentration of CD_3OD higher than 4×10^{14} molecules cm^{-3} and no formation of OH. Using the linear part of the decay, the rate constant obtained was $k_{CD3OD+OD} = (1.02 \pm 2.80) \times 10^{-13}$ $cm^3molecule^{-1}s^{-1}$ at 293 K, slightly lower than the rate constant of CD_3OD + OH.

To resume the results for the reactions involving the deuterated species, OH re-formation was observed during the reaction of CH_3OH + OH and CH_3OH + OD (same for C_3H_8) and a re-formation of OD during the reactions CD_3OD + OH and CD_3OD + OD. Thus, this confirms that the problem of non-linearity comes from the species in excess containing H or D atoms which leads to the re-formation of OH or OD radicals.

3.1.3. Monitoring OH and HO_2 radicals

To further investigate this OH re-formation phenomenon, OH (by LIF) and HO_2 (by cw-CRDS) radicals were measured simultaneously during the reaction of CH_3OH + OH in the presence of O_2.

The HO_2 was formed from the following sequence:

$CH_3OH + OH \rightarrow CH_2OH + H_2O$	(R 39)	$k = 9 \times 10^{-13}$ $cm^3molecule^{-1}s^{-1}$ at 298 K
$CH_3O + H_2O$	(R 40)	with $k_{40}/k_{39} = 0.15$ at 298 K
$CH_2OH + O_2 \rightarrow HO_2 + CH_2O$	(R 41)	$k = 9.69 \times 10^{-12}$ $cm^3molecule^{-1}s^{-1}$ at 298 K
$CH_3O + O_2 \rightarrow HO_2 + CH_2O$	(R 42)	$k = 1.9 \times 10^{-15}$ $cm^3molecule^{-1}s^{-1}$ at 298 K

As the reaction (R 42) is very slow, HO_2 radicals are mainly formed from reaction (R 41) and formation rate of HO_2 should follow the consumption rate of OH.

Figure 21 shows an example of the experimental OH decay and HO_2 formation as a function of reaction time during the reaction of $CH_3OH + OH + O_2$. The expected simulated profiles are also plotted (dashed lines) for comparison. The experimental OH decay shows that OH radicals are not totally consumed as it should theoretically be for this condition after a reaction time of 6 ms. Comparatively, we should obtain the maximum of HO_2 concentration at this reaction time and then HO_2 should decrease due to its consumption through secondary reactions. The experimental HO_2 profile does not follow this trend as HO_2 concentration continues to increase. This behaviour suggests again an OH re-formation which leads to this slight increase in HO_2 formation at long reaction time.

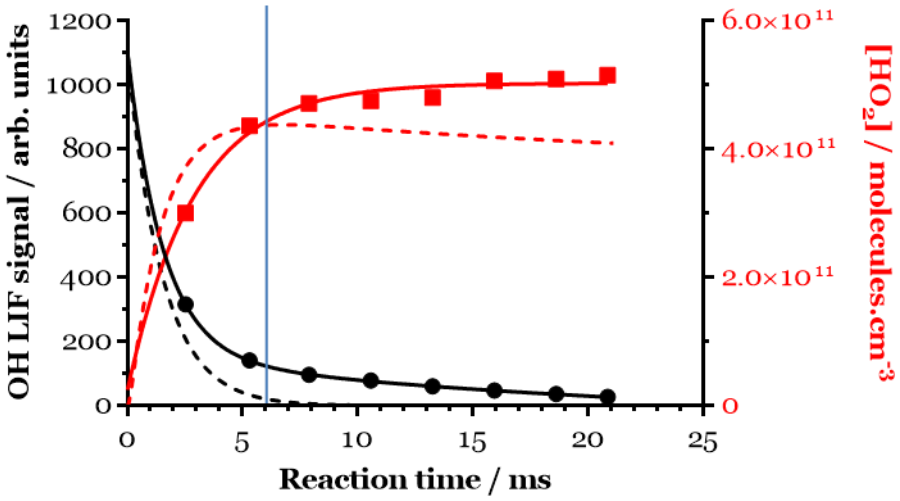

Figure 21: OH LIF signal (black symbols) and HO_2 concentration (red symbols) as a function of reaction time: experiments (circles), simulation (dashed line) for [F] = 3×10^{12} molecules cm^{-3}, [H_2O] = 2.2×10^{14} molecules cm^{-3}, [CH_3OH] = 6×10^{14} molecules cm^{-3} and [O_2] = 1×10^{15} molecules cm^{-3}

To conclude, all the tests showed that the problem of non-linearity is most probably due to an OH re-formation. To test whether the OH generation method can have an influence on the kinetics, other methods were used to generate OH.

3.1.4. Other precursors for the generation of OH radical

Another method was used to generate OH: from the reaction between H atoms and NO_2 (in excess). In this case, the study of the reactions C_3H_8 + OH and CH_3OH + OH showed linear OH decays over the entire reaction time and C_3H_8 or CH_3OH concentration range. The value for the rate constant obtained, $k_{C3H8+OH} = (1.21 \pm 0.31) \times 10^{-12}$ $cm^3 molecule^{-1} s^{-1}$ and $k_{CH3OH+OH} = (9.6 \pm 2.4) \times 10^{-13}$ $cm^3 molecule^{-1} s^{-1}$ at 298 K, were in a good agreement with data from the literature. This was not the case when OH was generated from F + H_2O. These results showed that the OH re-formation also depends on the chosen OH generation method. Thus, the OH re-formation phenomenon seems to be related to the stable species and to the method of generation of the OH radicals. Therefore, this might be due to an unexplained interaction between OH and molecules containing H atoms and F atoms, F_2, H_2O or HF.

Generating OH from H + NO_2 is the mostly used method in the literature compared to F + H_2O, but it was not our first choice to generate OH radicals as our final purpose is to study reactions

between RO_2 and HOx in low NOx (NO and NO_2) conditions. Thus, another method was explored to generate OH radicals from the photolysis of ozone in the presence of water.

Ozone was created by sending a flow of oxygen into an ozone generator (BMT 802N, BMT Messtechnik GmbH) that was placed before the injector. Then, the ozone was mixed with water and photolyzed in the injector by using two UV lamps (λ= 254 nm) placed around the quartz injector. Thus, OH radicals should be generated through the photolysis of ozone O_3 to form an excited oxygen atom $O(^1D)$ (R 1) that reacts with water vapor to form OH (R 3).

$$O_3 + h\nu \rightarrow O(^1D) + O_2 \qquad \text{(R 1)}$$

$$O(^1D) + H_2O \rightarrow 2OH \qquad \text{(R 3)}$$

The signal for O_3 at mass 48 was monitored by mass spectrometry and OH signal by LIF. However, the formation of OH was not observed in any of the tests done. This method was then abandoned.

Following the work performed during F. Kravtchenko's PhD, the objective of my PhD work is to explain the OH re-formation phenomenon which disturbs the kinetic measurement and to find a solution to avoid it. Therefore, new hypotheses were explored: Can heterogeneous reactions occur on the walls of the internal injector or the reactor and form OH radicals that disturb the measurements? Is the formation of F atoms from the reaction $R + F_2 \rightarrow RF + F$ ($R=C_3H_7$ or CH_2OH) react with water reforming OH radicals? Is it due to the formation of O atoms through the reaction of $F + OH \rightarrow O + HF$ reacting with the alkane/alcohol? Is it the formation of helium cations in the microwave discharge reacting with water and reforming OH radicals?

3.2. Heterogeneous reactions?

The OH re-formation phenomenon could be due to possible reactions on the walls of the glass injector or the reactor. Although the reactor internal part is coated by halocarbon wax, it can cause heterogeneous reactions if it was not well coated. Moreover, the outer wall of the internal glass injector is not coated with halocarbon wax. The walls of the internal glass injector and the reactor part were tested.

3.2.1. Reactions on the walls of the internal injector?

The perturbation of the kinetic measurements could be due to the attack of F atoms on the glass injector and possible reactions on the wall of the injector. This hypothesis was explored by

replacing the internal glass injector by a quartz one in an attempt to limit these reactions and obtain better kinetic measurements.

The double injector configuration was used with the external glass injector coated with halocarbon wax (inner wall only) and a quartz internal injector (not coated). Therefore, this configuration minimizes the OH losses at the walls of the injector. Several reactions involving C_3H_8 + OH and CH_3OH + OH were studied using this configuration.

3.2.1.1. C_3H_8 + OH reaction

To study the C_3H_8 + OH reaction, the OH radicals were created in the double injector from the reaction F + H_2O with [F] = 8×10^{11} molecules cm^{-3} and [H_2O] = 2×10^{14} molecules cm^{-3}. Propane was introduced into the reactor in excess with respect to OH ([C_3H_8] between 8×10^{13} and 4×10^{14} molecules cm^{-3}). The OH fluorescence signal was monitored as a function of the reaction time between OH and propane and for different concentrations of propane (Figure 22).

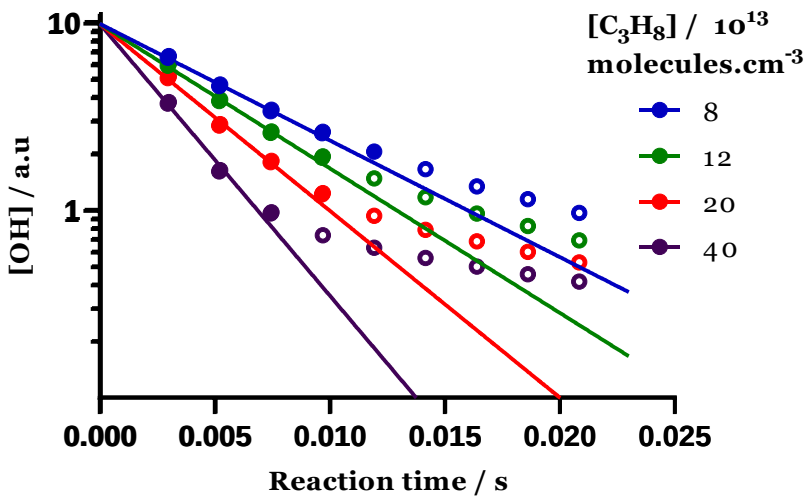

Figure 22: OH fluorescence signal (logarithmic scale) as a function of reaction time for [F]= 8×10^{11} molecules cm^{-3},[C_3H_8]= 8 - 40 × 10^{13} molecules cm^{-3} and [H_2O] = 2×10^{14} molecules cm^{-3}

The results show that the logarithmic decrease of the OH fluorescence signal is not linear over the entire reaction time range (0 - 23 ms). This non-linearity is dependent on the concentration of propane since it is observed more rapidly with higher propane concentration. It is observed from 14 ms when [C_3H_8] = 8×10^{13} molecules cm^{-3} while it shows non-linearity from 9 ms when [C_3H_8] = 4×10^{14} molecules cm^{-3}. The problem of non-linearity seems to appear when about 75% of the OH radicals were consumed.

Figure 23 represents a comparison for these results with the experiments done using the glass internal injector configuration (Kravtchenko, thesis 2019) in exactly the same species concentrations conditions.

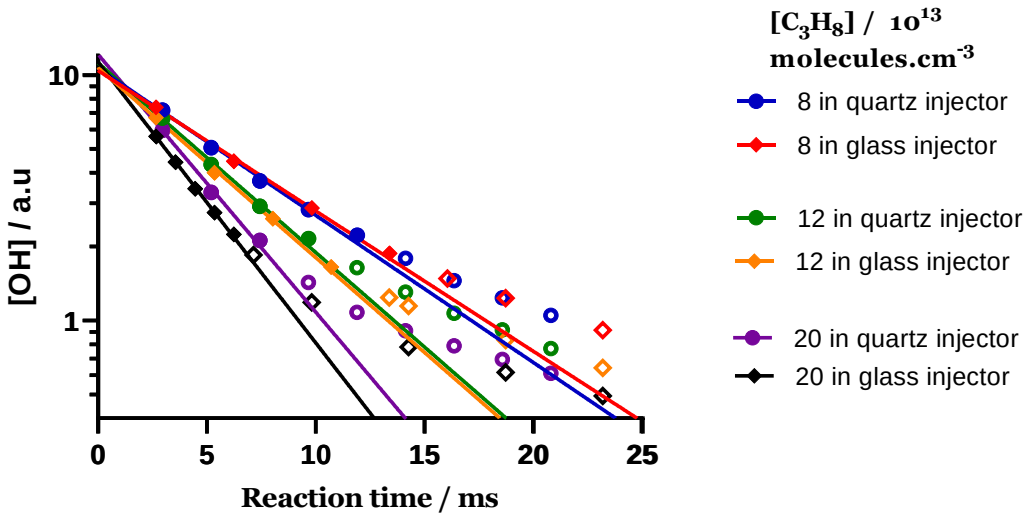

Figure 23: Comparison of the OH fluorescence signal (logarithmic scale) using the quartz or glass internal injector as a function of reaction time for [F] = 8 × 10^{11} molecules cm^{-3}, [C_3H_8] = 8 - 20 × 10^{13} molecules cm^{-3} and [H_2O] = 2 × 10^{14} molecules cm^{-3}

Comparing the OH fluorescence signal (logarithmic scale) using the quartz or glass internal injector for the same concentrations of propane and fluorine shows approximately the same results of non-linearity. Using both configurations shows that the non-linearity problem appears more rapidly with higher concentration of propane.

Then, the CH_3OH + OH reaction was also studied using this quartz internal injector configuration.

3.2.1.2. CH_3OH + OH reaction

The CH_3OH + OH reaction was studied under the same experimental conditions as for C_3H_8 + OH reaction with [F] = 8×10^{11} molecules cm^{-3}, [H_2O] = 2 × 10^{14} molecules cm^{-3} and [CH_3OH] = 0 - 4×10^{14} molecules cm^{-3}. Figure 24 represents the OH fluorescence signal (logarithmic scale) as a function of the reaction time for different concentrations of methanol.

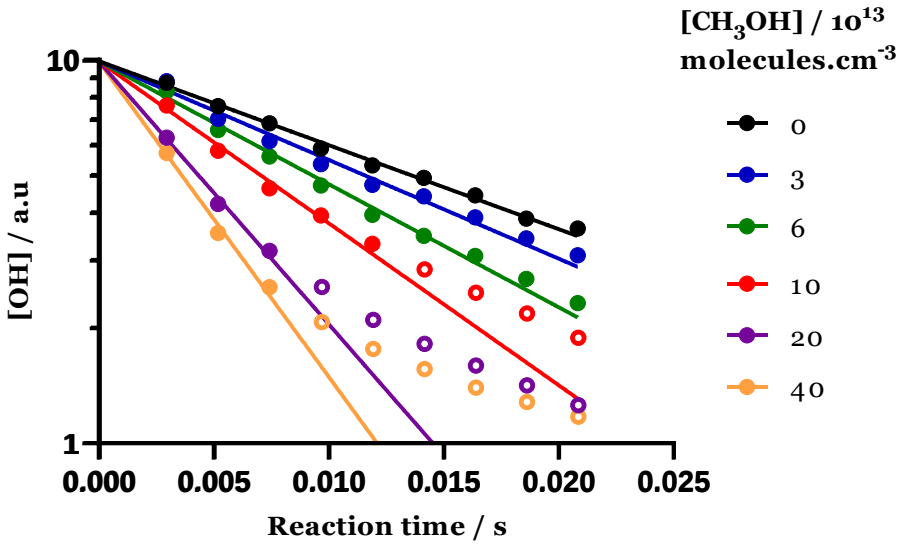

Figure 24: OH fluorescence signal (logarithmic scale) as a function of reaction time for [F]= 8×10^{11} molecules cm^{-3}, $[H_2O] = 2 \times 10^{14}$ molecules cm^{-3} and $[CH_3OH] = 0 - 4 \times 10^{14}$ molecules cm^{-3}

As for C_3H_8 + OH reaction, the logarithmic decrease of the OH fluorescence signal is not linear over the entire reaction time range for high concentrations of methanol, $[CH_3OH] > 6\times10^{13}$ molecules cm^{-3}. Similarly, the non-linearity is dependent on the concentration of methanol since it is observed more rapidly with higher methanol concentration. Using the slopes for which the decays are linear from Figure 24, a plot of the pseudo-first order rate constant k' as a function of $[CH_3OH]$ (Figure 25) returns a rate constant of $k_{CH3OH+OH} = (5.9 \pm 0.6) \times 10^{-13}$ $cm^3molecule^{-1}s^{-1}$ that is slightly lower than the data in the literature.

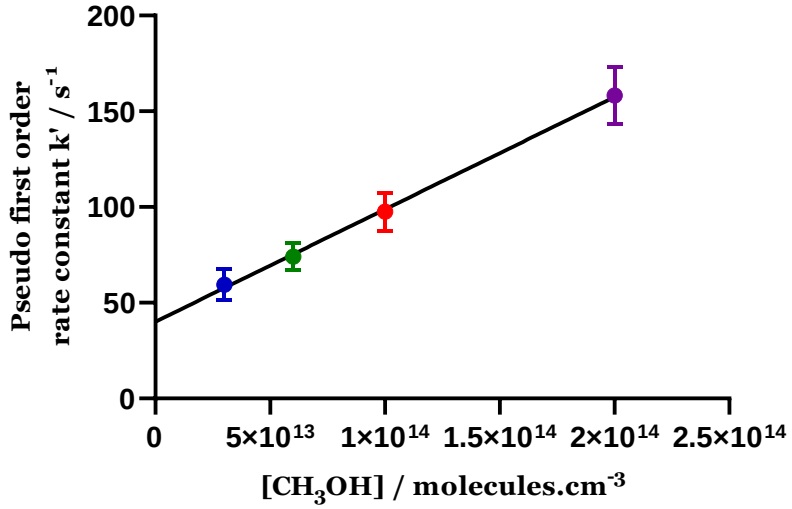

Figure 25: Pseudo-first order rate constant k' as a function of [CH_3OH] (0 – 2 × 10^{14} molecules cm^{-3})

The results of these experiments are not compared with the experiments done using the glass internal injector configuration since it is not done in exactly the same species concentrations conditions.

Then, other tests were done by removing the quartz internal injector where the experiments were performed in a single glass injector. Reactions of C_3H_8 + OH and CH_3OH + OH were tested using this configuration (OH generated in the single injector) to compare with the double injector configuration.

3.2.1.3. Reactions without internal injector

The reactions C_3H_8 + OH and CH_3OH + OH were studied using the single injector configuration to compare the results with the double injector. Unfortunately, in both cases the non-linearity phenomenon still appeared. An example is presented in Figure 26 for the reaction of C_3H_8 + OH for [F] = 5×10^{12} molecules cm^{-3}, [H_2O] = 2 × 10^{14} molecules cm^{-3}, and [C_3H_8] = 2 × 10^{14} molecules cm^{-3} with and without internal injector.

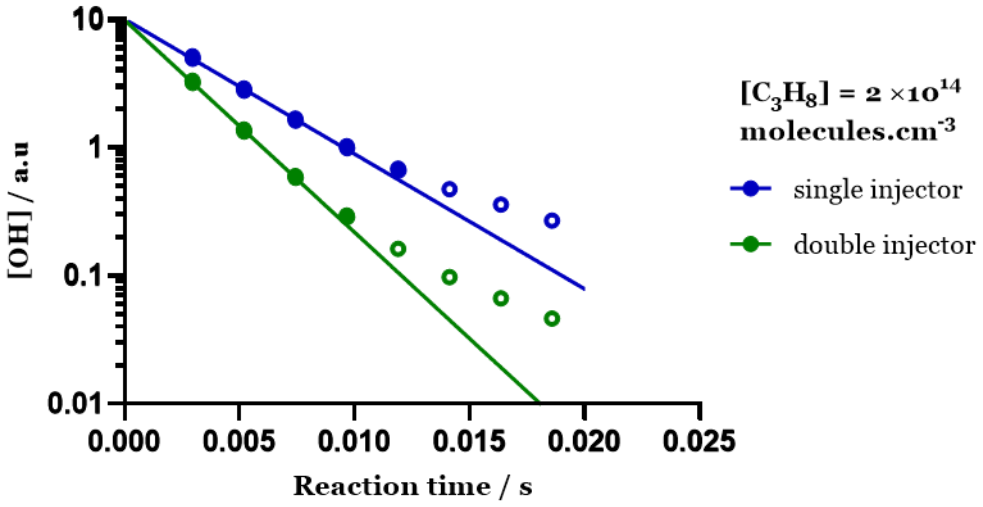

Figure 26: OH fluorescence signal (logarithmic scale) as a function of reaction time for [F] = 5 × 10^{12} molecules cm^{-3} and [C_3H_8] =2 × 10^{14} molecules cm^{-3}, with the double injector (green symbols) and with the single injector (blue symbols) configuration

Thus, replacing the glass internal injector with a quartz one and removing it do not change the results as it also shows a non-linearity problem for the C_3H_8/CH_3OH + OH reactions.

Then, experiments were performed to check if the problem could arise from reactions occurring on the walls of the reactor.

3.2.2. Reactions on the walls of the stainless steel reactor?

Heterogeneous reactions could take place on the walls of the reactor and disturb the kinetic measurements. Different tests were performed to check if the OH re-formation phenomenon was due to heterogeneous reactions on the walls of the reactor.

The first test done was to add O_2 into the reactor to check if there is an improvement on the kinetic measurements and the second test done was to replace the stainless steel reactor by a glass one.

3.2.2.1. Effect of adding O_2 in the reactor

Tests were performed by adding O_2 into the reactor, following the work of Chuong and Stevens (Chuong & Stevens, 2003) who also observed non-exponential pseudo-first order decays of OH during the reaction of Methyl Vinyl Ketone (MVK) and methacrolein with OH (generated from the reaction F + H_2O) in a Halocarbon wax coated reactor. The authors explain that the problem could be attributed to MVK and methacrolein catalysed-OH wall reactivity. This effect was found to be minimized by adding ~ 10% of O_2 into the reactor. The authors suggest that fluorine reduces the polarity of the walls by removing hydrogen atoms from the halocarbon wax coating, while O_2 may inhibit these active sites on the walls.

The C_3H_8 + OH reaction was studied by creating OH in the double injector from the reaction F + H_2O with [F] = 8×10^{11} molecules cm^{-3} and [H_2O] = 2×10^{14} molecules cm^{-3}. Oxygen and propane were introduced into the reactor with [O_2] = 1×10^{15} molecules cm^{-3} and [C_3H_8] = 0 and 2×10^{14} molecules cm^{-3}. The OH fluorescence signal was monitored as a function of the reaction time for different concentrations of propane, with and without adding O_2, as presented in Figure 27.

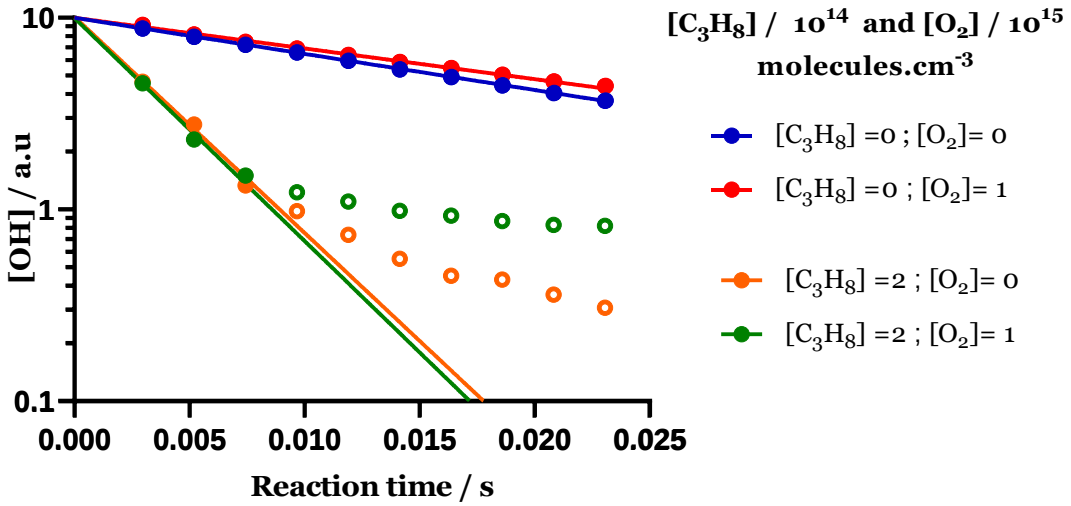

Figure 27: OH fluorescence signal (logarithmic scale) as a function of reaction time for [F] = 8×10^{11} molecules cm^{-3} ,[C_3H_8] = 0 and 2×10^{14} molecules cm^{-3} and [H_2O] = 2×10^{14} molecules cm^{-3} with and without adding O_2 in the reactor

The results show a value for k_{wall} = 43.5 ± 0.4 s^{-1} (for [C_3H_8] = 0) without adding O_2 in the reactor, this value decreases to k_{wall} = 37 ± 2 s^{-1} upon the addition of O_2 into the reactor. However, upon adding propane, the results show a non-linear decay for the OH radical with and without adding oxygen into the reactor. In both cases, the non-linearity problem appears at the same reaction time (t = 9.7 ms). Moreover, there is a higher re-formation for OH radical when oxygen is added. Thus, the addition of oxygen into the reactor shows a decrease in the value of the k_{wall} and a higher re-formation of OH radical when propane is added.

Performing the same experiment using a higher concentration of oxygen added into the reactor, [O_2] = 6×10^{15} molecules cm^{-3}, show the same results. Thus, adding oxygen into the reactor shows more OH re-formation that might be due to a formation of new species that is disturbing the kinetic measurement.

To check if there is formation of new species upon the addition of oxygen, a mass spectrometry scan was performed for masses between 0 and 120 when oxygen was added to propane and OH. The results showed only a signal at mass 32 corresponding to oxygen and a signal at mass 29 corresponding to propane. Hence, there was no detectable product by the mass spectrometry.

To conclude, the addition of oxygen did not solve the problem of non-linearity, so further tests were performed by replacing the stainless steel reactor by a glass one.

3.2.2.2. Reactions using glass reactor

The stainless steel reactor (coated with Halocarbon wax) was replaced by a glass reactor (also coated with Halocarbon wax) assuming that heterogeneous reactions could take place on the walls of the reactor (interactions between Halocarbon wax and stainless steel or defect in the coating with Halocarbon wax). Reactions involving C_3H_8 + OH and CH_3OH + OH were studied using the double injector configuration.

The C_3H_8 + OH reaction was studied under exactly the same experimental conditions as for using the stainless steel reactor with [F] = 8×10^{11} molecules cm^{-3}, [H_2O] = 2×10^{14} molecules cm^{-3}, and [C_3H_8] = 8×10^{13} - 4×10^{14} molecules cm^{-3}. Figure 28 represents the OH fluorescence signal monitored as a function of reaction time for using the glass reactor (left graph) and for using the stainless steel reactor (right graph).

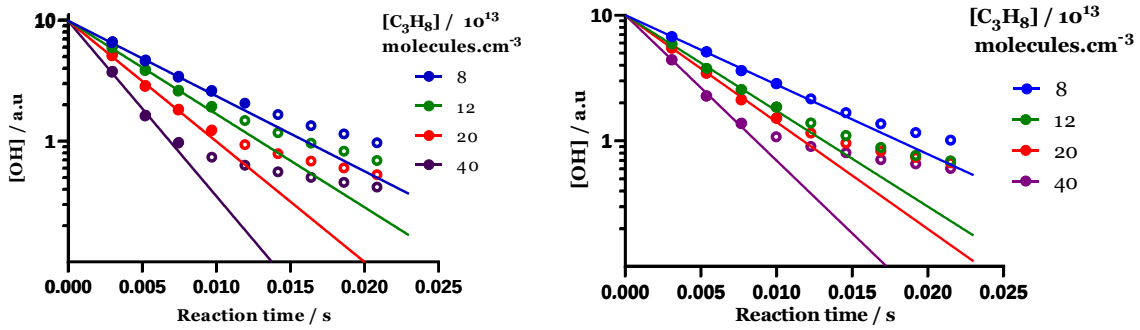

Figure 28: OH fluorescence signal (logarithmic scale) for using the glass reactor (left graph) and the stainless steel reactor (right graph) as a function of reaction time for C_3H_8 + OH.

Comparing the OH fluorescence signal (logarithmic scale) using the stainless steel or glass reactor for the same concentrations of propane and fluorine shows the same results of non-linearity. Using both configurations shows that the non-linearity problem appears when about 75% of the OH radicals were consumed and it appears more rapidly with higher concentration of propane.

As for C_3H_8 + OH reaction, the CH_3OH + OH reaction was also studied using the glass reactor under the same experimental conditions as for using the stainless steel reactor with [F] = 8×10^{11} molecules cm^{-3}, [H_2O] = 2×10^{14} molecules cm^{-3} and [CH_3OH] = 0 - 4×10^{14} molecules cm^{-3}. Figure 29 represents the OH fluorescence signal monitored as a function of reaction time for using the glass reactor (left graph) and for using the stainless steel reactor (right graph).

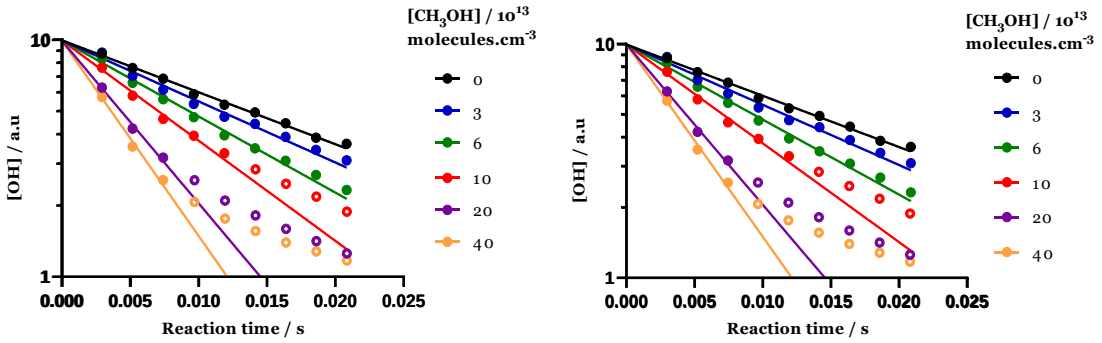

Figure 29: OH fluorescence signal (logarithmic scale) for using the glass reactor (left graph) and the stainless steel reactor (right graph) as a function of reaction time for CH_3OH + OH.

Same as for C_3H_8 + OH, comparing the OH fluorescence signal (logarithmic scale) using the stainless steel or glass reactor for the same concentrations of methanol and fluorine shows the same results of non-linearity. Using both configurations shows that the non-linearity problem is observed more rapidly with higher methanol concentration.

Thus, replacing the stainless steel reactor with a glass one does not solve the problem.

In conclusion, these different tests did not improve the kinetics measurements. The heterogeneous reactions on the walls of the reactor and the internal injector did not explain the non-linearity problem.

3.3. Re-formation of OH from F atoms?

Another hypothesis is that the re-formation of OH could be due to the reaction of water present in the reactor and F atoms that could be formed through the reaction R + F_2 → RF + F (R=C_3H_7 or CH_2OH) where F_2 (which is not totally converted to F atoms in the discharge) react with C_3H_7 (in the case of propane) or CH_2OH (in the case of methanol). This hypothesis was explored by adding F_2 into the reactor during the study of the reaction of C_3H_8 + OH (no rate constant for the reaction of C_3H_7 + F_2 and CH_2OH + F_2 in the literature). Then adding F_2 should increase the OH re-formation phenomenon.

The C_3H_8 + OH reaction was studied by creating OH in the double injector (quartz internal injector) from the reaction F + H_2O with [F] = 8×10^{11} molecules cm^{-3} and [H_2O] = 2×10^{14} molecules cm^{-3}. Fluorine and propane were introduced into the reactor with [F_2] = 5.7×10^{11} molecules cm^{-3} and [C_3H_8] = 0 - 4×10^{14} molecules cm^{-3}. The OH fluorescence signal was monitored as a function of

the reaction time for different concentrations of propane, with and without adding F_2, as presented in Figure 30.

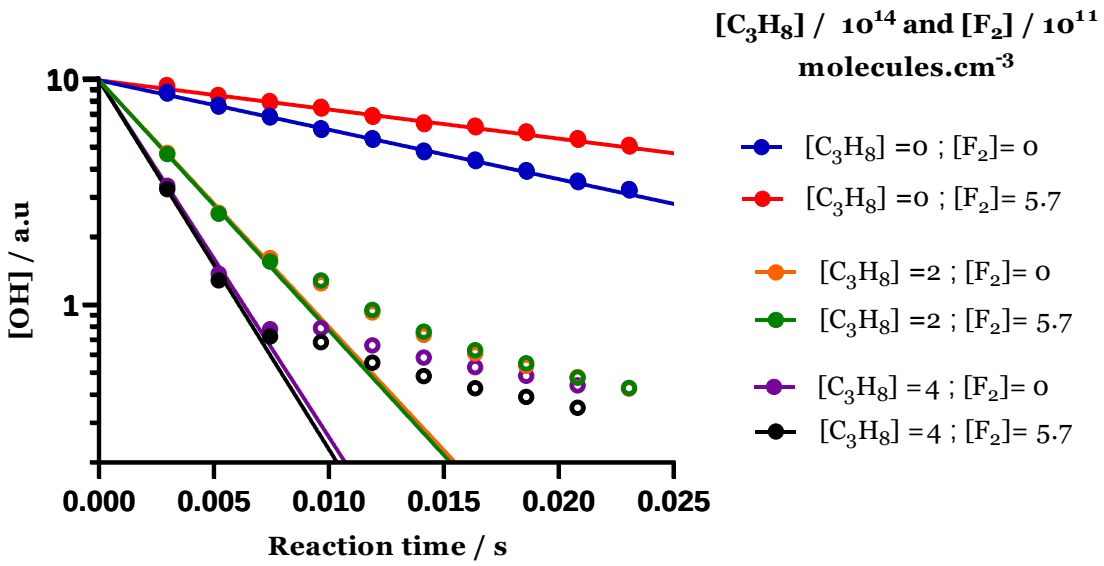

Figure 30: OH fluorescence signal (logarithmic scale) as a function of reaction time for [F] = 8×10^{11} molecules cm^{-3}, [C_3H_8] = 0 - 4×10^{14} molecules cm^{-3} and [H_2O] = 2×10^{14} molecules cm^{-3} with and without adding F_2 in the reactor

The results show a value for $k_{wall} = 50.5 \pm 1.9\ s^{-1}$ (for [C_3H_8] = 0) without adding F_2 in the reactor, this value decreases to $k_{wall} = 29.8 \pm 2\ s^{-1}$ upon the addition of F_2 into the reactor. However, for [C_3H_8] = 2×10^{14} and 4×10^{14} molecules cm^{-3}, the results show a non-linear decay for the OH radical with and without adding fluorine into the reactor. In both cases, the non-linearity problem appears at the same reaction time. Thus, the addition of fluorine into the reactor shows a decrease in the value of the k_{wall} (not explained) but it does not show any effect on the OH decay when propane is added.

Performing the same experiment using higher concentration of fluorine added into the reactor, [F_2] = 2.5×10^{12} molecules cm^{-3}, shows the same results.

Then the problem does not seem to come from the reaction $R + F_2 \rightarrow RF + F$ that could reform OH by the reaction $F+H_2O \rightarrow OH+HF$.

3.4. Re-formation of OH from O atoms?

A possible explanation could come from the formation of O atoms in the external injector from the reaction between F atoms and OH radicals formed ($F + OH \rightarrow O + HF$). O atoms can then react

with the reactant or products of the reaction between alkane/alcohol and OH to reform OH (k_{C3H8+O} = 2.8 × 10^{-15} $cm^3molecule^{-1}s^{-1}$ (Tsang, 1988) and $k_{CH3OH+O}$ = 7.9 × 10^{-15} $cm^3molecule^{-1}s^{-1}$ (Keil et al., 1981)). As water is naturally present everywhere in the injector and the reactor, a small amount of OH radicals can be already formed in the outer injector from the reaction F + H_2O → OH + HF, as shown in Figure 31. Then a part of F atoms that are not converted to OH because the concentration of "natural" water is not high enough to convert all F atoms, can react with OH to form O atoms.

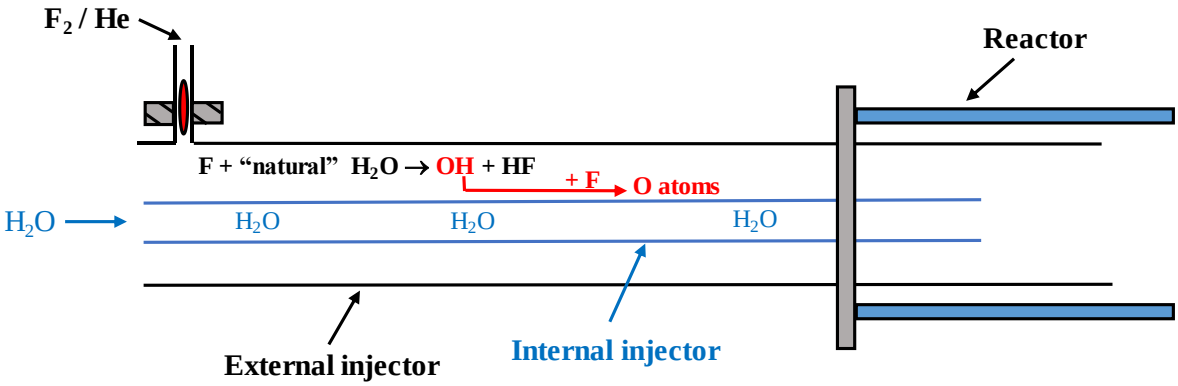

Figure 31: Schematic view of the double injector configuration and possible formation of O atoms

The first idea was to mix rapidly F atoms with an excess of water to reduce the effect of the reaction F + OH that could disturb the measurements, and reduce OH loss in the injector. This was done using a smaller single glass injector.

3.4.1. Reactions using small glass injector

In this part, a small single glass injector with length 10 cm (Figure 32), coated with halocarbon wax was used instead of the long double injector with length 77 cm. The reactions C_3H_8 + OH/OD and CH_3OH + OH/OD were studied using this small glass injector configuration. In this configuration, the injector cannot be moved in the reactor (as it is too short) then experiments were performed at a fixed reaction time t = 33 ms.

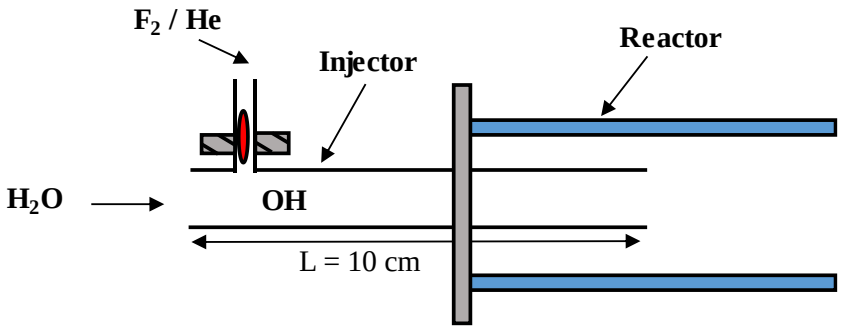

Figure 32: Schematic view of the small single injector configuration

3.4.1.1. C_3H_8 + OH reaction

To study the reaction of C_3H_8 + OH, the OH radicals were created in the small injector from the reaction F + H_2O with [F] = 8×10^{11} molecules cm^{-3} and [H_2O] = 2×10^{14} molecules cm^{-3}. Propane was introduced into the reactor in excess with respect to OH ([C_3H_8] between 2×10^{13} and 9×10^{14} molecules cm^{-3}). The OH fluorescence signal was monitored as a function of propane concentration at reaction time t = 33 ms.

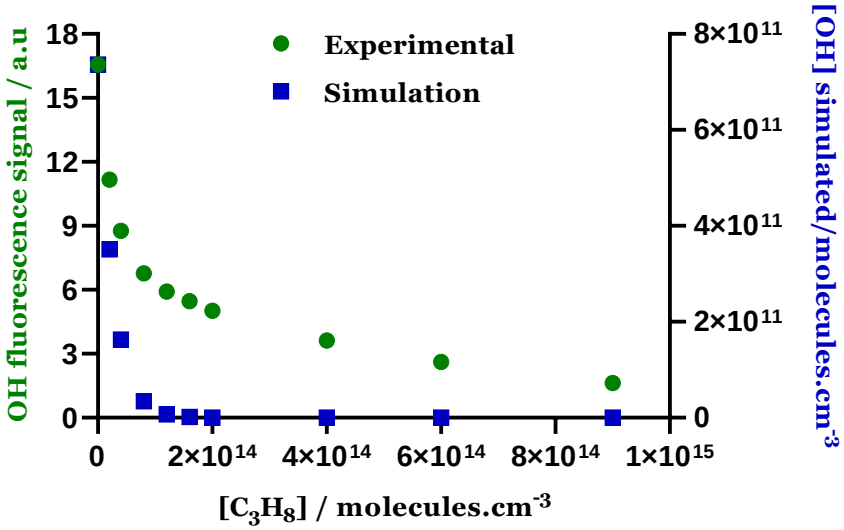

Figure 33: Comparison of the experimental OH LIF signal and the concentration of [OH] obtained by simulation for [F] = 8×10^{11} molecules cm^{-3} and [H_2O] = 2×10^{14} molecules cm^{-3} as a function of [C_3H_8], at t = 33 ms

Figure 33 compares the experimental fluorescence signal and the concentration of OH calculated by simulation as a function of [C_3H_8]. The theoretical results show that more than 99% of OH should be consumed when [C_3H_8] > 1.2×10^{14} molecules cm^{-3}, but this is not the case

experimentally: as it shows only 65% of OH was consumed when $[C_3H_8] = 1.2 \times 10^{14}$ molecules cm^{-3}. This shows that a re-formation of OH radicals is occurring also in this configuration. Thus, the problem of the OH re-formation is still appearing even by reducing the possible influence of the reaction F+OH and loss of OH in the injector. To confirm that there was a re-formation of OH radicals, the same experiment was carried out using the deuterated homologue of the OH radical.

3.4.1.2. C_3H_8 + OD reaction

The C_3H_8 + OD reaction was studied under the same experimental conditions as for C_3H_8 + OH with $[F] = 8\times10^{11}$ molecules cm^{-3}, $[D_2O] = 2 \times 10^{14}$ molecules cm^{-3} and $[C_3H_8] = 0 - 4 \times 10^{14}$ molecules cm^{-3}. Figure 34 represents the OH fluorescence signal as a function of propane concentration at a fixed reaction time (t = 33 ms).

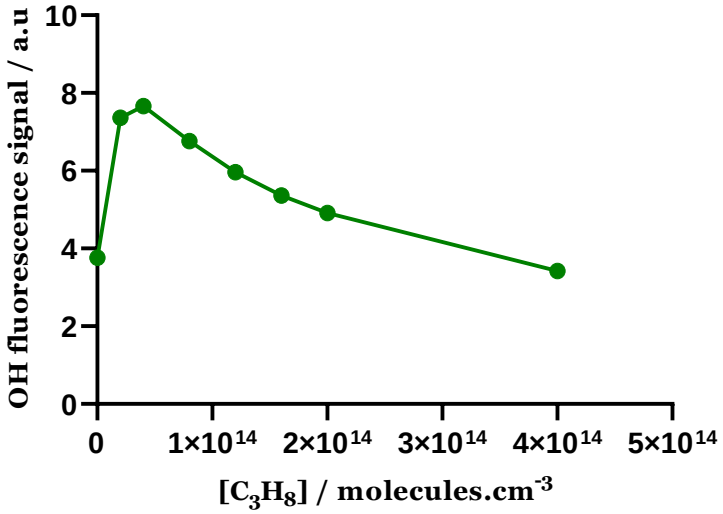

Figure 34: OH fluorescence signal for $[F] = 8 \times 10^{11}$ molecules cm^{-3} and $[D_2O] = 2 \times 10^{14}$ molecules cm^{-3}as a function of $[C_3H_8]$ during the reaction C_3H_8 + OD

The results show an OH fluorescence signal at $[C_3H_8] = 0$ since "natural" water is present in the reactor: $[H_2O] = 1 \times 10^{13}$ molecules cm^{-3} (Kravtchenko, thesis 2019). Although this concentration of H_2O is much lower than that of D_2O, a small part of the F atoms created from the microwave discharge react with H_2O to form OH radicals. Moreover, the results show a formation of OH radicals when propane was introduced into the reactor and this formation is dependent on the propane concentration. The OH fluorescence signal shows an increase when $[C_3H_8] < 4 \times 10^{13}$ molecules cm^{-3}. Then, for higher propane concentrations, a consumption of OH was observed. This

is probably due to the fact that the OH radicals formed are re-consumed by propane at higher concentrations.

These results confirm that the OH radicals are formed during the C_3H_8 + OD reaction since, theoretically, the OH fluorescence signal should only show a decrease upon the addition of propane into the reactor and no formation of OH radical should appear. The same kind of experiments was then performed with the reactions CH_3OH + OH and CH_3OH + OD.

3.4.1.3. CH_3OH + OH reaction

To study the reaction CH_3OH + OH, the OH radicals were created in the injector from the reaction of F + H_2O with [F] = 5×10^{12} molecules cm^{-3} and [H_2O] = 2×10^{14} molecules cm^{-3}. Methanol was introduced into the reactor with [CH_3OH] = 0 to 4×10^{14} molecules cm^{-3}. The OH fluorescence signal was monitored as a function of methanol concentration at a fixed reaction time (t = 33 ms). Figure 35 compares the experimental OH LIF signal and the concentration of OH calculated by simulation.

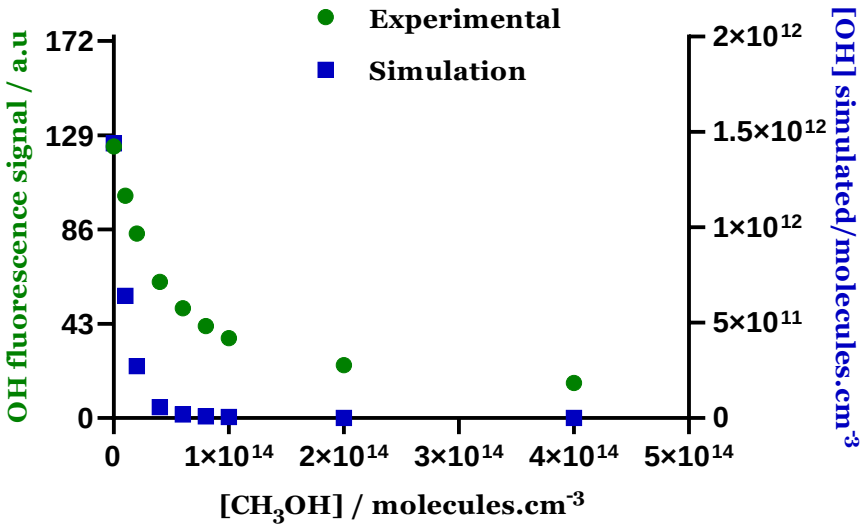

Figure 35: Comparison of the experimental OH LIF signal and the concentration of [OH] obtained by simulation for [F] = 5×10^{12} molecules cm^{-3} and [H_2O] = 2×10^{14} molecules cm^{-3} as a function of [CH_3OH]

The theoretical results show that more than 99% of OH should be consumed when [CH_3OH] > 6×10^{13} molecules cm^{-3}, but this was not the case experimentally as it shows only 60% of OH consumption when [CH_3OH] = 6×10^{13} molecules cm^{-3}. The experimental results did not show a

total consumption for OH radical at high concentration of methanol that confirms that there is an OH re-formation.

Performing the same experiment at a different initial concentration of F, [F] = 8×10^{11} molecules cm^{-3} showed the same result where there was no total consumption of the OH radicals at high concentration of methanol.

3.4.1.4. CH_3OH + OD reaction

CH_3OH + OD reaction was studied under the same experimental conditions as for CH_3OH + OH with [F] = 5×10^{12} molecules cm^{-3}, [D_2O] = 2×10^{14} molecules cm^{-3} and [CH_3OH] = 0 - 4×10^{14} molecules cm^{-3}. Figure 36 represents the OH fluorescence signal as a function of methanol concentration at a fixed reaction time (t = 33 ms).

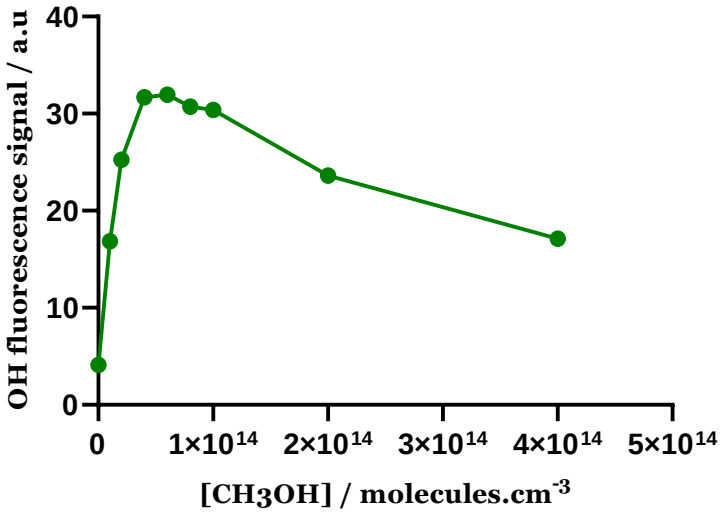

Figure 36: OH fluorescence signal for [F] = 5×10^{12} molecules cm^{-3} and [D_2O] = 2×10^{14} molecules cm^{-3}as a function of [CH_3OH] during the reaction CH_3OH + OD

These results are similar to those for C_3H_8 + OD where an OH fluorescence signal was observed without introducing methanol into the reactor, due to the presence of "natural" water. The formation of OH increases with [CH_3OH] until it reaches a maximum at [CH_3OH] = 6×10^{13} molecules cm^{-3}. Then, for higher methanol concentration, a consumption of OH was observed due to its reaction with CH_3OH. These results show that the OH radicals were also formed during the CH_3OH + OD reaction since, theoretically, the OH fluorescence signal should only show a decrease upon the addition of methanol into the reactor and no formation should appear.

Performing the same experiment at a different initial concentration of F, [F] = 8×10^{11} molecules cm^{-3} shows the same result.

Comparing these results to the formation of OH radicals during C_3H_8 + OD reaction shows that the signal of OH was higher in the case of methanol than that for propane for the same initial concentration of fluorine. This shows again that the problem of OH re-formation is more pronounced in the case of CH_3OH compared to C_3H_8.

In conclusion, using the small glass injector showed the same problem of OH re-formation, thus the problem appears even if F atoms and water are quickly mixed (to reduce the possible O atom formation from F +OH reaction) and OH radical loss is reduced in the single small injector.

The second idea was to add NO_2 in the reactor to scavenge the O atoms as mentioned by the work of (Bedjanian et al., 2001). Bedjanian et al. measured the rate constant of the reaction BrO + OH using both OH generation methods ($F+H_2O$ and $H+NO_2$), however in experiments using $F + H_2O$, NO_2 was also introduced into the reactor to scavenge the O atoms that can possibly be formed from the reaction of F + OH $\rightarrow$ O + HF (and OH+OH$\rightarrow$ $O+H_2O$), and could lead subsequently to the generation or consumption of BrO radicals through the reactions Br_2 + O $\rightarrow$ BrO + Br and BrO + O $\rightarrow$ Br + O_2. In these conditions, they found similar rate constants by generating OH either from H + NO_2 or F + H_2O (+NO_2).

In our conditions, as previously, we suppose that O atoms could react with reactants or products of the reaction between propane + OH and methanol + OH to reform OH.

3.4.2. Effect of adding NO_2 in the reactor

Following the work of (Bedjanian et al., 2001), the effect of adding NO_2 on C_3H_8 + OH and CH_3OH + OH reactions were studied.

3.1.2.1. C_3H_8 + OH reaction

The C_3H_8 + OH reaction was studied by creating OH in the double injector from the reaction F + H_2O and adding propane and NO_2 into the reactor.

First the OH fluorescence signal was measured as a function of NO_2 concentration without adding propane, and at a fixed reaction time (2 ms). Results are presented in Figure 37.

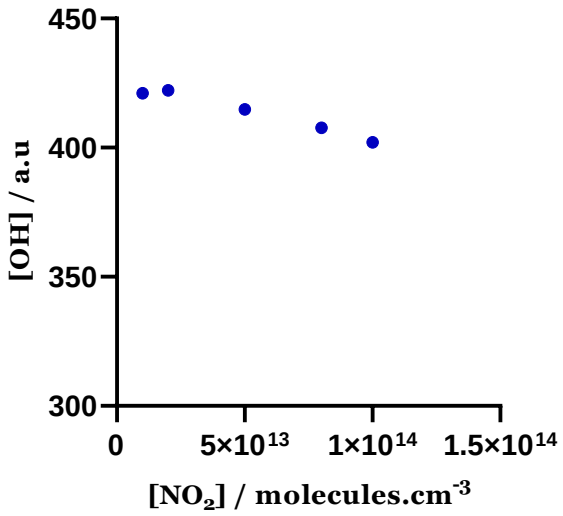

Figure 37: OH fluorescence signal as a function of [NO_2]

The results show that for [NO_2] > 1×10^{13} molecules cm^{-3}, the OH signal decreases. This decrease is due to the reaction between NO_2 and OH (R 43) (Dransfield et al., 1999), which consumes the formed OH radicals.

$$NO_2 + OH + M \rightarrow HONO_2 + M \qquad \text{(R 43)}$$

Thus, the C_3H_8 + OH reaction was studied using [NO_2] = 1×10^{13} molecules cm^{-3} with different concentrations of propane, [C_3H_8] = 0 - 2×10^{14} molecules cm^{-3}, and under the same experimental conditions as before with [F] = 8×10^{11} molecules cm^{-3} and [H_2O] = 2×10^{14} molecules cm^{-3}. Figure 38 represents the OH fluorescence signal monitored as a function of the reaction time for different concentrations of propane.

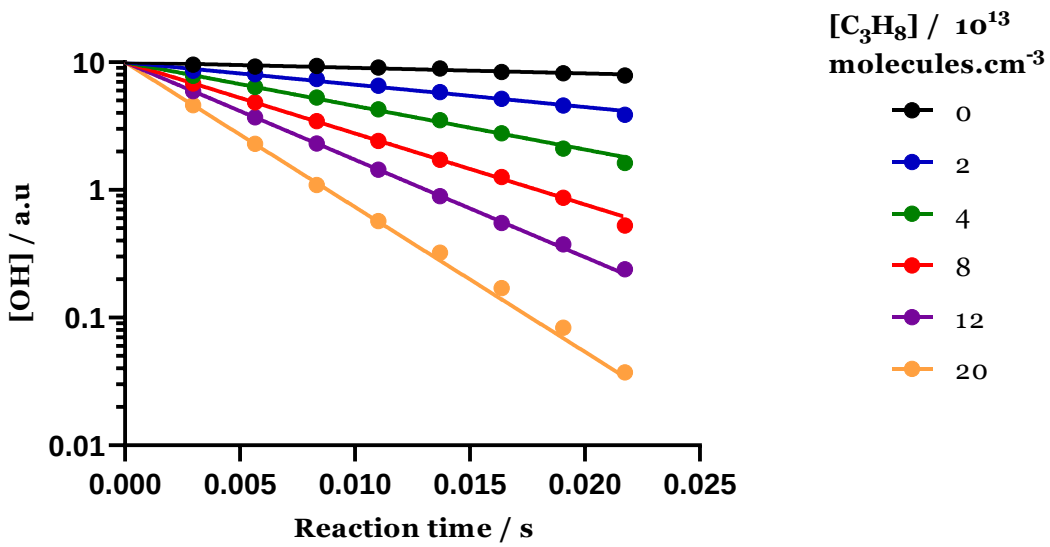

Figure 38: OH fluorescence signal (logarithmic scale) as a function of reaction time for [F] = 8×10^{11} molecules cm^{-3}, $[C_3H_8] = 0 - 2 \times 10^{14}$ molecules cm^{-3}, in the presence of $[NO_2] = 1 \times 10^{13}$ molecules cm^{-3}

The OH decay is linear over the entire reaction time range and for all concentrations of $[C_3H_8]$. From Figure 38, a plot of the pseudo-first order rate constant k' as a function of $[C_3H_8]$ (Figure 39) returns a rate constant of $k_{C3H8+OH} = (1.2 \pm 0.2) \times 10^{-12}$ $cm^3 molecule^{-1} s^{-1}$ at 293 K.

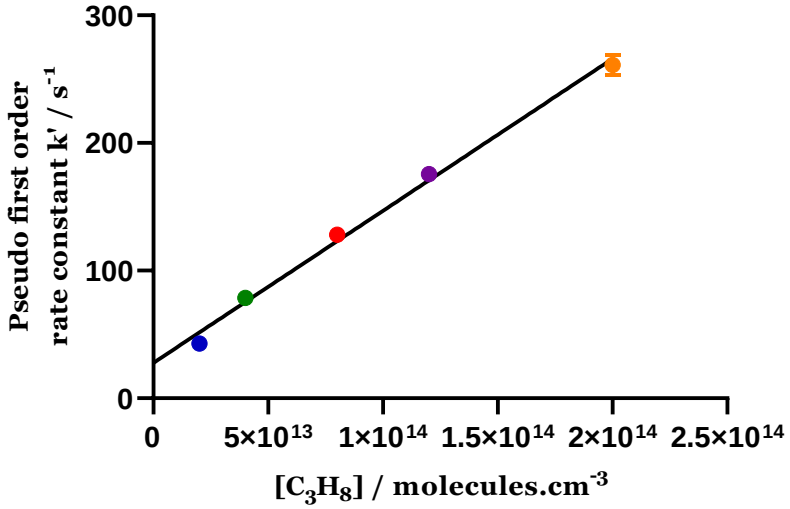

Figure 39: Pseudo-first order rate constant k' as a function of $[C_3H_8]$ ($0 - 2 \times 10^{14}$ molecules cm^{-3}) in the presence of $[NO_2] = 1 \times 10^{13}$ molecules cm^{-3}

Hence, the addition of NO_2 in the reactor seems to solve the problem observed in the work of (Kravtchenko, thesis 2019) (see Figure 19) where the non-linearity problem appears for $[C_3H_8]$ >

8×10^{13} molecules cm^{-3}. However, performing the same experiment for $[C_3H_8] = 2 \times 10^{14}$ molecules cm^{-3}, using higher concentration of fluorine and NO_2, $[F] = 5\times10^{12}$ molecules cm^{-3} and $[NO_2] = 4 \times 10^{13}$ molecules cm^{-3}, shows a non-linear OH decay at high reaction time.

Then, the CH_3OH + OH reaction was also studied by adding NO_2 in the reactor to see if the same effect can be observed.

3.4.2.2. CH_3OH + OH reaction

The CH_3OH + OH reaction was studied using the following conditions in the injector: $[F] = 5\times10^{12}$ molecules cm^{-3} and $[H_2O] = 2 \times 10^{14}$ molecules cm^{-3}. Methanol and nitrogen dioxide were introduced into the reactor with $[NO_2] = 4 \times 10^{13}$ molecules $cm^{-3}$and $[CH_3OH] = 0 - 6 \times 10^{14}$ molecules cm^{-3}. The OH fluorescence signal was monitored as a function of the reaction time for different concentrations of methanol (Figure 40).

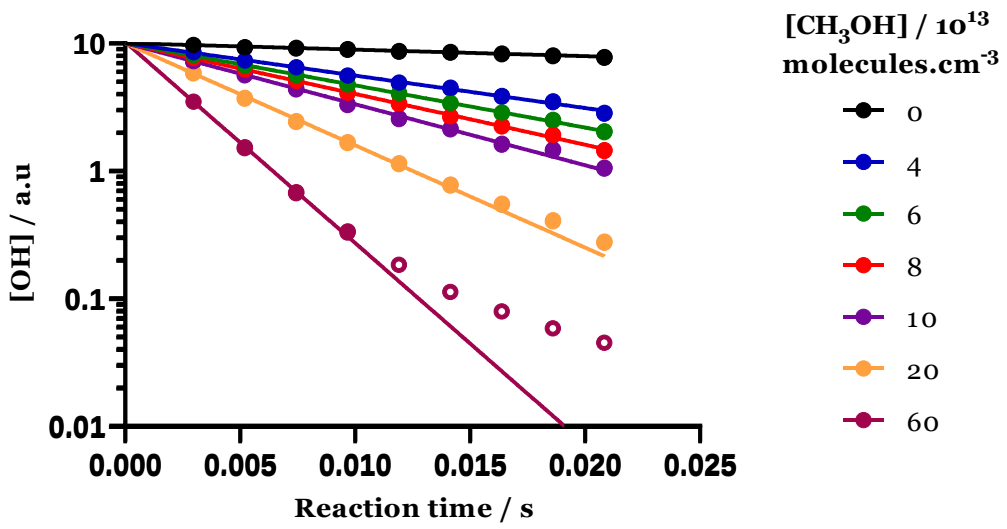

Figure 40: OH fluorescence signal (logarithmic scale) as a function of reaction time for $[F] = 5 \times 10^{12}$ molecules cm^{-3}, $[CH_3OH] = 0 - 6 \times 10^{14}$ molecules cm^{-3}, in the presence of $[NO_2] = 4 \times 10^{13}$ molecules cm^{-3}

As for C_3H_8 + OH, the OH decay is linear over the entire reaction time range for $[CH_3OH] < 2 \times 10^{14}$ molecules cm^{-3}, when NO_2 is added in the reactor. However, the non-linearity behavior appears at higher concentration of methanol, $[CH_3OH] = 6 \times 10^{14}$ molecules cm^{-3} (performed on another day), after 95% of OH consumption. This non-linearity behavior appears more rapidly without adding NO_2 where it appears after 60% of OH consumption. Using the concentrations that show a linear OH decay ($[CH_3OH]$ between 4×10^{13} and 2×10^{14} molecules cm^{-3}) from Figure 40,

a plot of the pseudo-first order rate constant k' as a function of [CH_3OH] (Figure 41) returns a rate constant of $k_{CH3OH+OH}$ = (7.8 ± 0.5) × 10^{-13} $cm^3molecule^{-1}s^{-1}$ at 293 K, in good agreement with the value from (Meier et al., 1984): $k_{CH3OH+OH}$ = (7.7 ± 1.0) × 10^{-13} $cm^3molecule^{-1}s^{-1}$ at 300 K and the IUPAC recommendation (Atkinson et al., 2006a): $k_{CH3OH+OH}$ = 9.0 × 10^{-13} $cm^3molecule^{-1}s^{-1}$.

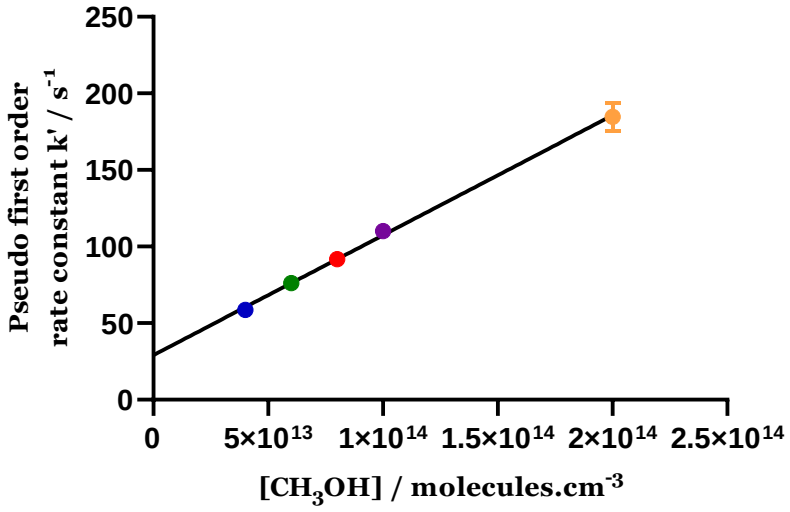

Figure 41: Pseudo-first order rate constant k' as a function of [CH_3OH] (0 - 2 × 10^{14} molecules cm^{-3})

Then, the same experiment was performed at a lower concentration of F: [F] = 8×10^{11} molecules cm^{-3} and [CH_3OH] = 0 - 4 × 10^{14} molecules cm^{-3}. Using these concentrations shows a linear OH decay over the entire reaction time range for [CH_3OH] < 2 × 10^{14} molecules cm^{-3} and a rate constant $k_{CH3OH+OH}$ = (6.03 ± 1.07) × 10^{-13} $cm^3molecule^{-1}s^{-1}$ that is in agreement with the value in the literature.

To resume the effect of NO_2 addition on C_3H_8 + OH and CH_3OH + OH reactions, a linear OH decay is obtained for higher concentrations of propane and methanol than without adding NO_2 where the non-linearity problem appears for concentrations of propane and methanol greater than 8 × 10^{13} molecules cm^{-3}. Thus, adding NO_2 improves the results on the kinetics of the reaction between propane/methanol and OH. However, the problem does not seem to be completely solved because the non-linearity of OH decay is still observed for higher concentration of the stable molecule.

3.4.2.3. $CH_3OH + OH + O_2$ reaction

As shown before in the previous work (Kravtchenko, thesis 2019), the addition of O_2 (in excess) to the CH_3OH + OH reaction leads to the formation of HO_2 radicals, through the following sequence:

$CH_3OH + OH \rightarrow CH_2OH + H_2O$	(R 39)	$k_{39}/ (k_{39} + k_{40}) = 0.85 \pm 0.08$ (McCaulley et al., 1989)
$CH_3O + H_2O$	(R 40)	$k_{40}/ (k_{39} + k_{40}) = 0.15 \pm 0.08$
$CH_2OH + O_2 \rightarrow HO_2 + CH_2O$	(R 41)	$k = 9.69 \times 10^{-12}$ $cm^3molecule^{-1}s^{-1}$ (Atkinson et al., 2006a)
$CH_3O + O_2 \rightarrow HO_2 + CH_2O$	(R 42)	$k = 1.9 \times 10^{-15}$ $cm^3molecule^{-1}s^{-1}$ (Atkinson et al., 2006a)

Then HO_2 radical formation can be measured by cw-CRDS and compared to the decay of OH.

Figure 42 shows the OH decay and HO_2 formation as a function of reaction time during the reaction of CH_3OH + OH in the presence of O_2 and in the presence of $NO_2 + O_2$ for [F] = 5×10^{12} molecules cm^{-3}, [H_2O] = 2×10^{14} molecules cm^{-3}, [CH_3OH] =1×10^{14} molecules cm^{-3}, [O_2] = 1×10^{15} molecules cm^{-3} and [NO_2] = 0 or 4×10^{13} molecules cm^{-3}.

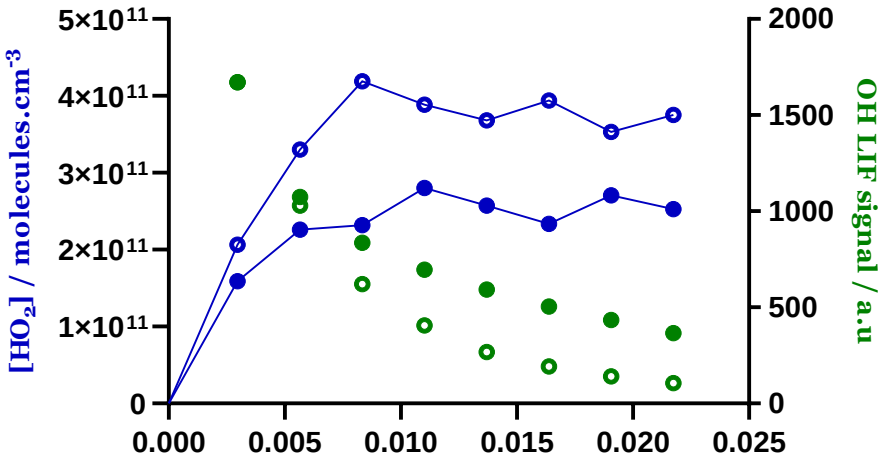

Figure 42: HO_2 concentration (blue symbols) and OH LIF signal (green symbols) as a function of reaction time with [NO_2] = 4×10^{13} molecules cm^{-3} (open symbols) and [NO_2] = 0 (filled symbols)

The results show that there is more consumption of OH at high reaction time when NO_2 is added (green open symbols) than without adding NO_2 (green filled symbols). The concentration of HO_2 formed without adding NO_2 (blue filled symbols) is about 2.5×10^{11} molecules cm^{-3} that is lower than expected (~ 8×10^{11} molecules cm^{-3} according to simulation). The addition of NO_2 (blue open symbols) show a slight increase in the concentration of HO_2 formed, $[HO_2] = 4 \times 10^{11}$ molecules cm^{-3} (blue filled symbols), but it is still lower than expected.

In an attempt to understand this low concentration of HO_2 radicals, several tests were carried out by measuring HO_2 radicals using the cw-CRDS formed from the reaction of $CH_3OH + F + O_2$ and $CH_3OH + Cl + O_2$. Several configurations were tried, however, it was not possible to obtain the expected concentration of HO_2.

3.5. Re-formation of OH from the formation of helium cations?

Another possible explanation for the OH re-formation phenomenon could come from the formation of helium cations in the microwave discharge that react with water to reform OH, $He^+ + H_2O \rightarrow$ OH (or $He^+ + C_3H_8$ or CH_3OH) (Ridenti et al., 2015). This hypothesis was checked by replacing helium in the discharge by argon and by performing different tests without adding fluorine to check if we can see a formation of OH radical.

3.5.1. Replacement of helium in the discharge by argon

To check if the OH re-formation phenomenon is due to the formation of helium cations in the discharge, the first test was to replace the helium by argon and study the reaction of OH with C_3H_8/CH_3OH under the same conditions as before.

The CH_3OH + OH reaction was studied by creating OH in the double injector from the reaction F + H_2O with $[F] = 8 \times 10^{11}$ molecules cm^{-3} and $[H_2O] = 2 \times 10^{14}$ molecules cm^{-3}. Methanol was introduced into the reactor with $[CH_3OH] = 1.2 \times 10^{14}$ molecules cm^{-3}. A comparison for the OH fluorescence signal as a function of time between using the He and Ar in the discharge is presented in Figure 43.

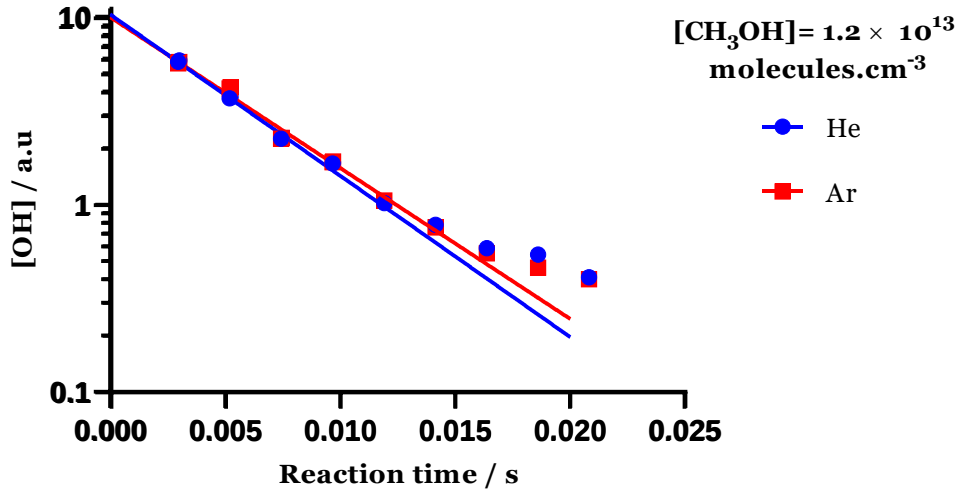

Figure 43: Comparison of the OH fluorescence signal (logarithmic scale) for using the He or Ar in the discharge as a function of reaction time for [F] = 8×10^{11} molecules cm^{-3} and [CH_3OH] = 1.2×10^{14} molecules cm^{-3}

The results show that the non-linearity phenomenon still appears even by using argon as a carrier gas in the discharge instead of helium. Performing the same experiment for C_3H_8 + OH showed also a non-linear decay for the OH radicals.

3.5.2. Tests without fluorine

The other tests performed to check if the OH radicals are reformed from the helium cations was to do experiments without adding fluorine. Several tests were done by introducing into the reactor: only He, He + H_2O, He + C_3H_8, He + H_2O + C_3H_8, He + CH_3OH, He + H_2O + CH_3OH to check if there will be formation of OH without adding fluorine. The results showed that in all cases there was no formation of OH radicals.

To conclude, all the attempts did not solve the OH re-formation phenomenon when OH was generated from F + H_2O. As shown before in the previous work (Kravtchenko, thesis 2019), it was possible to avoid the problem of non-linearity by generating OH from H + NO_2. However, as mentioned before, the method of generation of OH from H + NO_2 reaction was not our first choice in this project since the final purpose is to study reactions between RO_2 and HOx in low NOx conditions, a NOx free source of OH is thus needed. Then, C_3H_8 + OH and CH_3OH + OH reactions were studied by generating OH from H + NO_2 → OH + NO to check if there will be a linear OH decay as before.

3.6. Generation of OH from H + NO_2

3.6.1. Measurement of the dissociation rate of H_2

The dissociation rate of H_2 was estimated by monitoring the signal at mass 46 which corresponds to NO_2 using mass spectrometry. The signal for mass 46 was measured with and without discharge where the difference between the two signals corresponds to the consumption of NO_2 by H. Thus, the fraction of NO_2 consumed corresponds to the concentration of H. The dissociation rate for H_2 was about 43 ± 5 % and it was measured for different concentrations of. H_2. This value was higher than that mentioned in the literature where the dissociation rate is about 20 % (Raventos-Duran et al., 2007a).

3.6.2. Effect of NO_2 and H concentrations on the formation of OH radicals

OH radicals were generated from the reaction H + NO_2 → OH + NO in the single injector configuration. The evolution of the OH signal was first monitored as a function of the concentration of NO_2 and H. Figure 44 represents the experimental OH fluorescence signal as a function of the NO_2 concentration with [H] = 5×10^{11} molecules cm^{-3}.

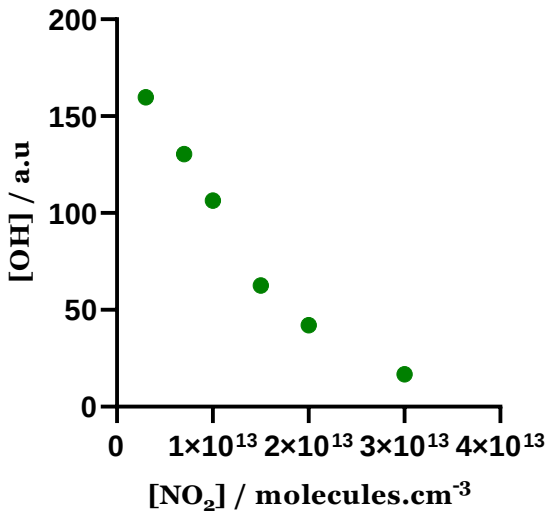

Figure 44: OH fluorescence signal as a function of [NO_2] for [H] = 5×10^{11} molecules cm^{-3}

In this case, when the concentration of NO_2 increases, the OH signal decreases. This decrease is due to the competition between H + NO_2 and the reaction between NO_2 and OH (R 43) which consumes the formed OH radicals.

The concentration of NO_2 must be in excess to rapidly consume all hydrogen atoms, but not in large excess to avoid the consumption of the OH radicals formed through reaction (R 43). Therefore, the concentration of NO_2 was set to be about 1×10^{13} molecules cm^{-3} when using this method of OH generation to limit the influence of the competitive reaction (R 43).

Figure 45 represents the evolution of the OH fluorescence signal as a function of the concentration of hydrogen atoms with $[NO_2] = 1 \times 10^{13}$ molecules cm^{-3}.

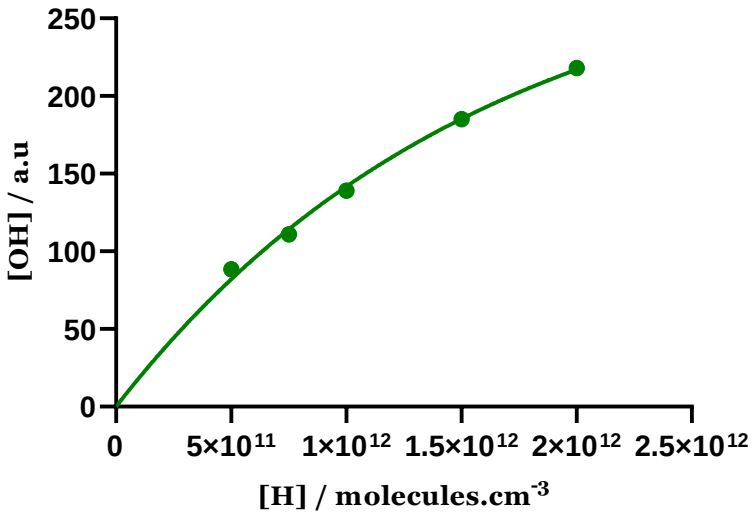

Figure 45: OH fluorescence signal as a function of [H] for $[NO_2] = 1 \times 10^{13}$ molecules cm^{-3}

The OH signal shows an increase with the concentration of H atoms, showing that the concentration of NO_2 is sufficient to convert the H atoms into OH radicals. These results are similar to those obtained in the previous work (Kravtchenko, thesis 2019).

3.6.3. C_3H_8 + OH reaction

The C_3H_8 + OH reaction was studied by creating OH in the single injector from the reaction H + NO_2 with $[H] = 5 \times 10^{11}$ molecules cm^{-3} and $[NO_2] = 1 \times 10^{13}$ molecules cm^{-3}. Propane was introduced into the stainless steel reactor with $[C_3H_8] = 0 - 4 \times 10^{14}$ molecules cm^{-3}. Figure 46 represents the OH fluorescence signal (logarithmic scale) as a function of reaction time for different concentrations of C_3H_8.

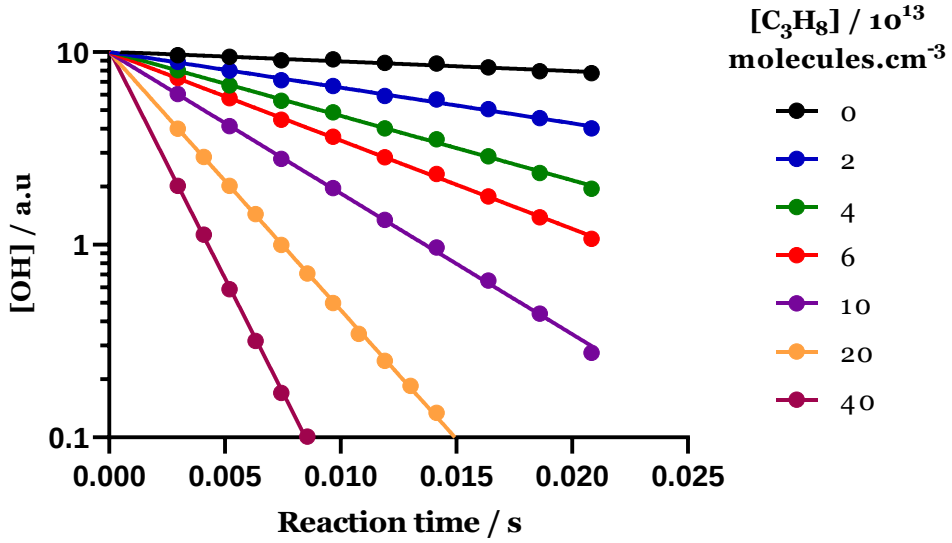

Figure 46: OH fluorescence signal (logarithmic scale) as a function of reaction time for [H] = 5×10^{11} molecules cm^{-3}, [NO_2] = 1×10^{13} molecules cm^{-3}, and [C_3H_8] =0 - 4×10^{14} molecules cm^{-3}

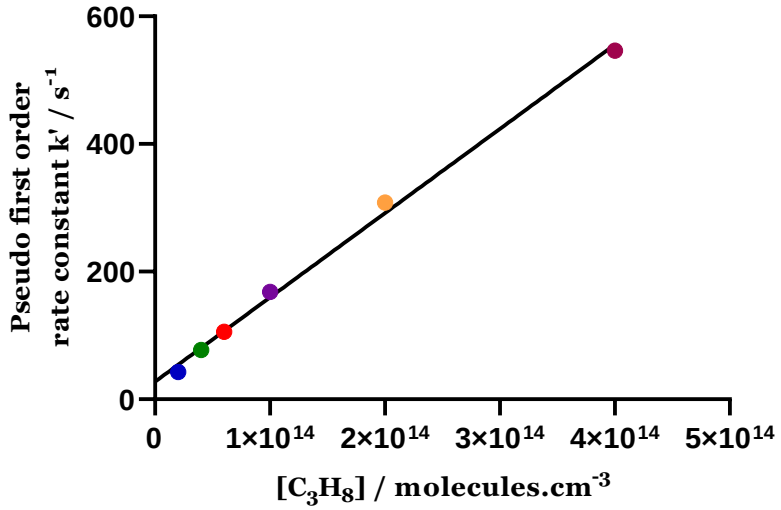

Figure 47: Pseudo-first order rate constant k' as a function of [C_3H_8] (0 - 4×10^{14} molecules cm^{-3})

The OH decay is linear over the entire time range and for all concentrations of propane (even for high concentration of propane: 4×10^{14} molecules cm^{-3}). The consumption of OH is close to 100% for the highest concentrations, 2×10^{14} molecules cm^{-3} and 4×10^{14} molecules cm^{-3} at 15 ms and 9 ms respectively. Moreover, the rate constant determined from these results, $k_{C3H8+OH}$ = (1.34 ± 0.09) $\times 10^{-12}$ $cm^3 molecule^{-1} s^{-1}$, is in a good agreement with data from the literature.

These results show that the non-linearity phenomenon does not appear for C_3H_8 + OH reaction when OH is generated from H + NO_2. Performing the same experiments using the glass reactor instead of the stainless steel reactor showed also the same results. Then, CH_3OH + OH reaction was studied to ensure the absence of the non-linearity phenomenon using this method.

3.6.4. CH_3OH + OH reaction

The CH_3OH + OH reaction was studied by creating OH in the single injector from the reaction H + NO_2 with [H] = 5×10^{11} molecules cm^{-3} and [NO_2] = 1×10^{13} molecules cm^{-3}. Methanol was introduced into the stainless steel reactor with [CH_3OH] = 0 - 3×10^{14} molecules cm^{-3}. Figure 48 represents the OH fluorescence signal (logarithmic scale) as a function of reaction time for different concentrations of CH_3OH.

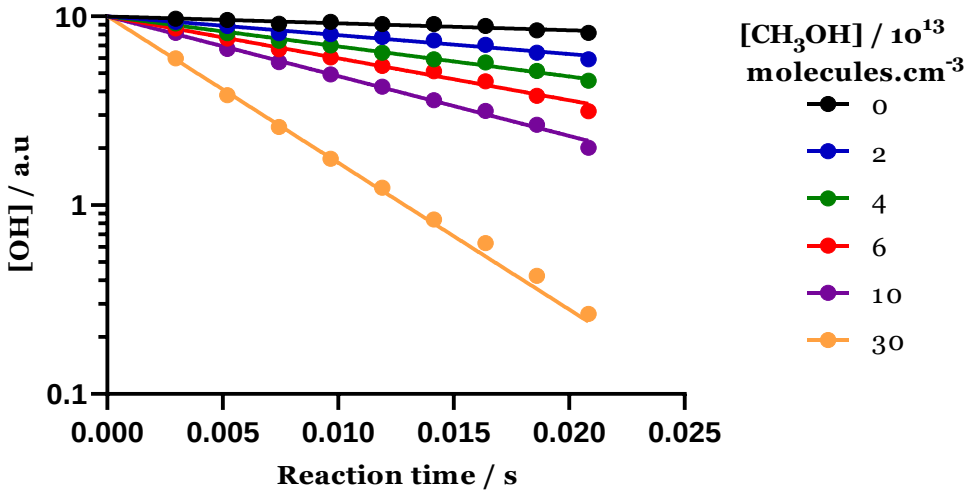

Figure 48: OH fluorescence signal (logarithmic scale) as a function of reaction time for [H] = 5×10^{11} molecules cm^{-3}, [NO_2] = 1×10^{13} molecules cm^{-3}, and [CH_3OH] =0 - 30×10^{13} molecules cm^{-3}

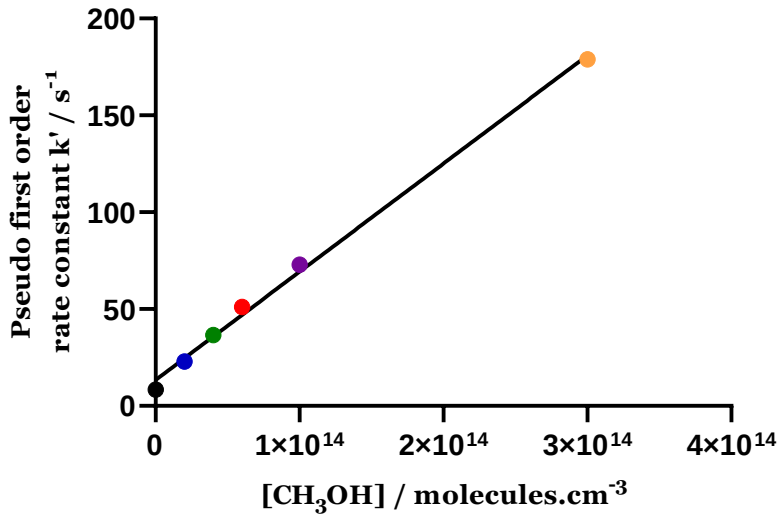

Figure 49: Pseudo-first order rate constant k' as a function of $[CH_3OH]$ (0 - 3×10^{14} molecules cm^{-3})

The OH decay is linear over the entire reaction time range and for all the concentrations of methanol. However, the obtained rate constant $k_{CH3OH+OH} = (5.6 \pm 0.5) \times 10^{-13}$ $cm^3 molecule^{-1} s^{-1}$ (Figure 49) is lower than the value from (Meier et al., 1984): $k_{CH3OH+OH} = (7.7 \pm 1.0) \times 10^{-13}$ $cm^3 molecule^{-1} s^{-1}$ at 300 K and close to the value obtained by generating OH from F + H_2O $k_{CH3OH+OH} = (5.9 \pm 0.6) \times 10^{-13}$ $cm^3 molecule^{-1} s^{-1}$ (for the linear part of the curve). Removing the last two points of the curve for $[CH_3OH]$ = 1 and 3×10^{14} molecules cm^{-3}, the rate constant becomes 7.0×10^{-13} $cm^3 molecule^{-1} s^{-1}$ that is closer to the value in the literature. Furthermore, the value of the first order rate constant for OH wall loss, determined experimentally without adding CH_3OH: $k_{wall} = 8.5$ s^{-1} (Figure 48) is not in agreement with the extrapolation to $[CH_3OH] = 0$ in Figure 49 where $k_{wall} = 13.5$ s^{-1}. Thus a linear decay is obtained when OH is generated from H + NO_2, but the value of the rate constant obtained is slightly lower than the value in the literature. Performing the same experiments using the glass reactor instead of the stainless steel reactor showed also the same results.

3.7. Conclusion

This chapter presents a summary of the previous work done using the recently developed fast flow reactor where an OH re-formation phenomenon was disturbing the kinetic measurements of the rate constants of well-known reactions between OH radicals and stable species (propane, ethane, methanol). Following this work, different hypotheses were then explored during my PhD in order to explain the OH re-formation phenomenon. Various tests showed that the problem is not due to

heterogeneous reactions on the walls of the internal injector or the reactor. It is also not due to the formation of F atoms in the external injector, neither to the formation of O atoms, nor to the formation of helium cations in the microwave discharge. This problem was not observed when OH was generated by the reaction of H + NO_2 which is the method mostly used in the literature. However, this method of OH generation was not our first choice in this project since the final purpose is to study reactions between RO_2 and HOx in low NOx conditions. All attempts to avoid the OH re-formation phenomenon were unsuccessful so far.

The kinetic and spectroscopic study of the ethyl peroxy radical studied using the laser photolysis cell coupled to a double cw-CRDS paths will be described in the following chapter.

Chapter 4: Kinetic and Spectroscopic Study of Ethyl Peroxy Radical

4.1. Introduction

Ethane is one of the most abundant non-methane hydrocarbons in the atmosphere where its oxidation leads to the formation of the ethyl peroxy radical, $C_2H_5O_2$. Under low NO_x conditions, the $C_2H_5O_2$ radical can undergo several reactions, either with itself as self-reaction, or with HO_2, or with other peroxy radicals mainly CH_3O_2, or with OH radicals.

As mentioned in Chapter 1 (section 1.1.3.3.), the $C_2H_5O_2$ self-reaction has several product pathways that either lead to stable products (R 29b and (R 29c, where (R 29c is thought to be minor) or maintain the radical pool through formation of HO_2 radicals ((R 29a) followed by (R 30) in the presence of O_2):

$$C_2H_5O_2 + C_2H_5O_2 \rightarrow C_2H_5O + C_2H_5O + O_2 \quad \text{(R 29a)}$$

$$C_2H_5O_2 + C_2H_5O_2 \rightarrow C_2H_5OH + CH_3CHO + O_2 \quad \text{(R 29b)}$$

$$C_2H_5O_2 + C_2H_5O_2 \rightarrow C_2H_5O_2C_2H_5 + O_2 \quad \text{(R 29c)}$$

$$C_2H_5O + O_2 \rightarrow CH_3CHO + HO_2 \quad \text{(R 30)}$$

$$C_2H_5O_2 + HO_2 \rightarrow C_2H_5OOH + O_2 \quad \text{(R 20a)}$$

$$C_2H_5O_2 + C_2H_5O \rightarrow \text{products} \quad \text{(R 44)}$$

When studying the $C_2H_5O_2$ self-reaction, several secondary reactions can be important and should be taken into account: the reaction of $C_2H_5O_2$ with HO_2 (R 20a) where HO_2 is formed through reaction (R 30) and the reaction of $C_2H_5O_2$ with C_2H_5O (R 44). The rate constant of (R 20a) (~10^{-12} $cm^3molecule^{-1}s^{-1}$) is higher than that of (R 29a) (~10^{-14} $cm^3molecule^{-1}s^{-1}$) and this accelerates the $C_2H_5O_2$ decays thus complicating the investigation of the $C_2H_5O_2$ self-reaction. As a result, measuring the rate constant k_{29} from the observed $C_2H_5O_2$ decays depends on the branching ratio $r' = k_{29a} / k_{29}$ used in the data treatment.

It was agreed in almost all earlier studies using the time resolved UV absorption spectroscopy method for the determination of the rate constant and using the FTIR or gas chromatography for the determination of the branching ratio that the $C_2H_5O_2$ self-reaction lead mainly to the formation of ethoxy radical C_2H_5O by pathway (R 29a, with a branching ratio of $r' = k_{29a} / k_{29} = 0.63$) and a total rate constant of $k_{29} = 7.6\times10^{-14}$ $cm^3molecule^{-1}s^{-1}$ is currently recommended by the IUPAC committee (Atkinson et al., 2006a). However, a recent work (Noell et al., 2010) using a more selective method to study the $C_2H_5O_2$ self-reaction obtained a large disagreement with the earlier recommendations. The UV absorption was used for $C_2H_5O_2$ detection and the near-infrared (NIR) absorption was used for direct measurement of HO_2. The results showed that the radical path was not the major path with a branching ratio of $r' = k_{29a} / k_{29} = 0.28$ and a higher total rate constant of $k_{29} = 1.19\times10^{-13}$ $cm^3molecule^{-1}s^{-1}$ than the value recommended by the IUPAC. Therefore, it seems important to reinvestigate this reaction with another selective detection method.

In this chapter, the kinetics of the $C_2H_5O_2$ self-reaction was investigated using the laser photolysis cell coupled to a double cw-CRDS paths (see Chapter 2) where $C_2H_5O_2$ and HO_2 were determined independently in the near IR region. The $C_2H_5O_2$ radical was detected in the $\tilde{A}$-$\tilde{X}$ electronic transition at 7596.47 cm^{-1} (1316.4 nm), and the HO_2 radical was quantified in the $2\nu_1$ overtone vibration band at 6638.2 cm^{-1} (1506.4 nm). The absorption cross-section of the ethyl peroxy radical was first determined by two different approaches. In the first method, the $C_2H_5O_2$ absorption cross-section was determined in back-to-back experiments relative to the absorption cross-section of HO_2 and then it was validated by measuring the rate constant of the cross reaction between $C_2H_5O_2$ and HO_2. Then, the rate constant and branching ratio of the ethyl peroxy self-reaction was determined.

4.2. Generation of radicals

Ethyl peroxy radicals were generated by the photolysis of C_2H_6/ Cl_2/ O_2 mixtures at 351 nm:

$$Cl_2 + h\upsilon_{351\ nm} \rightarrow 2\ Cl \qquad \text{(R 45)}$$

$$C_2H_6 + Cl \rightarrow C_2H_5 + HCl \qquad \text{(R 46)}$$

$$C_2H_5 + O_2 + M \rightarrow C_2H_5O_2 + M \qquad \text{(R 47a)}$$

$$C_2H_5 + O_2 \rightarrow C_2H_4 + HO_2 \qquad \text{(R 47b)}$$

HO_2 radicals were generated by the addition of methanol, CH_3OH, in varying concentrations to the mixture:

$$CH_3OH + Cl \rightarrow CH_2OH + HCl \quad \text{(R 48)}$$

$$CH_2OH + O_2 \rightarrow CH_2O + HO_2 \quad \text{(R 41)}$$

Most experiments were carried out at 100 Torr O_2 (Air Liquide, Alphagaz 2) in order to rapidly convert C_2H_5O into HO_2 through (R 30). The Cl_2 concentration was around 1×10^{16} molecules.cm^{-3}, leading to initial Cl-atom concentrations of around 1×10^{14} molecules.cm^{-3} with a photolysis energy of 20 mJ/cm^2. Some experiments were carried out at 90 Torr N_2 / 10 Torr O_2 in order to investigate the possible secondary reaction (R 44) as will be explained later.

The flow of the various gases was added directly from the cylinder (ethane (Mitry-Mory, N35), chlorine (Praxair), oxygen (Air Liquide)) and controlled by a calibrated flow meter (Bronkhorst, Tylan). Methanol (Sigma-Aldrich) was added to the mixture by passing a small fraction of the main flow through a bubbler containing liquid methanol, kept in a thermostated water bath. All experiments were carried out at 298 K.

The various gases introduced into the reactor and the injector are controlled by mass flow regulators (Tylan or Bronkhorst) previously calibrated.

4.3. Spectroscopic study of $C_2H_5O_2$ radicals

A reliable detection of the $C_2H_5O_2$ radical is highly desirable for studying its reactivity. Most of the previous studies of peroxy chemistry have been carried out by UV absorption spectroscopy, however, the absorption of peroxy radicals in the near IR region allows a more selective detection. The electronic transitions of peroxy radicals in the near IR region have not attracted much attention after they have been located for the first time by Hunziker and Wendt in 1976 (Hunziker & Wendt, 1974, 1976) due to their small absorption cross-sections (~10^{-20} – 10^{-21} cm^2). Interest has been revived many years later when the CRDS technique has been developed (O'Keefe & Deacon, 1988; Romanini et al., 1997).

The first report on using the CRDS technique for the detection of peroxy radicals was in 2000 (Pushkarsky et al., 2000). T.A.Miller and coworkers measured the absorption spectra of the methyl and ethyl peroxy radicals, but determined only the absorption cross section for the methyl peroxy radical. They found a peak of the $\tilde{A}$-$\tilde{X}$ transition for $C_2H_5O_2$ around 7596 cm^{-1}.

A few years later, the spectra of both radicals, CH_3O_2 and $C_2H_5O_2$, was measured again by Atkinson and Spillman (Atkinson & Spillman, 2002) using a continuous external cavity diode laser to perform cw-CRDS with a much narrower bandwidth (~3×10^{-5} cm^{-1}). They confirmed the overall shape of the previous absorption spectrum, and measured for the first time the absorption cross-section for $C_2H_5O_2$ using the kinetic method (Farago et al., 2013; Thiebaud et al., 2007; Wen et al., 2019, 2020). This method can be used if the rate constant of a radical-radical reaction is known, because the initial concentration and thus the absorption cross-section can in principle be determined from the shape of the kinetic decay. The self-reaction can be described as follows.

$$A + A \rightarrow B$$

$$\frac{d[A]}{dt} = -2k[A]^2 \qquad \text{Equation 38}$$

Integration of Equation 38 leads to

$$\frac{1}{[A]} = \frac{1}{[A]_0} + 2kt \qquad \text{Equation 39}$$

Hence, plotting 1/[A] as a function of time leads to a straight line with the slope being *2k*. The absorption coefficient $\alpha = \sigma \times [A]$ (where α is the absorption coefficient and σ is the absorption cross-section of the species studied) can be used in Equation 39 instead of [A] when the rate constant is known, but not the absolute concentration of A, this leads to

$$\frac{1}{\sigma \times [A]} = \frac{1}{\sigma \times [A]_0} + \frac{2k}{\sigma} t \qquad \text{Equation 40}$$

Plotting $1/\sigma \times [A]$ as a function of time leads to a straight line with the slope being $m = 2k/\sigma$ while the intercept $I = 1/\sigma \times [A]_0$. However, different complications can arise from this method where the radicals can be lost through other processes too, for example through diffusion out of the photolysed volume or through unidentified secondary reactions. Due to these complications, the decays are faster than expected from pure self-reaction only, and the retrieved absorption cross-section would be too small. This method has another complication in the case of the self-reaction

of peroxy radicals (R 29) since one of its product pathways leads to the formation of HO_2 radicals (R 30) that accelerates the $C_2H_5O_2$ decays. By applying the kinetic method using the recommended value of k_{29obs}, Atkinson and Spillman (Atkinson & Spillman, 2002) obtained an absorption cross-section for $C_2H_5O_2$ at 7596 cm^{-1} of $\sigma = (3.0 \pm 1.5) \times 10^{-21}$ cm^2.

Another work on the ethyl peroxy spectrum was done by the Miller group (Rupper et al., 2007) where they scanned the $\tilde{A} \leftarrow \tilde{X}$ electronic transition over a large wavelength range and identified the transitions for the two different isomers. Ethyl peroxy radicals exist in an equilibrium between two stable conformers, T (trans) and G (gauche) conformer. The dihedral angles between the O-O-C and O-C-C planes being 0° for the T- and 120° for the G-conformer. The peak absorptions for the T and G conformers of $C_2H_5O_2$ radical were located at 7362 cm^{-1} and 7592 cm^{-1}, respectively. In this work, the absorption cross-section was estimated using a different method where the $C_2H_5O_2$ radicals were generated by the reaction of Cl-atoms with C_2H_6, with the Cl-atoms being generated by 193 nm photolysis of oxalylchloride, $(COCl)_2$. To obtain the concentration of $C_2H_5O_2$, they calculated the Cl-atom concentration from the difference between the photolysis laser energy with and without precursor, and supposing that each Cl-atom generated one $C_2H_5O_2$ radical, they obtained $\sigma = 4.4 \times 10^{-21}$ cm^2 for $C_2H_5O_2$ at 7596 cm^{-1}.

The next work on the ethyl peroxy spectrum done by the Miller group (Melnik et al., 2010) used a different method to determine the absorption cross-section. They used a dual-path CRDS set-up where the concentration of HCl (generated from the reaction of Cl-atoms with C_2H_6) was measured on one path while the absorption of $C_2H_5O_2$ was measured simultaneously on the other path. Again, they supposed that each HCl-molecule had generated one $C_2H_5O_2$ radical and thus obtained $\sigma = (5.29 \pm 0.20) \times 10^{-21}$ cm^2 for $C_2H_5O_2$ at 7596 cm^{-1}.

In the most recent work from the Miller group (Melnik & Miller, 2013), the above absorption cross-section was validated indirectly by applying the kinetic method: the $C_2H_5O_2$ absorption profiles were converted to $C_2H_5O_2$ concentration-time profiles using the absorption cross-section obtained previously, and the rate constant k_{29obs} for the self-reaction was extracted. The obtained value of k_{29obs} was consistent with the majority of the previously reported values, which was taken as an indication that the absorption cross-section is valid.

In this work, a new determination of the absorption cross-section for the $C_2H_5O_2$, based on two different approaches, will be presented (sections 4.3.2 and 4.3.3). The first approach is comparable to one of the Miller methods (Melnik et al., 2010) and will be called “back-to-back” method: in our

dual-path CRDS set-up we generate Cl-atoms and convert them to HO_2 through reaction with CH_3OH, with HO_2 being quantified on one path at 6638.2 cm^{-1}. Directly after, the Cl-atoms were converted to $C_2H_5O_2$ by adding C_2H_6 instead of CH_3OH to the reaction mixture, with $C_2H_5O_2$ absorption being measured on the second path. Supposing that the Cl concentration stays the same between both experiments and that in both cases all Cl-atoms are transformed to either HO_2 (which can be quantified reliably) or to $C_2H_5O_2$, the absorption cross-section of $C_2H_5O_2$ is determined relative to that of HO_2. The second approach is a kinetic method such as used by Atkinson and Spillman (Atkinson & Spillman, 2002) and Melnik et al. (Melnik & Miller, 2013), but not based on the self-reaction of $C_2H_5O_2$, but on the cross reaction between HO_2 and $C_2H_5O_2$. This reaction has been studied in a wide range of concentrations under either excess of HO_2 or excess of $C_2H_5O_2$. In the first case, using excess of HO_2, the rate constant is retrieved by adjusting the $C_2H_5O_2$ decays with the absolute concentration of HO_2 being fixed. In the second case, using excess of $C_2H_5O_2$, the rate constant is fixed to the value determined just before, and now the best fit of the HO_2 decay is achieved by adjusting the absolute concentration of $C_2H_5O_2$, i.e., the absorption cross-section.

A summary of previous results as well as the results obtained in this work is presented in Table 3.

Table 3: Summary of the $C_2H_5O_2$ absorption cross-section at 7596 cm^{-1}.

$\sigma/10^{-21}$ cm^2	Method	Reference
3.0 ± 1.5	Kinetic method, no other radical losses considered	Atkinson & Spillman, 2002
4.4	Depletion of photolysis energy through precursor with [Cl] = [$C_2H_5O_2$], i.e., no secondary reactions considered	Rupper et al., 2007
5.29 ± 0.20	Measurement of HCl in dual path CRDS with [Cl] = [$C_2H_5O_2$], i.e., no secondary reactions considered	Melnik et al., 2010
5.29	Kinetic method used for validation of Melnik et al., 2010	Melnik & Miller, 2013
10 ± 2	Measurement of HO_2/$C_2H_5O_2$ in dual path CRDS with [Cl] = [HO_2] = [$C_2H_5O_2$]	This work
10 ± 2	Kinetic method from $C_2H_5O_2$ + HO_2	This work

4.3.1. Detection of HO_2 and $C_2H_5O_2$

The reliability of the measurements depends on the selective quantification of the two radicals, HO_2 and $C_2H_5O_2$.

Detection of HO_2 radicals

The HO_2 radical has been detected in the $2\nu_1$ overtone vibration band at 6638.2 cm^{-1}. The HO_2 absorption spectrum in this wavelength range is very structured with sharp peaks, thus it is easy to verify the selectivity of the detection of HO_2 by taking absorption measurements on top of the line, and at a wavelength just next to it, where the absorption of HO_2 is virtually zero. The results showed that there was no absorption signal observed off the HO_2 line in any of the current experiments, and therefore we can conclude that absorption measurements at 6638.2 cm^{-1} are highly selective for HO_2 in this reaction system.

Detection of $C_2H_5O_2$ radicals

The $C_2H_5O_2$ radical has been detected in the $\tilde{A}$-$\tilde{X}$ electronic transition at 7596.47 cm^{-1}. To ensure that the decays measured at the peak wavelength of $C_2H_5O_2$ are selective for this radical, it is not possible to measure, as for HO_2, decays at a wavelength where $C_2H_5O_2$ does not absorb, since the transition is too broad. Therefore, the decays have been measured at several different wavelengths that are accessible with our DFB laser: in the case of an underlying absorption of another species, for example a reaction product, one can expect that the shape of the absorption spectrum for any other species would be different from the shape of the $C_2H_5O_2$ spectrum. An underlying absorption of another species with a less or differently varying spectrum should lead to different shapes of decays at different wavelengths. Figure 50 show examples of decays obtained at five different wavelengths, all measured under the same conditions following the 351 nm photolysis of Cl_2 / C_2H_6 mixtures. A very high initial radical concentration has deliberately been used in order to force the formation of high concentrations of reaction products. Even when using these conditions, no change in the shape of the decays can be observed for the different wavelengths, and therefore we conclude that measurements at 7596.47 cm^{-1} are selective for $C_2H_5O_2$ in this reaction system.

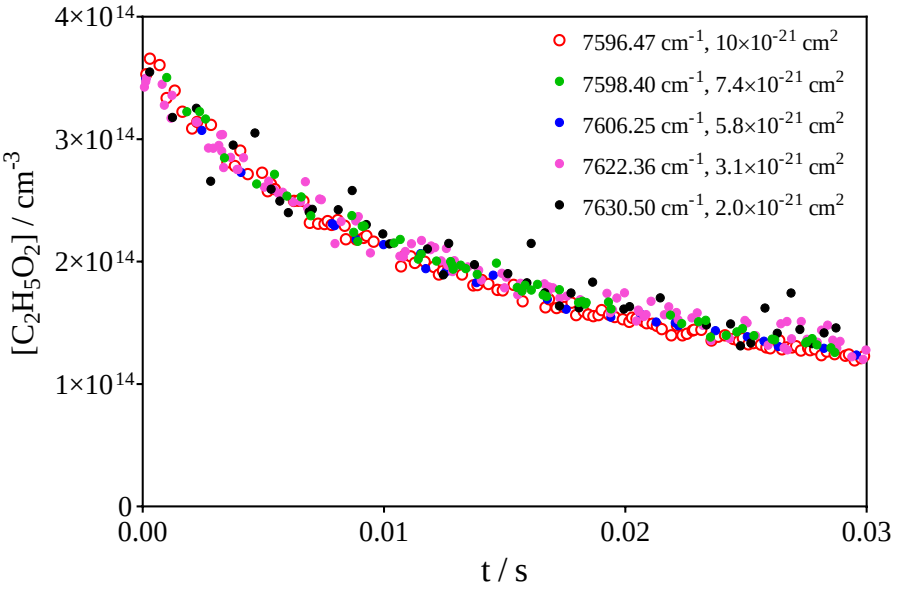

Figure 50: Examples of $C_2H_5O_2$ decays following the 351 nm photolysis of $[Cl_2] = 3\times10^{16}$ cm^{-3} in presence of $[C_2H_6] = 2.6\times10^{16}$ cm^{-3}, obtained at 5 different wavelengths: the absorption cross section of $C_2H_5O_2$ (given in the legend of the figure) varies over a factor of 5 for the different wavelengths

4.3.2. Quantification of $C_2H_5O_2$ in Back-to-Back Experiments

In the first method, the $C_2H_5O_2$ absorption cross-section was determined in a rather direct way in back-to-back experiments relative to the absorption cross-section of HO_2. Therefore, the reliability of the measurement of the absorption cross-section of $C_2H_5O_2$ depends on the reliability of the absorption cross-section of HO_2. There have been several measurements on the cross-sections of HO_2 and absorption spectrum in the near IR (Assaf et al., 2017a; DeSain et al., 2003; Tang et al., 2010; Thiebaud et al., 2007) and also on the pressure broadening of selected lines (Assaf et al., 2018c; Ibrahim et al., 2007; Onel et al., 2017). In this work, HO_2 was detected on two different absorption lines with the cross-section varying about a factor of 9 between both lines. In most of the experiments HO_2 was detected on the strongest line of the $2\nu_1$ band at 6638.2 cm^{-1}, but for experiments with high initial HO_2 concentrations a small line at 6638.58 cm^{-1} has been used to avoid saturation. The absorption cross-section of the strongest line in helium ($\sigma_{50\ \text{Torr He}} = 2.72 \times 10^{-19}$ cm^2) (Tang et al., 2010; Thiebaud et al., 2007) and in synthetic air (Assaf et al., 2018c; Ibrahim et al., 2007; Onel et al., 2017) ($\sigma_{100\ \text{Torr air}} = 1.44 \times 10^{-19}$ cm^2) has been carried out several times. The cross-section of the small line has only been determined once in 50 and 100 Torr helium (2.8 and 2.1 × 10^{-20} cm^2, respectively) (Assali et al., 2019; Onel et al., 2017), but no measurements

in pure O_2 have been carried out. Therefore, we have determined both cross-sections (for HO_2 and $C_2H_5O_2$) in 100 Torr O_2 in this work, using the kinetic method.

Figure 51 shows the measurement of HO_2 absorption cross section where HO_2 decays have been measured for 3 different initial Cl-atom concentrations and the raw signals are shown in graph 51(a). The decays have then been plotted following Equation 40 and the result is shown in graph 51(b). Using the known rate constant of the HO_2 self-reaction ($k_{HO2} + k_{HO2} = 1.7 \times 10^{-12}$ $cm^3molecule^{-1}s^{-1}$), the slope of a linear regression of the plot in graph 51(b) can in principle be converted to the absorption cross-section. However, as has been mentioned above, radicals can be lost through other processes, and in the case of laser photolysis experiments one possible loss is through diffusion out of the photolysis volume. The influence of this loss process decreases with increasing initial HO_2 concentration. In order to correct this influence, an extrapolation to infinite $[HO_2]_0$ is used and the result is presented in graph 51(c) where the slope m from graph 51(b) is plotted as a function of the intercept I ($=1/\alpha_0$). Extrapolating the m-values to I = 0 therefore removes the impact of the diffusion on the slope m. Using the slope m determined from the extrapolation instead of using the directly obtained slope m leads to an increase in the absorption cross-section of 6% for the highest initial concentration and 13% for the lowest initial concentration. In graph 51(c), error bars correspond to 95% confidence interval of the linear regression from the graph 51(b): the error bars on the x-values are too small to be seen within the symbols. Other several series have been measured for both absorption lines, and the following absorption cross-sections in 100 Torr O_2 have been obtained for HO_2 for the two lines:

$$6638.2\ cm^{-1} : \sigma_{HO2} = (2.0 \pm 0.3) \times 10^{-19}\ cm^2.$$

$$6638.58\ cm^{-1} : \sigma_{HO2} = (2.1 \pm 0.3) \times 10^{-20}\ cm^2.$$

The uncertainty on σ_{HO2} reflects the uncertainty of ±15% on the rate constant of the self-reaction of HO_2, such as estimated by the IUPAC committee (Atkinson et al., 2004).

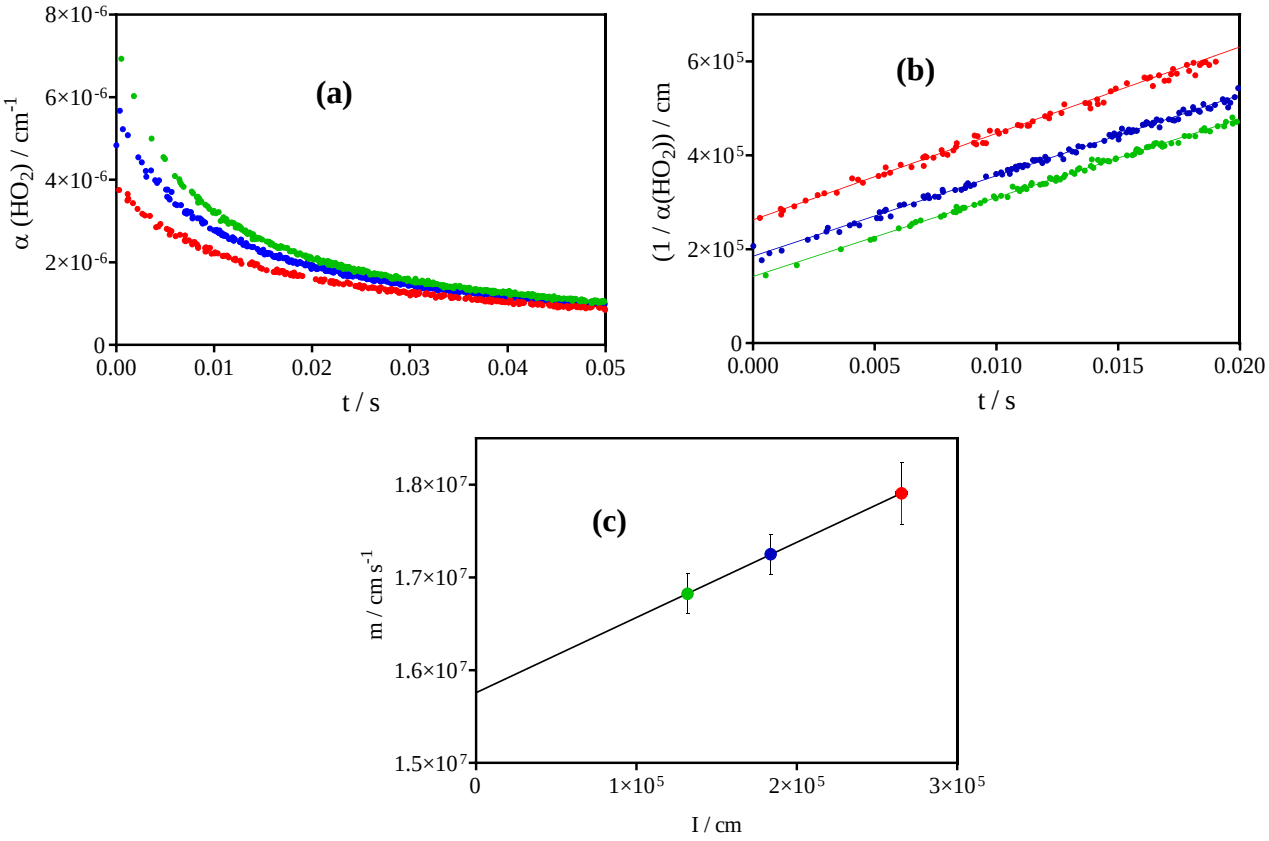

Figure 51: Example of measurement of HO_2 absorption cross-section using the kinetic method: graph (**a**) shows kinetic decays for 3 different Cl-atom concentrations, graph (**b**) shows the same signals plotted following Equation 40 with the linear regression over the first 20 ms, graph (**c**) shows the plot of slope m as a function of I, obtained in graph (**b**) for the 3 experiments.

These obtained absorption cross-sections are now used to determine the absorption cross-section of $C_2H_5O_2$ in back-to-back experiments. Figure 52 shows the principle of these measurements: Cl_2 is first photolysed in the presence of excess CH_3OH, leading to quantitative conversion of Cl atoms to HO_2 radicals: typical absorption-time profiles for 4 different Cl_2 concentrations are presented in the upper right graph (b) of Figure 52. In the next step, the gas flow of CH_3OH is removed, and excess C_2H_6 is added instead with keeping all other conditions constant. The absorption time profiles for $C_2H_5O_2$ are shown in the upper left graph 52(a). The HO_2 profiles show a faster decay than the corresponding $C_2H_5O_2$ profiles: this is in line with the rate constant of the HO_2 self-reaction being around 10 times faster than the rate constant of the $C_2H_5O_2$ self-reaction. In order to get a reliable extrapolation of $\alpha_{t=0\ ms}$, a plot of $1/\alpha$ as a function of time is generated for both species

(graph 52(c) and 52(d) for $C_2H_5O_2$ and HO_2, respectively) and a linear regression allows retrieving $\alpha_{t=0\ ms}$ from the intercept, as shown in Equation 40. For HO_2, the $\alpha_{t=0\ ms}$ values are then converted to absolute concentrations ($[HO_2]_{t=0\ ms}$) using the above determined absorption cross-section. Supposing that each Cl-atom is transformed into either one HO_2 radical or into one $C_2H_5O_2$ radical, i.e., $[HO_2]_{t=0\ ms} = [C_2HO_5]_{t=0\ ms}$, a plot of $\alpha(C_2H_5O_2)_{t=0\ ms} = f([HO_2]_{t=0\ ms})$ leads to a linear relationship with the slope equal to the absolute absorption cross-section of $C_2H_5O_2$. The lower graph (e) in Figure 52 shows the results obtained on four different days: for using either the strong HO_2 line at 6638.2 cm^{-1} (open circles and open diamonds), or the weak line at 6635.58 cm^{-1} (all other symbols, with the colored symbols representing the results from the experiment in Figure 52(c) and (d)).

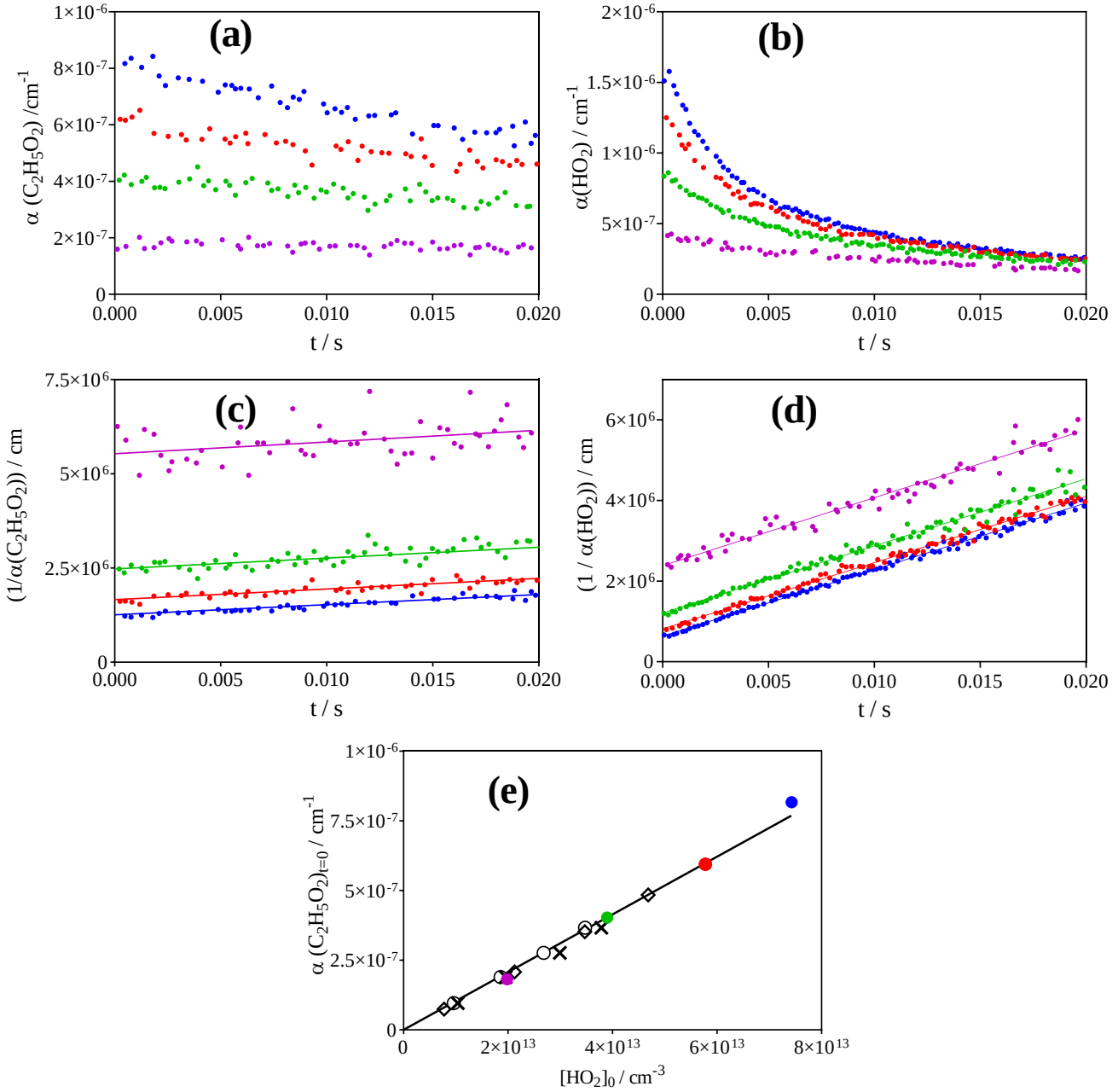

Figure 52: Example of measurement of the $C_2H_5O_2$ absorption cross-section relative to the HO_2 absorption cross-section. Upper graphs: $C_2H_5O_2$ (**a**) and HO_2 (**b**) absorption time profiles. Graphs (**c**) and (**d**): same profiles, converted to 1/α (see Equation 40) and linear regression over the first 20 ms following the photolysis pulse. Lower graph (**e**) shows plot of $\alpha\ (C_2H_5O_2)_{t=0\ ms} = f\ ([HO_2]_{t=0\ ms})$. $[O_2] = 2.8 \times 10^{18}$ cm^{-3}, $[C_2H_6] = 3.7 \times 10^{16}$ cm^{-3} for all experiments.

An absorption cross-section of $\sigma = (1.0 \pm 0.2) \times 10^{-20}$ cm^2 for $C_2H_5O_2$ at 7596 cm^{-1} is obtained from these experiments. The error bar of the absorption cross-section of $C_2H_5O_2$ is directly linked to the uncertainty in the rate constant of the HO_2 self-reaction.

4.3.3. Quantification of $C_2H_5O_2$ by Measuring the Rate Constant of $C_2H_5O_2$ + HO_2

The absorption cross-section of $C_2H_5O_2$ has also been determined by measuring the rate constant of the cross reaction between $C_2H_5O_2$ and HO_2. Indeed, the rate constant can be determined under different conditions by using either an excess of HO_2 over $C_2H_5O_2$ or an excess $C_2H_5O_2$ over HO_2. Using an excess of HO_2 leads to $C_2H_5O_2$ decays that are sensitive to the absolute concentration of HO_2, while the reverse case leads to HO_2 decays that are sensitive to the absolute concentration of $C_2H_5O_2$, and thus to its absorption cross-section. Therefore, measuring simultaneously the decays of both species over a large range of concentration ratios allows measuring the rate constant (from excess HO_2 experiments) and the absorption cross-section of $C_2H_5O_2$ (from excess $C_2H_5O_2$ experiments).

Figure 53 shows the $C_2H_5O_2$ and HO_2 decays where HO_2 was used in excess. The profiles of all the conditions shown in Figure 53 have simultaneously been fitted to a simple mechanism, with the experimental conditions presented in Table 4 and the mechanism presented in Table 5. The initial concentration of Cl-atom was fixed to 1.2×10^{14} molecules.cm^{-3} for all experiments, obtained from measuring pure HO_2 decays (no C_2H_6 added) in initial experiments.

Table 4: Conditions for experiments shown in Figure 53. Initial Cl-atom concentration was for all experiments 1.2×10^{14} molecules.cm^{-3}, total pressure was 100 Torr O_2, T = 295 K. $[C_2H_5O_2]$ and $[HO_2]$ concentrations taken from the model. Total radical concentrations are slightly below initial Cl-concentration due to (R 50).

$[C_2H_6]/ 10^{15}$ cm^{-3}	$[CH_3OH]/ 10^{15}$ cm^{-3}	$[C_2H_5O_2]_{max}/ 10^{13}$ cm^{-3}	$[HO_2]_{max}/10^{13}$ cm^{-3}	$[HO_2]/ [C_2H_5O_2]$
1.94	5.0	3.4	8.3	2.5
2.74	5.0	4.3	7.4	1.7
3.45	5.0	5.0	6.7	1.3
4.30	5.0	5.6	6.1	1.1

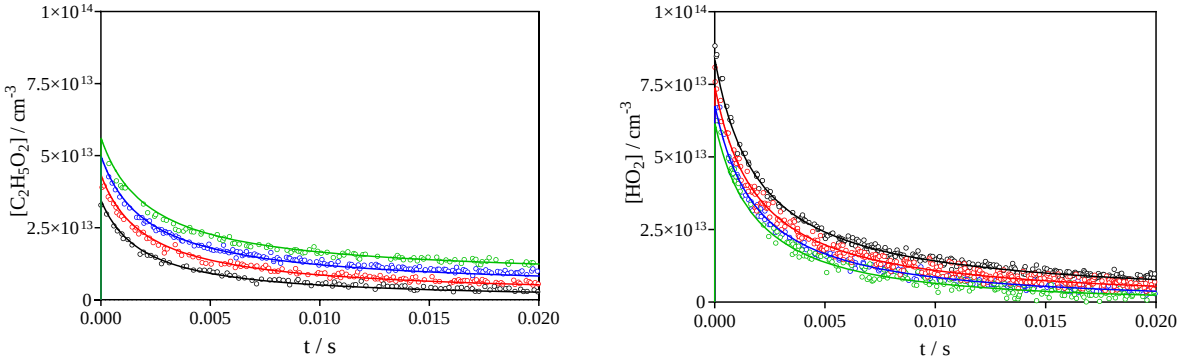

Figure 53: $C_2H_5O_2$ (left graphs) and HO_2 (right graphs) concentration time profiles for a total radical concentration of 1.2×10^{14} molecules.cm^{-3}. $C_2H_5O_2$ absorption time profiles have been converted using $\sigma = 1.0 \times 10^{-20}$ cm^2.

Table 5: Reaction mechanism used to fit all experiments in this work.

	Reaction	k/cm^{3}molecule^{-1}s^{-1}	Reference
(R 29a)	$2\ C_2H_5O_2 \rightarrow 2\ C_2H_5O + O_2$	3.2×10^{-14}	This work
(R 29b)	$2\ C_2H_5O_2 \rightarrow C_2H_5OH + CH_3CHO + O_2$	7.0×10^{-14}	This work
(R 30)	$C_2H_5O + O_2 \rightarrow CH_3CHO + HO_2$	8×10^{-15}	Fittschen et al., 1999
(R 20a)	$C_2H_5O_2 + HO_2 \rightarrow C_2H_5OOH + O_2$	6.2×10^{-12}	This work
(R 46)	$Cl + C_2H_6 \rightarrow C_2H_5 + HCl$	5.9×10^{-11}	Atkinson et al., 2006a
(R 47a)	$C_2H_5 + O_2 + M \rightarrow C_2H_5O_2 + M$	4.8×10^{-12}	Fernandes et al., 2015
(R 47b)	$C_2H_5 + O_2 \rightarrow C_2H_4 + HO_2$	$3\text{-}4\times 10^{-14}$	This work *
(R 48)	$Cl + CH_3OH \rightarrow CH_2OH + HCl$	5.5×10^{-11}	Atkinson et al., 2006a
(R 41)	$CH_2OH + O_2 \rightarrow CH_2O + HO_2$	9.6×10^{-12}	Atkinson et al., 2006a
(R 44)	$C_2H_5O_2 + C_2H_5O \rightarrow$ products	7×10^{-12}	This work
(R 49)	$2\ HO_2 \rightarrow H_2O_2 + O_2$	1.7×10^{-12}	Atkinson et al., 2004
(R 50)	$C_2H_5O_2 + Cl \rightarrow$ products	1.5×10^{-10}	Maricq et al., 1994
(R 51)	$C_2H_5O + HO_2 \rightarrow$ products	1×10^{-10}	Assaf et al., 2018b
(R 52)	$C_2H_5O_2 \rightarrow$ diffusion	2 s^{-1}	This work
(R 53)	$HO_2 \rightarrow$ diffusion	3 s^{-1}	This work

* This reaction is likely due to excited C_2H_5 radicals and the branching ratio between (R 47a) and (R 47b) depends on pressure and also on the mode of generation of the C_2H_5 radicals.

Under excess HO_2 conditions, $C_2H_5O_2$ decays are mainly due to its reaction with HO_2 and HO_2 decays are mainly due to its self-reaction. The HO_2 self-reaction is fast and is the major loss process under all reaction times. This is also shown in Figure 54 that presents the modelled profiles of the product of corresponding self-reaction (C_2H_5OH for $C_2H_5O_2$ and H_2O_2 for HO_2) and the product

of (R 20a) (C_2H_5OOH). The $C_2H_5O_2$ and HO_2 profiles could be well reproduced over the excess HO_2 concentration range using a rate constant of $k_{20a} = 6.2 \times 10^{-12}$ cm^3 molecule^{-1} s^{-1}.

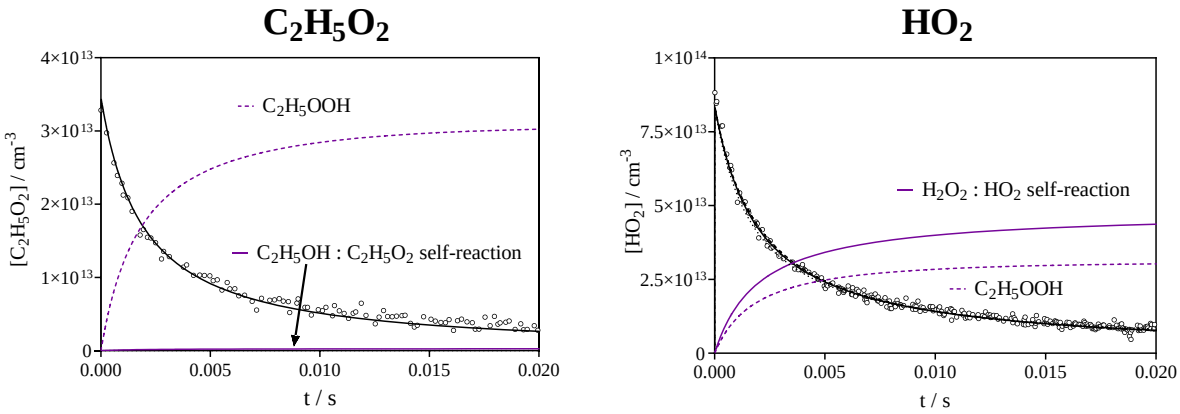

Figure 54: Experimental profiles taken under excess HO_2 conditions. The dashed lines represent modelled profiles of C_2H_5OOH, the product from (R 20a), while the full lines represent the product of the corresponding self-reaction (C_2H_5OH for $C_2H_5O_2$ and H_2O_2 for HO_2).

Then, the reaction of $C_2H_5O_2 + HO_2$ was studied using excess of $C_2H_5O_2$ and the decays of $C_2H_5O_2$ and HO_2 are shown in Figure 55. The profiles of these two species have simultaneously been fitted with the same mechanism as when HO_2 was used in excess with the experimental conditions presented in Table 6 and the mechanism presented in Table 5.

Table 6: Conditions for experiments shown in Figure 55. Initial Cl-atom concentration was for all experiments 1.2 × 10^{14} cm^{-3}, total pressure was 100 Torr O_2, T = 295 K. [$C_2H_5O_2$] and [HO_2] concentrations taken from the model. Total radical concentrations are slightly below initial Cl-concentration due to (R 50).

$[C_2H_6]/ 10^{15}$ cm^{-3}	$[CH_3OH]/ 10^{15}$ cm^{-3}	$[C_2H_5O_2]_{max}/ 10^{13}$ cm^{-3}	$[HO_2]_{max}/10^{13}$ cm^{-3}	$[HO_2]/ [C_2H_5O_2]$
5.91	2.8	8.1	3.6	0.4
7.50	2.8	8.6	3.0	0.3

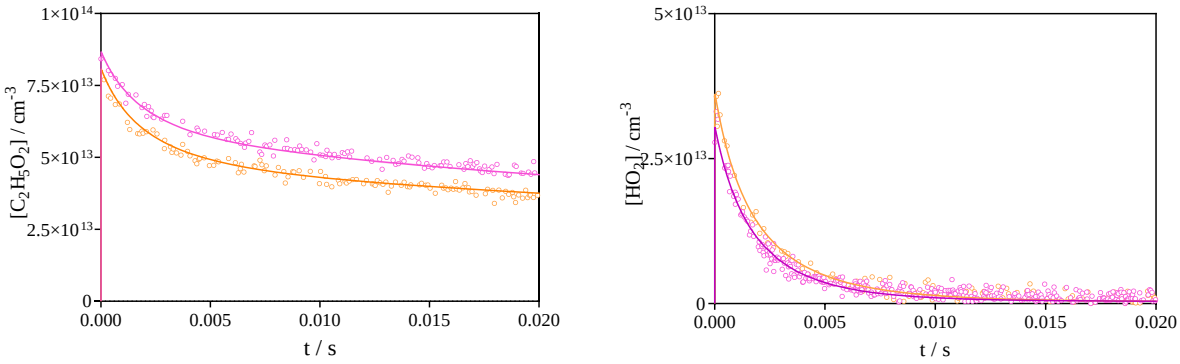

Figure 55: $C_2H_5O_2$ (left graphs) and HO_2 (right graphs) concentration time profiles for a total radical concentration of 1.2×10^{14} molecules.cm^{-3}. $C_2H_5O_2$ absorption time profiles have been converted using $\sigma = 1.0 \times 10^{-20}$ cm^2.

Under excess $C_2H_5O_2$ conditions, HO_2 decays are mainly due to its reaction with $C_2H_5O_2$ and $C_2H_5O_2$ decays are mainly due to its self-reaction. The $C_2H_5O_2$ decreases rapidly over the first few ms, due to its loss through (R 20a). Then, at longer reaction times when HO_2 concentration gets low, the $C_2H_5O_2$ decays slow down because the self-reaction becomes the major loss process and this reaction is slow for $C_2H_5O_2$ radicals. This is also shown in Figure 56 that presents the modelled profiles of the product of corresponding self-reaction (C_2H_5OH for $C_2H_5O_2$ and H_2O_2 for HO_2) and the product of (R 20a) (C_2H_5OOH).

The $C_2H_5O_2$ and HO_2 profiles (under excess of $C_2H_5O_2$) could also be well reproduced over the entire concentration range using a rate constant of $k_{20a} = 6.2 \times 10^{-12}$ cm^3 molecule^{-1} s^{-1} and the absorption cross-section for $C_2H_5O_2$ ($\sigma = 1.0 \times 10^{-20}$ cm^2) obtained in back-to-back experiments, thus validating the obtained value for the $C_2H_5O_2$ absorption cross-section.

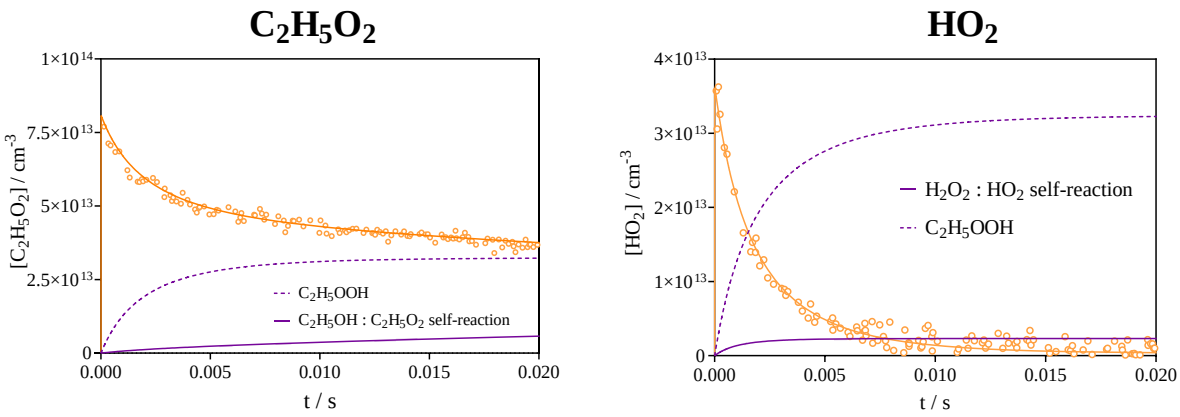

Figure 56: Experimental profiles taken under excess $C_2H_5O_2$ conditions. The dashed lines represent modelled profiles of C_2H_5OOH, the product from (R 20a), while the full lines represent the product of the corresponding self-reaction (C_2H_5OH for $C_2H_5O_2$ and H_2O_2 for HO_2).

Then, different rate constants for the cross reaction k_{20a} have been tested also: indeed, despite several previous measurements over the last decades (Boyd et al., 2003; Cattell et al., 1986; Dagaut et al., 1988b; Fenter et al., 1993; Maricq & Szente, 1994; Noell et al., 2010; Raventós-Duran et al., 2007b), there is no good agreement for this rate constant. The two recent determinations from Noell et al. (Noell et al., 2010) (5.57×10^{-12} $cm^3molecule^{-1}\,s^{-1}$ from UV/near IR absorption) and Boyd et al. (Boyd et al., 2003) (8.14×10^{-12} $cm^3molecule^{-1}\,s^{-1}$ from UV absorption) are considered by the IUPAC committee as being carried out by the most reliable methods, however they vary by about a factor of 1.5. These two limits have been tested by trying to adjust both profiles over the entire concentration range (excess of HO_2 and excess $C_2H_5O_2$) and the results are shown in Figure 57.

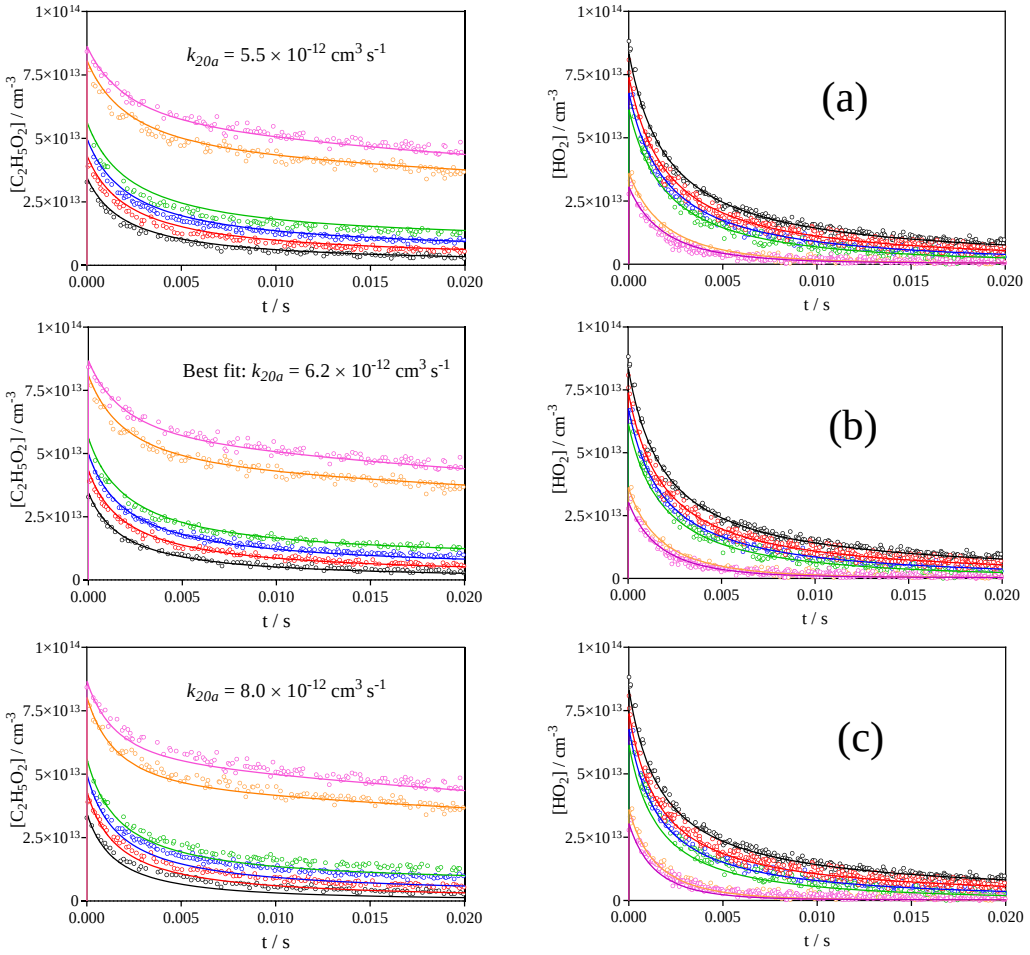

Figure 57: $C_2H_5O_2$ (left graphs) and HO_2 (right graphs) concentration time profiles for a total radical concentration of 1.2×10^{14} molecules.cm^{-3}. $C_2H_5O_2$ absorption time profiles have been converted using $\sigma = 1.0 \times 10^{-20}$ cm^2. Centre graphs (**b**): best fit with $k_{20a} = 6.2 \times 10^{-12}$ cm^{3}molecule^{-1} s^{-1}, upper graphs (**a**): model with of $k_{20a} = 5.5 \times 10^{-12}$ cm^{3}molecule^{-1} s^{-1}, lower graphs (**c**): model with $k_{20a} = 8.0 \times 10^{-12}$ cm^3 molecule^{-1} s^{-1}.

In the upper graphs 57(a), the rate constant k_{20a} has been set to the lower limit $k_{20a} = 5.5 \times 10^{-12}$ cm^{3}molecule^{-1} s^{-1}, leading to $C_2H_5O_2$ and (less pronounced) HO_2 decays that are too slow. In the lower graphs (c), the rate constant k_{20a} has been set to the upper limit $k_{20a} = 8 \times 10^{-12}$ cm^{3}molecule^{-1} s^{-1}, leading to too fast decays of both species.

In conclusion, these kinetic experiments show the best fit for both species over the entire concentration range when using the absorption cross-section for $C_2H_5O_2$ obtained in back-to-back experiments. However, it should of course be noted, that in the end both approaches rely on the absorption cross-section of HO_2 and therefore both methods cannot be considered as independent methods. The absorption cross-section of HO_2 might vary through pressure broadening (which is

taken into account), and also during the experiment through small and unnoted shifts in the wavelength of the DFB laser emission (the linewidth of the absorption lines of the HO_2 are on the order of 0.02 cm^{-1} FWHM at 50 Torr He). However, in our experiments the HO_2 absorption cross-section is under most conditions constantly being "measured": a major loss of HO_2 in most experiments is the self-reaction, and thus the HO_2 decays are sensitive to the absolute concentration of HO_2, i.e., to the absorption cross-section that has been used to transform the absorption time profiles to concentration time profiles. Therefore, it can be said that both approaches have determined the absorption cross-section of $C_2H_5O_2$ relative to the rate constant of the HO_2 self-reaction. The IUPAC committee (Atkinson et al., 2004) estimates the uncertainty of the HO_2 self-reaction rate constant to ± 15%, which we use as a basis to estimate the uncertainty of our rate constant, with an additional 10% for uncertainties in the fitting of the rate constant: $k_{20a} = (6.2 \pm 1.5) \times 10^{-12}$ $cm^3 molecule^{-1} s^{-1}$.

4.3.4. Comparison of the Absorption Cross-section with Literature Data

The absorption cross-section of $C_2H_5O_2$ was first obtained by Atkinson and Spillman (Atkinson & Spillman, 2002) using 193 nm photolysis of 3-pentanone as precursor. Applying the kinetic method, they obtained at the peak $\sigma = (3 \pm 1.5) \times 10^{-21}$ cm^2, which is 3 times smaller than the present value. A higher absorption cross-section had also been determined previously by our group for the CH_3O_2 radical (Farago et al., 2013). One possible reason for this low absorption cross section obtained by Atkinson and Spillman might be that it is based on the kinetic method using low initial radical concentrations. Thus the $C_2H_5O_2$ concentration has to be measured over long reaction times in order to obtain a sizeable decay, but the possible loss through diffusion out of the photolysis volume or due to wall loss, possibly non-negligible over such long reaction times, has not been considered in the data evaluation. This can lead to an overestimation of the radical concentration and therefore an underestimation of the absorption cross-section. Another reason might be the precursor: the reaction of $C_2H_5 + O_2$ can also form small amounts of HO_2 through (R 47a), around 1% of the initial Cl-atom concentration led to the formation of HO_2 in our experiments, this is shown in Figure 61. Atkinson and Spillman used 193 nm photolysis of 3-pentanone, that leaves considerably higher amounts of excess energy in the fragments than our method, based on H-atom abstraction. Hence, the fraction of C_2H_5 radicals that react through (R 47a) might be considerably higher than in our experiments. This could lead to the formation of a non-negligible initial HO_2 concentration which participates in the removal of $C_2H_5O_2$ and would

thus cause a systematic error when using the kinetic method. This is also in line with the observation of Atkinson and Spillman, that in their experiments the rate constant of the $C_2H_5O_2$ self-reaction decreased with increasing pressure showing that the apparent rate constant was inversely pressure dependent (D. Atkinson, private communication). An increased cooling of the hot C_2H_5 radical with increasing pressure would lead to a lower HO_2 concentration and thus to a slow-down of the $C_2H_5O_2$ decay.

Rupper et al. (Rupper et al., 2007) estimated the absolute absorption cross-section to $\sigma = 4.4 \times 10^{-21}$ cm^{-2} by calculating the initial Cl-atom concentration from the difference between the photolysis laser energy with and without precursor, supposing that all generated Cl-atoms lead to formation of one $C_2H_5O_2$. In a more recent work from the same group, Melnik et al. (Melnik & Miller, 2013) have estimated the absorption cross-section by dual-CRDS method where the absorption of $C_2H_5O_2$ was measured on one path while the concentration of HCl was measured simultaneously on the other path thanks to its known absorption cross-section. Assuming again that each HCl-molecule had generated one $C_2H_5O_2$ radical, they found an absorption cross-section of $\sigma = 5.29 \times 10^{-21}$ cm^{-2} that is nearly 2 times lower than the value obtained in this work. It is unlikely that the difference in the bandwidth of the excitation laser sources (0.01 cm^{-1} for Melnik and $<1 \times 10^{-4}$ cm^{-1} for this work) can cause this difference, since the absorption band is unstructured and much larger than the bandwidth of both laser sources.

A possible explanation for this difference in the absorption cross-section might be that Melnik et al. and Rupper et al. both consider the complete conversion of Cl-atoms into $C_2H_5O_2$ radicals. A simple model presented by Melnik et al. (Melnik et al., 2010) shows the complete conversion of Cl-atoms into $C_2H_5O_2$. However, the very fast reactions of Cl-atoms with $C_2H_5O_2$ ($k_{55} = 1.5 \times 10^{-10}$ $cm^3molecule^{-1}\,s^{-1}$) (Maricq et al., 1994) and C_2H_5 ($k = 3 \times 10^{-10}$ $cm^3molecule^{-1}\,s^{-1}$) (Seakins et al., 1993) are not taken into consideration in this model, even though these reactions are non-negligible under their conditions where they used very high initial Cl-atom concentrations, well above 10^{15} molecules.cm^{-3}, combined with relatively low C_2H_6 concentrations (1×10^{16} molecules.cm^{-3}). These reactions lead to a concentration of $C_2H_5O_2$ that might be well below the initial Cl-atom concentration, depending on the overall radical concentration as well as on the C_2H_6 concentration. Figure 58 shows a simulation using the model from Melnik et al., but also including the two fast reactions ($C_2H_5O_2$ + Cl and C_2H_5 + Cl). The left graph shows the result with initial concentrations

used by Melnik et al. ($[Cl]_0 = 2 \times 10^{15}$ molecules.cm^{-3} and $[C_2H_6]_0 = 1 \times 10^{16}$ molecules.cm^{-3}), the right graph shows the model result with typical conditions such as used in this work for the measurement of the absorption cross-section ($[Cl]_0 = 5 \times 10^{13}$ molecules.cm^{-3}and $[C_2H_6]_0 = 3 \times 10^{16}$ molecules.cm^{-3}). Using high Cl/low C_2H_6 conditions of Melnik et al. shows that only 63% of the Cl-atoms have been converted to $C_2H_5O_2$, while 28% of the Cl-atoms have reacted with $C_2H_5O_2$ and 8% have reacted with C_2H_5. Using low Cl/high C_2H_6 conditions (right graph) shows that almost all Cl-atoms have been converted to $C_2H_5O_2$ and less than 1% of the Cl-atoms have reacted with either $C_2H_5O_2$ or C_2H_5 (right y-scale in the right graph). From this model one can suspect that the obtained absorption cross-sections of Melnik et al. (Melnik et al., 2010) and Rupper et al. (Rupper et al., 2007) are strongly underestimated, and a correction of the obtained value of Melnik et al., based on the more complete model presented here, would lead to $\sigma = 8.8 \times 10^{-21}$ cm^{-2}, which gets into good agreement with the value obtained in this work.

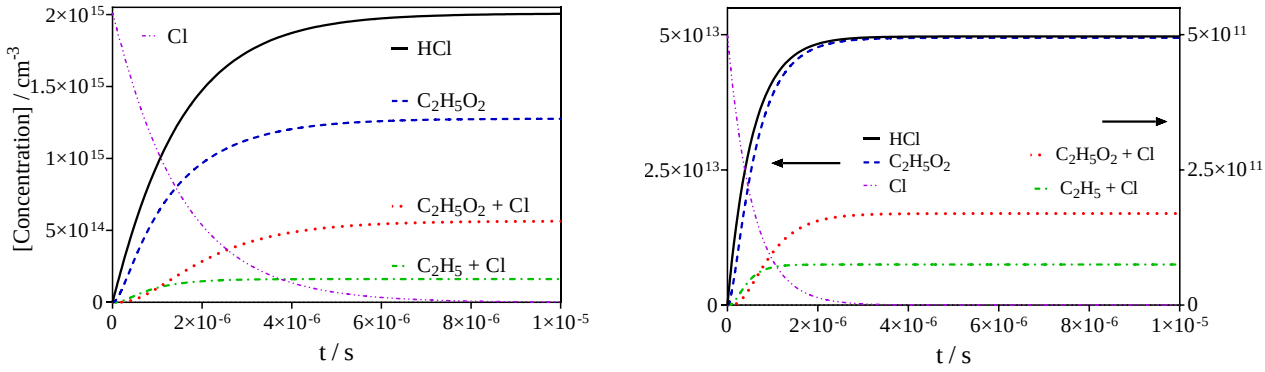

Figure 58: Simulation of conversion of Cl-atoms (violet dashed dot) into HCl (black) and $C_2H_5O_2$ (blue dashed): model taken from Melnik et al., completed with the reactions of Cl with $C_2H_5O_2$ ($k = 1.5 \times 10^{-10}$ cm^{3}s^{-1}) (Maricq et al., 1994) (red dotted) and C_2H_5 ($k = 3 \times 10^{-10}$ cm^{3}s^{-1}) (Seakins et al., 1993) (green dashed dotted): left graph conditions such as used in Melnik et al.(Melnik et al., 2010), right graph conditions such as used in this work. The products from the reaction of Cl with $C_2H_5O_2$ (red) and with C_2H_5 (green) are zoomed in the right graph by a factor of 100 (right y-axis applies).

4.3.5. Measuring the Relative Absorption Spectrum of $C_2H_5O_2$

In order to obtain the absorption spectrum of $C_2H_5O_2$, kinetic decays have been measured under the same conditions at 15 different wavelengths in the range accessible with our DFB laser (7596–7630 cm^{-1}). The relative absorption coefficients are put on an absolute scale by comparison with

the absorption cross-section at 7596.47 cm^{-1}. Table 7 presents the obtained results, and Figure 59 compares the data of this work with two literature results.

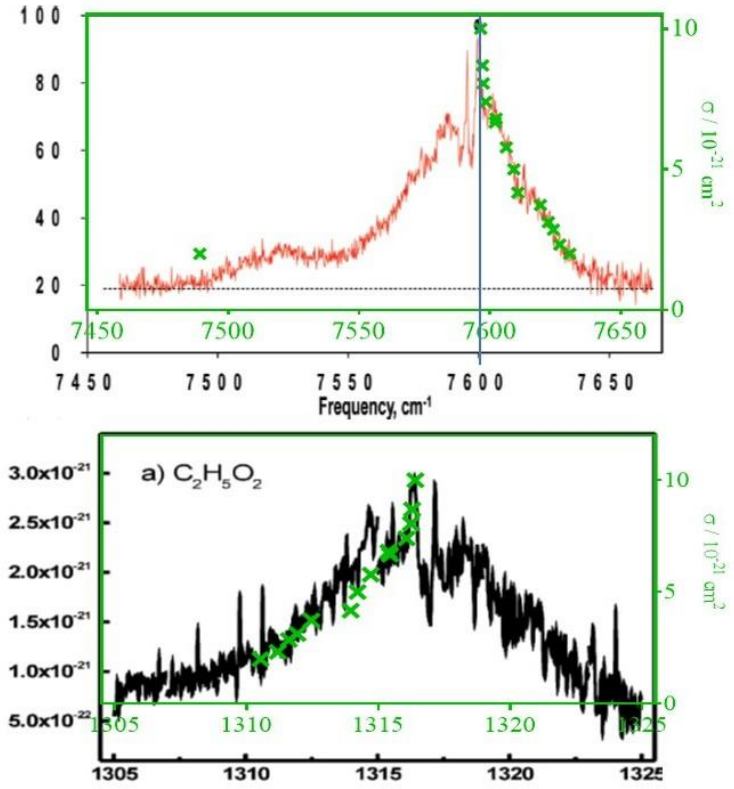

Figure 59: $C_2H_5O_2$ absorption coefficients at different wavelengths obtained in this work (green crosses and green axis), overlaid onto the spectrum obtained by Melnik et al. (Melnik et al., 2010) (upper graph, Reprinted with permission from (Melnik et al., 2010), Copyright 2010 American Chemical Society) and Atkinson and Spillman (Atkinson & Spillman, 2002) (lower graph, Reprinted with permission from (Atkinson & Spillman, 2002), Copyright 2002 American Chemical Society). In the upper graph the data have been shifted by 4 cm^{-1}, and in both graphs our data have been scaled on the y-axis, i.e., apparently there is a baseline shift in both comparisons.

The upper graph shows that the spectrum obtained in this work (green symbols and green axis apply) agrees well with the spectrum obtained by Melnik et al. (Melnik et al., 2010) if our data are shifted by 4 cm^{-1}. Possibly, there is a mistake in the Melnik figure (T. Miller, private communication), since the peak absorption is given at 7596 cm^{-1} in the text, same as in our case, however the peak is located at 7600 cm^{-1} in the figure, indicated by a blue vertical line. In the lower graph, our data (again in green) are overlaid to the spectrum obtained by Atkinson and Spillman (Atkinson & Spillman, 2002). Both comparisons show a good agreement of the spectrum when our data are scaled on the y-axis, i.e., when we suppose a shift in the baseline of both literature spectra (around 23% of the peak absorption for Atkinson and Spillman and 15% for Melnik et al.). Melnik

et al. discussed in their paper about such a baseline shift (dashed line in their figure) and attributed it to a broadband absorber, formed simultaneously during the photolysis. Indeed, they determined their baseline by measuring ring-down events with the photolysis laser blocked. In this case, a broadband absorber formed simultaneously to the $C_2H_5O_2$ radical would induce a baseline shift. Taking into account this shift (horizontal dashed line in the upper graph of Figure 59), they have calculated the absorption cross-section above this plateau. No explanation for a possible baseline shift in the spectrum of Atkinson and Spillman can be given.

Table 7: $C_2H_5O_2$ Absorption cross-sections at different wavelengths.

Wavenumber/cm^{-1}	**σ/10^{-20} cm^2**
7596.47	10.0
7597.20	8.7
7597.44	8.1
7598.40	7.4
7602.02	6.7
7602.38	6.8
7606.25	5.8
7609.16	5.0
7610.66	4.2
7619.28	3.7
7622.36	3.1
7624.28	2.9
7626.72	2.3
7630.50	2.0
7489.16	2.0

To conclude, the absorption cross-section of $C_2H_5O_2$ in $\tilde{A}$-$\tilde{X}$ electronic transition has been determined to be $\sigma = 1\times10^{-20}$ cm^2 on the peak at 7596.47 cm^{-1}. It has been also validated by measuring the rate constant of $C_2H_5O_2$ with HO_2 which was found to be $k_{20a} = 6.2\times10^{-12}$ cm^{3}molecule^{-1}s^{-1}, a value close to one recommended by IUPAC. Then, this cross-section along with the rate constant of $C_2H_5O_2$ with HO_2 was used to study the self-reaction of $C_2H_5O_2$. The obtained cross-section is used to convert $C_2H_5O_2$ absorption time profiles into concentration time profiles and the rate constant of $C_2H_5O_2$ with HO_2 is essential for extracting the branching ratio of $C_2H_5O_2$ self-reaction.

4.3. Kinetic study of $C_2H_5O_2$ radicals

When studying the $C_2H_5O_2$ self-reaction (R 29), several secondary reactions can be important and should be taken into account: the reaction of $C_2H_5O_2$ with HO_2 (R 20a) and with C_2H_5O (R 44).

The $C_2H_5O_2$ self-reaction:

$$C_2H_5O_2 + C_2H_5O_2 \rightarrow C_2H_5O + C_2H_5O + O_2 \quad \text{(R 29a)}$$

$$\rightarrow C_2H_5OH + CH_3CHO + O_2 \quad \text{(R 29b)}$$

and, in presence of O_2:

$$C_2H_5O + O_2 \rightarrow CH_3CHO + HO_2 \quad \text{(R 30)}$$

The $C_2H_5O_2$ radicals react with HO_2:

$$C_2H_5O_2 + HO_2 \rightarrow C_2H_5OOH + O_2 \quad \text{(R 20a)}$$

The $C_2H_5O_2$ radicals react also with C_2H_5O:

$$C_2H_5O_2 + C_2H_5O \rightarrow \text{products} \quad \text{(R 44)}$$

The rate constant of the reaction of $C_2H_5O_2$ with HO_2 obtained in this work, $k = 6.2\times10^{-12}$ $cm^3molecule^{-1}s^{-1}$, is used for extracting the branching ratio of the $C_2H_5O_2$ self-reaction. The reaction of $C_2H_5O_2$ with C_2H_5O has been also studied to check if it will play a role in the $C_2H_5O_2$ self-reaction.

4.3.1. Rate constant of the reaction of $C_2H_5O_2$ with C_2H_5O

In the work of Noell et al. (Noell et al., 2010) it turned out that the reaction of $C_2H_5O_2$ with C_2H_5O (R 44) was important under their conditions. In their experiments, using different O_2 concentrations, a fast rate constant of $k_{44} = 1.5\times10^{-11}$ $cm^3molecule^{-1}s^{-1}$ was extracted. Even though experiments in our work were carried out in 100 Torr O_2 (compared to 50 Torr O_2 in Noell et al.) making (R 30) very rapid ($k' \approx 24000$ s^{-1}) and hence the stationary concentration of C_2H_5O very low, it turned out during data evaluation of the self-reaction experiments, that (R 44) would still have a small influence on the HO_2 profiles. A decrease in the HO_2 profiles was observed when using the fast rate constant k_{44} obtained by (Noell et al., 2010) since the reaction of C_2H_5O with $C_2H_5O_2$ (R 44) becomes competitive with the reaction sequence forming HO_2 (R 29a) / (R 30). For this reason, we have performed some experiments with low O_2 concentration in order to re-

determine k_{44} under our conditions. Figure 60 show experiments using 4 different initial Cl-concentrations: the left graph shows experiments carried out under low O_2 (90 Torr N_2 and 10 Torr O_2: $[O_2] \sim 3\times10^{17}$ molecules cm^{-3}), experiments in the right graph were carried out under high O_2 (100 Torr O_2: $[O_2] \sim 3\times10^{18}$ molecules cm^{-3}). The results show that the $C_2H_5O_2$ profiles (lower graphs) are very similar between the two conditions, however the HO_2 profiles (upper graphs) present strong differences:

- in the case of 100 Torr O_2, the HO_2 concentrations just after the photolysis pulse are higher compared to the case of 90 Torr N_2 / 10 Torr O_2. This is in line with the hypotheses that this initial HO_2 is formed from the collision between hot C_2H_5 and O_2: with increasing N_2 and decreasing O_2, collisions with N_2 will cool down excited C_2H_5 and the reaction $C_2H_5 + O_2 \rightarrow C_2H_4 + HO_2$ (R 47b) will become less important.
- HO_2 signals initially rise in the case of 100 Torr O_2 while they decay from the beginning in the case of 90 Torr N_2 / 10 Torr O_2. Under high O_2 conditions, HO_2 formation from the reaction sequence (R 29a) / (R 30) is initially faster than its consumption through (R 20a) and this is due to the fast conversion of C_2H_5O ($k' = 24\ 000\ s^{-1}$), until after 2-3 ms steady-state is reached and HO_2 decays at the same pace as $C_2H_5O_2$. At low O_2, HO_2 formation from the reaction sequence (R 29a) / (R 30) is slower than (R 20a) since the conversion of C_2H_5O into HO_2 (R 30) is 10 times slower making the reaction of HO_2 with $C_2H_5O_2$ competitive for C_2H_5O.

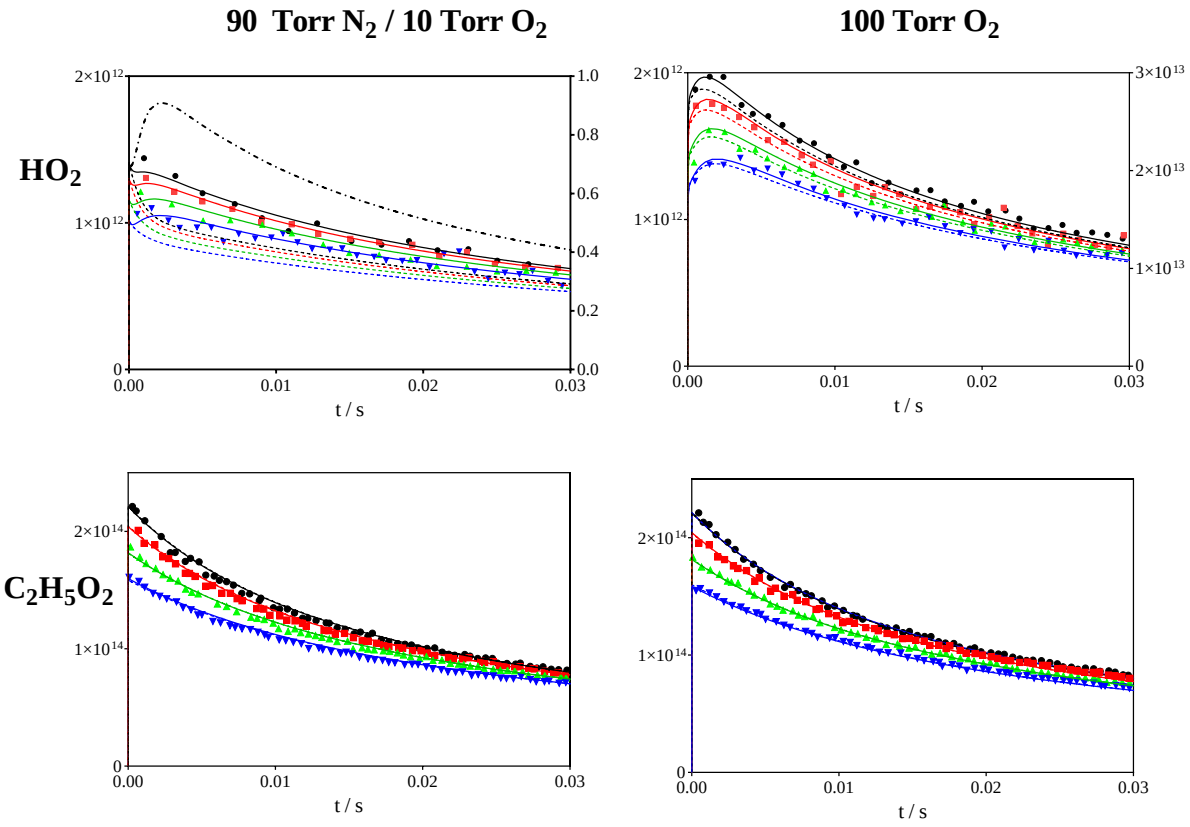

Figure 60: Experiments for determination of the rate constant between $C_2H_5O_2$ and C_2H_5O: upper graphs show HO_2 profiles, lower graphs show simultaneously measured $C_2H_5O_2$ profiles. Left graphs: 90 Torr N_2 / 10 Torr O_2, right graphs: 100 Torr O_2. Initial Cl-concentration was 2.26, 2.08, 1.85 and 1.6×10^{14} cm^{-3} for the experiments marked with black, red, green and blue dots, respectively. Full lines: model in Table 5 with $k_{44} = 7\times10^{-12}$ cm^3s^{-1}, dotted coloured lines $k_{44} = 1.5\times10^{-11}$ cm^3s^{-1}, dashed-dotted black line $k_{44} = 0$, for highest radical concentration only.

Those experiments were fitted using the model presented in Table 5 with varying the rate constant of the reaction (R 44). Using the rate constant for (R 44) recommended by Noell et al. ($k_{44} = 1.5\times10^{-11}$ $cm^3molecule^{-1}s^{-1}$) did not allow to reproduce the HO_2 profiles under low O_2 conditions where the modelled HO_2 profiles decrease much faster than the experimental profiles (dotted coloured lines in the upper graph of Figure 60). The HO_2 profiles show the best fit when using the rate constant of $k_{44} = 7\times10^{-12}$ $cm^3molecule^{-1}s^{-1}$, nearly two times slower (full lines in the upper graphs of Figure 60). It can be seen that even with the lower rate constant, this reaction still has an influence on the HO_2 profiles, especially under low O_2 conditions where HO_2 formation from the reaction sequence (R 29a) / (R 30) is slower than (R 20a) since the conversion of C_2H_5O into HO_2 (R 30) is 10 times slower making the reaction of HO_2 with $C_2H_5O_2$ competitive for C_2H_5O. Ignoring this reaction did not allow to reproduce the HO_2 profiles under low O_2 conditions as shown in the modelled profile

without (R 44) (dashed-dotted line in the upper graph of Figure 60) for the highest radical concentration only.

Not many detail are given in the previous work of Noell et al. on how the rate constant was determined, therefore it is difficult to understand the differences and no good explanation can be given for the disagreement of these results with the result from Noell et al. (Noell et al., 2010). From these experiments we have chosen to use $k_{44} = 7\times10^{-12}$ $cm^3molecule^{-1}s^{-1}$ for studying the $C_2H_5O_2$ self-reaction. It should however be noted that the reaction of $C_2H_5O_2$ with C_2H_5O has a smaller impact on the retrieved rate constant and branching ratio of the $C_2H_5O_2$ self-reaction due to the 2 times higher O_2 concentration used in our experiments, compared to Noell et al.

4.3.2. Rate constant and branching ratio of the self-reaction of $C_2H_5O_2$

The rate constant of the self-reaction of $C_2H_5O_2$ has been determined in this work by following simultaneously $C_2H_5O_2$ and HO_2. Figure 61 presents an example of $C_2H_5O_2$ and HO_2 profiles obtained from the photolysis of varying concentrations of Cl_2 in presence of $[C_2H_6] = 2\times10^{16}$ molecules cm^{-3} and $[O_2] = 3\times10^{18}$ molecules cm^{-3}. The HO_2 profiles do not start at zero just after the photolysis pulse: this is due to the reaction of $C_2H_5 + O_2$ (R 47a), leading to the formation of around 1% or less of HO_2. This has already been observed in earlier studies (Clifford et al., 2000; Noell et al., 2010).

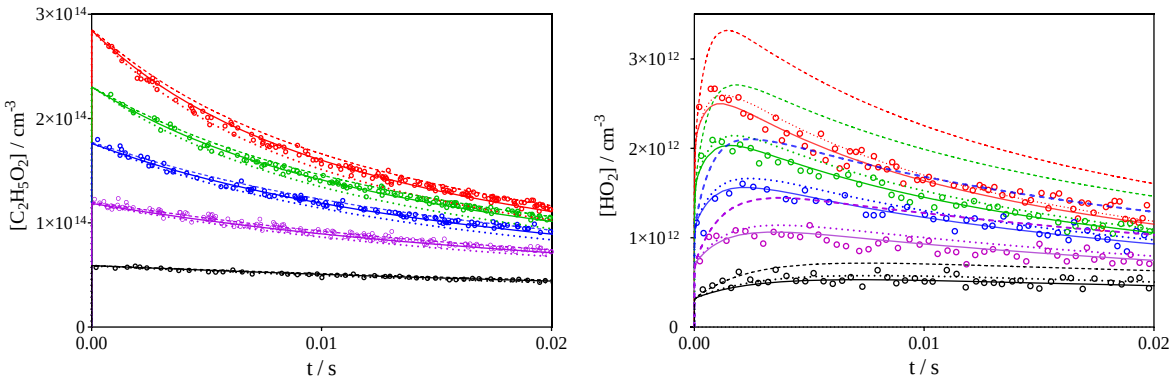

Figure 61: $C_2H_5O_2$ (left graph) and HO_2 (right graph) profiles obtained from the 351 nm photolysis of $[Cl_2]$ = 0.6, 1.3, 1.9, 2.5, and 3 $\times10^{16}$ cm^{-3}, from bottom to top. Full lines model from Table 5**,** dotted lines model using values from Noell et al., dashed lines model with IUPAC recommended values for k_{29a} and k_{29b} (see Table 8).

High C_2H_6 concentrations (2-3$\times10^{16}$ molecules cm^{-3}), leading to pseudo-first-order rate constant for the reaction C_2H_6 + Cl (R 46) of ~ 2 $\times10^5$ s^{-1}, have always been used in order to minimize the

influence of the fast reaction of $C_2H_5O_2$ + Cl (R 50). A fast reaction of Cl atoms with $C_2H_5O_2$ has been included in the model with 1.5×10^{-10} cm^3s^{-1} but was always negligible: even at the highest radical concentration, only around 0.3% of the initial Cl atoms reacted with $C_2H_5O_2$. Also, most experiments have been carried out at 100 Torr O_2 in order to rapidly convert C_2H_5O into HO_2 through (R 30) and minimize the impact of (R 44). The rate constant k_{29} and the branching ratio α have then been extracted by fitting simultaneously the profiles of HO_2 and $C_2H_5O_2$ for an entire series of experiments with varying Cl-concentrations. In the example in Figure 61, the initial radical concentration has been varied by around a factor of 6, making the $C_2H_5O_2$ reactivity varying on our typical time scale of 20 ms from near stable for the lowest concentration (black symbols) to a loss of more than 50% of $C_2H_5O_2$ for the highest concentration (red symbols). The rate constant k_{42b}, i.e. the fraction of C_2H_5 radicals that react with O_2 leading to the formation of HO_2 radicals, has been adjusted such as to best reproduce the non-zero HO_2 concentration immediately after the laser pulse. This fraction was always around 1%, in good agreement with previous findings.

The HO_2 and $C_2H_5O_2$ profiles are very well reproduced over the full range of initial radical concentrations (full lines in Figure 61) using the model given in Table 5. Figure 61 also show the results of two other models with the rate constants of (R 29a), (R 20a) and (R 44) varied to match either the results from Noell et al. (Noell et al., 2010) (dotted lines) or the current IUPAC recommendations (Atkinson al., 2006) (dashed lines). Table 8 summarizes the rate constants used for these models in Figure 61.

Table 8: Values used for models in Figure 61, all rate constants are in units $cm^3molecule^{-1}s^{-1}$.

	Reaction	This work	Noell et al., 2010	IUPAC (Atkinson et al., 2006a)
(R 29a)	$2\ C_2H_5O_2 \rightarrow 2\ C_2H_5O + O_2$	3.2×10^{-14}	3.33×10^{-14}	4.79×10^{-14}
(R 29b)	$2\ C_2H_5O_2 \rightarrow C_2H_5OH + CH_3CHO + O_2$	7.0×10^{-14}	8.57×10^{-14}	2.81×10^{-14}
(R 29a)	$k / 10^{-13}$ $cm^3molecule^{-1}s^{-1}$	**1.0 ± 0.2***	1.19 ± 0.04	0.76 ± 0.4
(R 29a)	k_{obs} ** $/ 10^{-13}$ $cm^3molecule^{-1}s^{-1}$	1.34	1.52	1.24
(R 29a)	r'	**0.31 ± 0.06***	0.28 ± 0.06	0.63
(R 20a)	$C_2H_5O_2 + HO_2 \rightarrow C_2H_5OOH + O_2$	$(6.2 \pm 1.5)\times10^{-12}$	$(5.6 \pm 0.4)\times10^{-12}$	6.9×10^{-12}
(R 44)	$C_2H_5O_2 + C_2H_5O \rightarrow$ products	$(7 \pm 1.5)^* \times 10^{-12}$	$(15 \pm 7) \times 10^{-12}$	-

*Error bars of 20% are estimated, mostly due to uncertainties in the absolute absorption cross sections of HO_2 and $C_2H_5O_2$

** $k_{obs} = k\ (1+r')$

Using the rate constants of the current IUPAC recommendations (Atkinson et al., 2006a), the modelled $C_2H_5O_2$ profiles show a very minor deviation from our measurements (the model decays too slowly), however the disagreement of the modelled HO_2 profiles with our measurements is huge: the model predicts too much HO_2, far beyond any experimental uncertainty. This disagreement is due to the much higher radical yield r in (R 29a), which is not counterbalanced by the overall lower rate constant k_{29} or the higher rate constant of (R 20a). Using the rate constants from Noell et al. (Noell et al., 2010), the modelled HO_2 profiles are in very good agreement with our measurements (the model slightly overpredicts the HO_2 concentration by around 10%, within the experimental uncertainty), but for $C_2H_5O_2$ the model predicts faster decays than the experimental profiles, especially at longer reaction times. This slight disagreement is due to a combination of the different rate constants for the three major radical-radical reactions used in both models: in the work of Noell et al., they used a higher rate constant of (R 44), a lower rate constant of (R 20a) and a slightly faster (R 29a) with a lower radical yield compared to our model. Since this slight disagreement is within the experimental uncertainty, and even though our measurements are not with a perfect agreement with the data from Noell et al. (Noell et al., 2010), this work confirms their finding of an overall faster rate constant for (R 29a) together with a lower branching ratio for the radical channel, compared to current recommendations.

Previous studies used GC/MS (Anastasi et al., 1983) and FTIR (Niki et al., 1982; Wallington et al., 1989) for obtaining branching ratios from the measurements of end products of the $C_2H_5O_2$ self-reaction: the branching ratio r was determined from the measurements of the product ratios $[C_2H_5OH]/[CH_3CHO]$ following continuous photolysis of a mixture of Cl_2 / C_2H_6 / O_2. The discrepancy in the branching ratio might be due to unaccounted secondary chemistry that could have occurred in these end products studies. Diethylperoxide $C_2H_5O_2C_2H_5$, possibly formed through the pathway (R 29c), could have been photolysed:

$$C_2H_5O_2C_2H_5 + h\upsilon \rightarrow 2C_2H_5O \qquad \text{(R 54)}$$

This would generate ethoxy radicals, which would not be distinguishable from the ethoxy radicals generated through pathway (R 29a). Thus, the measurements of the product CH_3CHO will be the sum of the ethoxy radicals formed from radical channel in the $C_2H_5O_2$ self-reaction and the ones formed from the photolysis of the diethyl peroxide. This would then lead to a systematically higher branching ratio r for the radical channel.

4.4. Conclusion

This chapter presented a new determination of the absorption cross-section of the $C_2H_5O_2$ radical along with the rate constant and branching ratio of its self-reaction using a selective cw-CRDS detection of HO_2 and $C_2H_5O_2$ in the Ã-$\tilde{X}$ electronic transition located in the near-IR region. The $C_2H_5O_2$ absorption cross-section at the peak wavelength 7596.47 cm^{-1} has been determined by direct comparison with the well-known HO_2 absorption cross-section in back-to-back experiments to be $(1.0 \pm 0.2) \times 10^{-20}$ cm^2. This cross-section has also been validated by measuring the rate constant of $C_2H_5O_2$ with HO_2 in a wide range of concentrations: the ratio of $[HO_2]/[C_2H_5O_2]$ has been varied between 0.3 and 2.5 and the concentration time profiles for both radicals could be reproduced very well using the obtained absorption cross-section for $C_2H_5O_2$, which returned a rate constant for the cross reaction of $k_{20a} = 6.2 \times 10^{-12}$ $cm^3 molecule^{-1} s^{-1}$.

A strong disagreement exists about the rate constant and branching ratio of $C_2H_5O_2$ self-reaction between the IUPAC recommendation (Atkinson et al., 2006a), where a high C_2H_5O radical yield was generally admitted based on stable end products measurements, and a more recent work (Noell et al., 2010) where the radical channel was found to be the minor one based on selective detection of HO_2 and $C_2H_5O_2$ radicals. In this work we have also directly measured the radical yield and confirmed that it should be the minor one with r' = 0.31±0.06, together with a faster overall rate constant $k_{29} = (1.0 \pm 0.2) \times 10^{-13}$ $cm^3 molecule^{-1} s^{-1}$. This is therefore the second report of a low yield for the radical channel, based on direct measurement of radicals rather than end-products and this indicates that the current recommendation for the branching fraction and rate constant for this reaction should be revised.

Conclusions and Perspectives

In order to understand the complexity of chemical transformations and mechanisms occurring in the atmosphere, a contribution of new experimental kinetic data is required. As mentioned before, peroxy radicals are important intermediates in tropospheric chemical processes in both polluted and clean environments. While the influence of these peroxy radicals is well known in polluted environment where it leads to the formation of the tropospheric ozone, the reactivity of these radicals is still poorly known in clean environments where the RO_2 self- and cross-reactions become predominant and where RO_2 can also react with OH and HO_2 radicals.

This thesis was focused on the kinetic study of the reactions involving RO_2, HO_2 and OH radicals to better understand their reactivity in a low NOx environment. After a short overview on the radical chemistry in the troposphere highlighting the reactions involving peroxy radicals in clean environment, experimental techniques for carrying out kinetic studies for radical reactions were described briefly. In this work, two experimental set-ups have been used to study radical + radical reactions: a fast flow reactor that was continued to be developed in the frame of this work and which is designed to complement an existing photolysis cell set-up. The fast flow reactor is coupled to three complementary techniques: cw-CRDS, LIF and MB/MS and the laser photolysis cell is coupled to a double cw-CRDS paths for the simultaneous measurements of RO_2 and HO_2 radicals.

The fast flow reactor coupled to LIF, cw-CRDS, and MB/MS was developed during F. Kravtchenko's PhD (Kravtchenko, thesis 2019) and it was validated by the measurement of the rate constants of well-known reactions between OH radicals and stable species (propane, ethane, methanol). During the validation of this recently developed experimental set-up, an OH re-formation phenomenon disturbing the kinetic measurements has been observed. Following this work, different hypotheses were then explored during my thesis in order to further explain the OH re-formation phenomenon. Various tests showed that the problem is not due to heterogeneous reactions on the walls of the internal injector or the reactor. This has been shown by obtaining the same results when replacing the glass internal injector by a quartz one and using a glass reactor instead of a stainless steel one. Other tests showed also that the OH re-formation phenomenon is not due to the formation of F atoms in the external injector, neither to the formation of O atoms, nor to the formation of helium cations in the microwave discharge. This problem was not observed when OH was generated by the reaction of H + NO_2 which is the method mostly used in the

literature. However, this method of OH generation was not our first choice in this project since the final purpose is to study reactions between RO_2 and HOx in low NOx conditions. All attempts to avoid the OH re-formation phenomenon were unsuccessful so far. It would be interesting to measure the OH radical by mass spectrometry instead of LIF. Further tests that could be done is converting the OH into HOBr by adding Br_2 into the reactor and thus detecting HOBr by mass spectrometry as is done by Bedjanian et al. (Bedjanian et al., 1999). Other tests that could be done is coating the reactor by boric acid to check if the problem could come from an interaction with halocarbon wax.

Meanwhile a laser photolysis cell coupled to a double cw-CRDS paths for the simultaneous measurements of HO_2 and $C_2H_5O_2$ radicals was used to determine the rate constant and branching ratio of the $C_2H_5O_2$ self-reaction. The $C_2H_5O_2$ absorption cross-section at the peak wavelength 7596.47 cm^{-1} has been determined by direct comparison with the well-known HO_2 absorption cross-section in back-to-back experiments to be $(1.0 \pm 0.2) \times 10^{-20}$ cm^2. This cross-section has also been validated by measuring the rate constant of $C_2H_5O_2$ with HO_2 in a wide range of concentrations which returned a rate constant for the cross reaction of k_{20a} =6.2 × 10^{-12} $cm^3molecule^{-1}$ s^{-1}. A strong disagreement exists about the rate constant and branching ratio of $C_2H_5O_2$ self-reaction between the IUPAC recommendation (Atkinson et al., 2006a) where a high C_2H_5O radical yield was generally considered based on stable end products measurements and a more recent work (Noell et al., 2010) where the radical channel was found to be the minor one based on selective detection of HO_2 and $C_2H_5O_2$ radicals. In this work, the direct measurements of the radical yield confirmed that it should be the minor one with r' = 0.31±0.06, together with a faster overall rate constant $k_{29} = (1.0\pm0.2) \times 10^{-13}$ $cm^3molecule^{-1}s^{-1}$.

This approach focusing on the study of the complex atmospheric chemistry of radicals (RO_2 + HOx) in non-polluted environments is of great interest as it is not well-known in the literature. So, it would be interesting to study the kinetics of less known reactions such as $C_2H_5O_2$ + CH_3O_2 and $C_2H_5O_2$ + $CH_3C(O)O_2$ using the laser photolysis cell coupled to the double cw-CRDS paths.

References

Adachi, H., & Basco, N. (1979). Kinetic spectroscopy study of the reaction of CH_3O_2 with NO. *Chemical Physics Letters*, *64*, 431–434. https://doi.org/10.1016/0009-2614(79)80215-8

Amedro, D., Miyazaki, K., Parker, A., Schoemaecker, C., & Fittschen, C. (2012). Atmospheric and kinetic studies of OH and HO_2 by the FAGE technique. *Journal of Environmental Sciences*, *24*, 78–86. https://doi.org/10.1016/S1001-0742(11)60723-7

Anastasi, C., Waddington, D. J., & Woolley, A. J. (1983). Reactions of Oxygenated Radicals in the Gas Phase. *Journal of the Chemical Society, Faraday Transactions*, *79*, 505–516. https://doi.org/10.1039/F19837900505

Anderson, D. Z., Frisch, J. C., & Masser, C. S. (1984). Mirror reflectometer based on optical cavity decay time. *Applied Optics*, *23*, 1238. https://doi.org/10.1364/ao.23.001238

Appelman, E. H., & Clyne, M. A. A. (1975). Reaction Kinetics of Ground State Fluorine , F ^{2}P , Atoms. *Journal of the Chemical Society, Faraday Transactions 1*, *71*, 2072–2084. https://doi.org/10.1039/F19757102072

Archibald, A. T., Petit, A. S., Percival, C. J., Harvey, J. N., & Shallcross, D. E. (2009). On the importance of the reaction between OH and RO_2 radicals. *Atmospheric Science Letters*, *10*, 102–108. https://doi.org/10.1002/asl

Assaf, E., Asvany, O., Votava, O., Batut, S., Schoemaecker, C., & Fittschen, C. (2017a). Measurement of line strengths in the $\tilde{A}$ 2A' ← $\tilde{X}$ 2A" transition of HO_2 and DO_2. *Journal of Quantitative Spectroscopy and Radiative Transfer*, *201*, 161–170. https://doi.org/10.1016/j.jqsrt.2017.07.004

Assaf, E., Liu, L., Schoemaecker, C., & Fittschen, C. (2018c). Absorption spectrum and absorption cross sections of the $2\nu_1$ band of HO_2 between 20 and 760 Torr air in the range 6636 and 6639 cm^{-1}. *Journal of Quantitative Spectroscopy and Radiative Transfer*, *211*, 107–114. https://doi.org/10.1016/j.jqsrt.2018.02.035

Assaf, E., Schoemaecker, C., Vereecken, L., & Fittschen, C. (2018a). Experimental and theoretical investigation of the reaction of RO_2 radicals with OH radicals: Dependence of the HO_2 yield on the size of the alkyl group. *International Journal of Chemical Kinetics*, *50*, 670–680. https://doi.org/10.1002/kin.21191

Assaf, E., Schoemaecker, C., Vereecken, L., & Fittschen, C. (2018b). The reaction of fluorine atoms with methanol: Yield of CH_3O/CH_2OH and rate constant of the reactions $CH_3O + CH_3O$ and $CH_3O + HO_2$. *Physical Chemistry Chemical Physics*, *20*, 10660–10670. https://doi.org/10.1039/c7cp05770a

Assaf, E., Song, B., Tomas, A., Schoemaecker, C., & Fittschen, C. (2016). Rate Constant of the Reaction between CH_3O_2 Radicals and OH Radicals Revisited. *The Journal of Physical Chemistry A*, *120*, 8923–8932. https://doi.org/10.1021/acs.jpca.6b07704

Assaf, E., Tanaka, S., Kajii, Y., Schoemaecker, C., & Fittschen, C. (2017b). Rate constants of the reaction of C_2–C_4 peroxy radicals with OH radicals. *Chemical Physics Letters*, *684*, 245–249. https://doi.org/10.1016/j.cplett.2017.06.062

Assaf, E.(2017). *Kinetic study of reactions with interest to atmospheric chemistry by simultaneous detection of OH and RO_2 radicals coupled to laser photolysis*. PhD thesis.

Assali, M., & Fittschen, C. (2022). Rate Constants and Branching Ratios for the Self-Reaction of Acetyl Peroxy ($CH_3C(O)O_2$•) and Its Reaction with CH_3O_2. *Atmosphere*, *13*, 186. https://doi.org/10.3390/atmos13020186

Assali, M., Rakovsky, J., Votava, O., & Fittschen, C. (2019). Experimental determination of the rate constants of the reactions of HO_2 + DO_2 and DO_2 + DO_2. *International Journal of Chemical Kinetics*, *52*, 197–206. https://doi.org/10.1002/kin.21342

Atkinson, D. B., & Hudgens, J. W. (1997). Chemical Kinetic Studies Using Ultraviolet Cavity Ring-Down Spectroscopic Detection : Self-Reaction of Ethyl and Ethylperoxy Radicals and the Reaction O_2 + C_2H_5 → $C_2H_5O_2$. *Journal of Physical Chemistry A*, *101*, 3901–3909. https://doi.org/10.1021/jp970240+

Atkinson, D. B., & Spillman, J. L. (2002). Alkyl peroxy radical kinetics measured using near-infrared CW-cavity ring-down spectroscopy. *Journal of Physical Chemistry A*, *106*, 8891–8902. https://doi.org/10.1021/jp0257597

Atkinson, R., Baulch, D. L., Cox, R. A., Crowley, J. N., Hampson, R. F., Hynes, R. G., Jenkin, M. E., Rossi, M. J., & Troe, J. (2004). Evaluated kinetic and photochemical data for atmospheric chemistry: Volume I - gas phase reactions of Ox, HOx, NOx and SOx species. *Atmospheric Chemistry and Physics*, *4*, 1461–1738. https://doi.org/10.5194/acp-4-1461-2004

Atkinson, R., Baulch, D. L., Cox, R. A., Crowley, J. N., Hampson, R. F., Hynes, R. G., Jenkin, M. E., Rossi, M. J., & Troe, J. (2006a). Evaluated kinetic and photochemical data for atmospheric chemistry: Volume II – gas phase reactions of organic species. *Atmospheric Chemistry and Physics*, *6*, 3625–4055. https://doi.org/10.5194/acp-6-3625-2006

Atkinson, R., Baulch, D. L., Cox, R. A., Crowley, J. N., Hampson, R. F., Hynes, R. G., Jenkin, M. E., Rossi, M. J., & Troe, J. (2006b). Evaluated kinetic and photochemical data for atmospheric chemistry: Volume III - Gas phase reactions of inorganic halogens. *Atmospheric Chemistry and Physics Discussions*, *6*, 2281–2702.

Bauer, D., Crowley, J. N., & Moortgat, G. K. (1992). The UV absorption spectrum of the ethylperoxy radical and its self-reaction kinetics between 218 and 333 K. *Journal of Photochemistry and Photobiology, A: Chemistry*, *65*, 329–344. https://doi.org/10.1016/1010-6030(92)80015-N

Baulch, D. L., Campbell, I. M., & Saunders, S. M. (1985). Rate constants for the reactions of hydroxyl radicals with propane and ethane. *J. Chem. Soc. Faraday Trans. 1*, *81*, 259–263. https://doi.org/10.1126/science.180.4087.735

Bedjanian, Y., Le Bras, G., & Poulet, G. (1999). Kinetic Study of OH + OH and OD + OD Reactions. *Journal of Physical Chemistry A*, *103*, 7017–7025. https://doi.org/10.1021/jp991146r

Bedjanian, Y., Romanias, M. N., & El Zein, A. (2013). Uptake of HO_2 radicals on Arizona Test Dust. *Atmospheric Chemistry and Physics*, *13*, 6461–6471. https://doi.org/10.5194/acp-13-6461-2013

Bedjanian, Yuri, Riffault, V., Bras, G. Le, & Poulet, G. (2001). Kinetic study of the reactions of Br with HO_2 and DO_2. *Journal of Physical Chemistry A*, *105*, 573–578. https://doi.org/10.1021/jp002731r

Berndt, T., Chen, J., Kjærgaard, E. R., Møller, K. H., Tilgner, A., Hoffmann, E. H., Herrmann, H., Crounse, J. D., Wennberg, P. O., & Kjaergaard, H. G. (2022). Hydrotrioxide (ROOOH) formation in the atmosphere. *Science*, *376*, 979–982. https://doi.org/10.1126/science.abn6012

Bossolasco, A., Faragó, E. P., Schoemaecker, C., & Fittschen, C. (2014). Rate constant of the reaction between CH_3O_2 and OH radicals. *Chemical Physics Letters*, *593*, 7–13. https://doi.org/10.1016/j.cplett.2013.12.052

Boyd, A. A., Flaud, P. M., Daugey, N., & Lesclaux, R. (2003). Rate constants for RO_2 + HO_2 reactions measured under a large excess of HO_2. *Journal of Physical Chemistry A*, *107*, 818–821. https://doi.org/10.1021/jp026581r

Bridier, I., Veyret, B., Lesclaux, R., & Jenkin, M. E. (1993). Flash photolysis study of the UV spectrum and kinetics of reactions of the acetonylperoxy radical. *Journal of the Chemical Society, Faraday Transactions*, *89*, 2993–2997. https://doi.org/10.1039/FT9938902993

Caravan, R. L., Khan, M. A. H., Zádor, J., Sheps, L., Antonov, I. O., Rotavera, B., Ramasesha, K., Au, K., Chen, M. W., Rösch, D., Osborn, D. L., Fittschen, C., Schoemaecker, C., Duncianu, M., Grira, A., Dusanter, S., Tomas, A., Percival, C. J., Shallcross, D. E., & Taatjes, C. A. (2018). The reaction of hydroxyl and methylperoxy radicals is not a major source of atmospheric methanol. *Nature Communications*, *9*, 4343. https://doi.org/10.1038/s41467-018-06716-x

Cattell, F. C., Cavanagh, J., Cox, R. A., & Jenkin, M. E. (1986). A kinetics study of reactions of HO_2 and $C_2H_5O_2$ using diode laser absorption spectroscopy. *Journal of the Chemical Society, Faraday Transactions 2: Molecular and Chemical Physics*, *82*, 1999–2018. https://doi.org/10.1039/F29868201999

Chao, W., Jr-min, J., Takahashi, K., Tomas, A., Yu, L., Kajii, Y., Batut, S., Schoemaecker, C., & Fittschen, C. (2019). Water Vapor Does Not Catalyze the Reaction between Methanol and OH Radicals. *Angew. Chem.*, *131*, 5067–5071. https://doi.org/10.1002/ange.201900711

Chen, L., Kutsuna, S., Tokuhashi, K., & Sekiya, A. (2003). New technique for generating high concentrations of gaseous OH radicals in relative rate measurements. *International Journal of Chemical Kinetics*, *35*, 317–325. https://doi.org/10.1002/kin.10133

Chuong, B., & Stevens, P. S. (2003). Kinetics of the OH + methyl vinyl ketone and OH + methacrolein reactions at low pressure. *Journal of Physical Chemistry A*, *107*, 2185–2191. https://doi.org/10.1021/jp026036q

Clifford, E. P., Farrell, J. T., DeSain, J. D., & Taatjes, C. A. (2000). Infrared Frequency-Modulation Probing of Product Formation in Alkyl + O_2 Reactions: I. the Reaction of C_2H_5 with O_2 between 295 and 698 K. *Journal of Physical Chemistry A*, *104*, 11549–11560. https://doi.org/10.1021/jp0024874

Cox, R. A., & Tyndall, G. S. (1980). Rate Constants for the Reactions of CH_3O_2 with HO_2, NO and NO_2 using Molecular Modulation Spectrometry. *Journal of the Chemical Society,*

Faraday Transactions 2: Molecular and Chemical Physics, *76*, 153–163. https://doi.org/10.1039/F29807600153

Crawford, M. A., Wallington, T. J., Szente, J. J., Maricq, M. M., & Francisco, J. S. (1999). Kinetics and Mechanism of the Acetylperoxy + HO_2 Reaction. *Journal of Physical Chemistry A*, *103*, 365–378. https://doi.org/10.1021/jp983150t

Dagaut, P., Wallington, T. J., & Kurylo, M. J. (1988b). Flash photolysis kinetic absorption spectroscopy study of the gas-phase reaction HO_2 + $C_2H_5O_2$ over the temperature range 228-380 K. *Journal of Physical Chemistry*, *92*, 3836–3839. https://doi.org/10.1021/j100324a031

Dagaut, P., Wallington, T. J., & Kurylo, M. J. (1988a). Temperature dependence of the rate constant for the HO_2 + CH_3O_2 gas-phase reaction. *J. Phys. Chem.*, *92*, 3833–3836. https://doi.org/10.1021/j100324a030

DeSain, J. D., Ho, A. D., & Taatjes, C. A. (2003). High-resolution diode laser absorption spectroscopy of the O-H stretch overtone band (2, 0, 0) ← (0, 0, 0) of the HO_2 radical. *Journal of Molecular Spectroscopy*, *219*, 163–169. https://doi.org/10.1016/S0022-2852(03)00022-5

Dillon, T. J., & Crowley, J. N. (2008). Direct detection of OH formation in the reactions of HO_2 with $CH_3C(O)O_2$ and other substituted peroxy radicals. *Atmospheric Chemistry and Physics*, *8*, 4877–4889. https://doi.org/10.5194/acp-8-4877-2008

Djehiche, M., Tomas, A., Fittschen, C., & Coddeville, P. (2011). First cavity ring-down spectroscopy HO_2 measurements in a large photoreactor. *Zeitschrift Fur Physikalische Chemie*, *225*, 983–992. https://doi.org/10.1524/zpch.2011.0143

Doussin, J. F., Ritz, D., Durand-Jolibois, R., Monod, A., & Carlier, P. (1997). Design of an environmental chamber for the study of atmospheric chemistry: New developments in the analytical device. In *Analusis* (Vol. 25, pp. 236–242). https://doi.org/10.1016/S0365-4877(97)86083-4

Dransfield, T. J., Perkins, K. K., Donahue, N. M., Anderson, J. G., Sprengnether, M. M., & Demerjian, K. L. (1999). Temperature and pressure dependent kinetics of the gas-phase reaction of the hydroxyl radical with nitrogen dioxide. *Geophysical Research Letters*, *26*, 687–690. https://doi.org/10.1029/1999GL900028

Faragó, E. P., Schoemaecker, C., Viskolcz, B., & Fittschen, C. (2015). Experimental determination of the rate constant of the reaction between $C_2H_5O_2$ and OH radicals. *Chemical Physics Letters*, *619*, 196–200. https://doi.org/10.1016/j.cplett.2014.11.069

Farago, E. P., Viskolcz, B., Schoemaecker, C., & Fittschen, C. (2013). Absorption Spectrum and Absolute Absorption Cross Sections of CH_3O_2 Radicals and CH_3I Molecules in the Wavelength Range 7473− 7497 cm−1. *Journal of Physical Chemistry A*, *117*, 12802–12811. https://doi.org/10.1021/jp408686s

Fayad, L. (2019). *Characterization of the new atmospheric simulation chamber CHARME , and study of the ozonolysis reaction of a biogenic VOC , the γ -terpinene*. PhD thesis.

Fenter, F. F., Catoire, V., Lesclaux, R., & Lightfoot, P. D. (1993). The ethylperoxy radical: Its ultraviolet spectrum, self-reaction, and reaction with HO_2, each studied as a function of temperature. *Journal of Physical Chemistry*, *97*, 3530–3538.

https://doi.org/10.1021/j100116a016

Fernandes, R. X., Luther, K., Marowsky, G., Rissanen, M. P., Timonen, R., & Troe, J. (2015). Experimental and Modeling Study of the Temperature and Pressure Dependence of the Reaction $C_2H_5 + O_2$ (+ M) → $C_2H_5O_2$ (+ M). *Journal of Physical Chemistry A*, *119*, 7263–7269. https://doi.org/10.1021/jp511672v

Fittschen, C., Frenzel, A., Imrik, K., Devolder, P., & Cine, L. De. (1999). Rate Constants for the Reactions of C_2H_5O , i-C_3H_7O , and n-C_3H_7O with NO and O_2 as a Function of Temperature. *John Wiley & Sons*, *31*, 860–866. https://doi.org/10.1002/(SICI)1097-4601(1999)31:12<860::AID-KIN4>3.0.CO;2-E

Fittschen, C. (2019). The reaction of peroxy radicals with OH radicals. *Chemical Physics Letters*, *725*, 102–108. https://doi.org/10.1016/j.cplett.2019.04.002

Fittschen, Christa, Whalley, L. K., & Heard, D. E. (2014). The Reaction of CH_3O_2 Radicals with OH Radicals: A Neglected Sink for CH_3O_2 in the Remote Atmosphere. *Environmental Science & Technology*, *48*, 7700–7701. https://doi.org/10.1021/es502481q

Glowacki, D. R., Goddard, A., Hemavibool, K., Malkin, T. L., Commane, R., Anderson, F., Bloss, W. J., Heard, D. E., Ingham, T., Pilling, M. J., & Seakins, P. W. (2007). Design of and initial results from a Highly Instrumented Reactor for Atmospheric Chemistry (HIRAC). *Atmospheric Chemistry and Physics*, *7*, 5371–5390. https://doi.org/10.5194/acp-7-5371-2007

Groß, C. B. M., Dillon, T. J., Schuster, G., Lelieveld, J., & Crowley, J. N. (2014). Direct kinetic study of OH and O_3 formation in the reaction of $CH_3C(O)O_2$ with HO_2. *Journal of Physical Chemistry A*, *118*, 974–985. https://doi.org/10.1021/jp412380z

Hansen, N., Cool, T. A., Westmoreland, P. R., & Kohse-Höinghaus, K. (2009). Recent contributions of flame-sampling molecular-beam mass spectrometry to a fundamental understanding of combustion chemistry. *Progress in Energy and Combustion Science*, *35*, 168–191. https://doi.org/10.1016/j.pecs.2008.10.001

Hasson, A. S., Tyndall, G. S., & Orlando, J. J. (2004). A product yield study of the reaction of HO_2 radicals with ethyl peroxy ($C_2H_5O_2$), acetyl peroxy ($CH_3C(O)O_2$), and acetonyl peroxy ($CH_3C(O)CH_2O_2$) radicals. *Journal of Physical Chemistry A*, *108*, 5979–5989. https://doi.org/10.1021/jp048873t

Hasson, A. S., Tyndall, G. S., Orlando, J. J., Singh, S., Hernandez, S. Q., Campbell, S., & Ibarra, Y. (2012). Branching ratios for the reaction of selected carbonyl-containing peroxy radicals with hydroperoxy radicals. *Journal of Physical Chemistry A*, *116*, 6264–6281. https://doi.org/10.1021/jp211799c

Heard, D. E., & Pilling, M. J. (2003). The measurement of OH and HO_2 in the troposphere. *Chemical Reviews*, *103*, 5136–5198. https://doi.org/10.1021/cr020522s

Horie, O., & Moortgat, G. K. (1992). Reactions of $CH_3C(O)O_2$ radicals with CH_3O_2 and HO_2 between 263 and 333 K. *Journal of the Chemical Society, Faraday Transactions*, *88*, 3305–3312. https://doi.org/10.1039/FT9928803305

Hou, H., Li, J., Song, X., & Wang, B. (2005). A Systematic Computational Study on the Reactions of HO_2 with RO_2: The $HO_2 + C_2H_5O_2$ Reaction. *Journal of Physical Chemistry A*, *109*, 11206–

11212. https://doi.org/10.1021/jp0550098

Howard, C. J. (1979). Kinetic measurements using flow tubes. *Journal of Physical Chemistry*, *83*, 3–9. https://doi.org/10.1021/j100464a001

Howard, C. J., & Evenson, K. M. (1974). Laser magnetic resonance study of the gas phase reactions of OH with CO, NO, and NO_2. *The Journal of Chemical Physics*, *61*, 1943–1952. https://doi.org/10.1063/1.1682195

Hui, A. O., Fradet, M., Okumura, M., & Sander, S. P. (2019). Temperature Dependence Study of the Kinetics and Product Yields of the HO_2 + $CH_3C(O)O_2$ Reaction by Direct Detection of OH and HO_2 Radicals Using 2f-IR Wavelength Modulation Spectroscopy. *The Journal of Physical Chemistry A*, *123*, 3655–3671. https://doi.org/10.1021/acs.jpca.9b00442

Hunziker, H. E., & Wendt, H. R. (1974). Near infrared absorption spectrum of HO_2. *The Journal of Chemical Physics*, *60*, 4622–4623. https://doi.org/10.1063/1.1680949

Hunziker, H. E., & Wendt, H. R. (1976). Electronic absorption spectra of organic peroxyl radicals in the near infrared. *The Journal of Chemical Physics*, *64*, 3488–3490. https://doi.org/10.1063/1.432606

Ibrahim, N., Thiebaud, J., Orphal, J., & Fittschen, C. (2007). Air-broadening coefficients of the HO_2 radical in the $2\nu_1$ band measured using cw-CRDS. *Journal of Molecular Spectroscopy*, *242*, 64–69. https://doi.org/10.1016/j.jms.2007.02.007

J. M. Herbelin, J. A. McKay, M. A. Kwok, R. H. Ueunten, D. S. Urevig, D. J. Spencer, and D. J. B. (1980). Sensitive Measurement of Photon Lifetime and True Reflectances in an Optical Cavity by a Phase Shift Method. *Applied Optics*, *19*, 144–147. https://doi.org/10.1364/AO.19.000144

Jenkin, M. E., Hurley, M. D., & Wallington, T. J. (2007). Investigation of the radical product channel of the $CH_3C(O)O_2$ + HO_2 reaction in the gas phase. *Physical Chemistry Chemical Physics*, *9*, 3149–3162. https://doi.org/10.1039/b702757e

Jenkin, M. E., Hurley, M. D., & Wallington, T. J. (2008). Investigation of the radical product channel of the $CH_3C(O)CH_2O_2$ + HO_2 reaction in the gas phase. *Physical Chemistry Chemical Physics*, *10*, 4274–4280. https://doi.org/10.1039/b802898b

Jenkin, Michael E., Valorso, R., Aumont, B., & Rickard, A. R. (2019). Estimation of rate coefficients and branching ratios for reactions of organic peroxy radicals for use in automated mechanism construction. *Atmospheric Chemistry and Physics*, *19*, 7691–7717. https://doi.org/10.5194/acp-19-7691-2019

Johnson, D., Price, D. W., & Marston, G. (2004). Correlation-type structure activity relationships for the kinetics of gas-phase RO_2 self-reactions and reaction with HO_2. *Atmospheric Environment*, *38*, 1447–1458. https://doi.org/10.1016/j.atmosenv.2003.12.003

Kambezidis, H. D. (2012). *"3.02–The Solar Resource."Comprehensive Renewable Energy* (Vol. 3). Elsevier Oxford. https://doi.org/10.1016/B978-0-08-087872-0.00302-4

Keil, D. G., Tanzawa, T., Skolnik, E. G., Bruce Klemm, R., & Michael, J. V. (1981). Rate constants for the reaction of ground state atomic oxygen with methanol. *The Journal of Chemical*

Physics, *75*, 2693–2704. https://doi.org/10.1063/1.442379

Kravtchenko, F. (2019). *Développement et validation d'un nouveau dispositif expérimental pour l'étude des réactions RO_2 + HOx*. PhD thesis.

Langhaar, H. L. (1942). Steady Flow in the Transition Length of a Straight Tube. *J. Appl . Mech*, *9*.

Le Crâne, J. P., Rayez, M. T., Rayez, J. C., & Villenave, E. (2006). A reinvestigation of the kinetics and the mechanism of the $CH_3C(O)O_2$ + HO_2 reaction using both experimental and theoretical approaches. *Physical Chemistry Chemical Physics*, *8*, 2163–2171. https://doi.org/10.1039/b518321a

Lehmann. (1996). *Ring-Down Cavity Spectroscopy Cell Using Continious Wave Excitation For Trace Species Detection*. *19*.

Lightfoot, P. D., Lesclaux, R., & Veyret, B. (1990). Flash photolysis study of the CH_3O_2 + CH_3O_2 reaction: Rate constants and branching ratios from 248 to 573 K. *Journal of Physical Chemistry*, *94*, 700–707. https://doi.org/10.1021/j100365a035

Liu, Y., Chen, L., Chen, D., Wang, W., Liu, F., & Wang, W. (2017). Computational study on mechanisms of $C_2H_5O_2$+OH reaction and properties of $C_2H_5O_3H$ complex. *Chemical Research in Chinese Universities*, *33*, 623–630. https://doi.org/10.1007/s40242-017-7055-4

Malkin, T. L., Goddard, A., Heard, D. E., & Seakins, P. W. (2010). Measurements of OH and HO_2 yields from the gas phase ozonolysis of isoprene. *Atmospheric Chemistry and Physics*, *10*, 1441–1459. https://doi.org/10.5194/acp-10-1441-2010

Maricq, M. M., & Szente, J. J. (1994). A kinetic study of the reaction between ethylperoxy radicals and HO_2. *Journal of Physical Chemistry*, *98*, 2078–2082. https://doi.org/10.1021/j100059a016

Maricq, M. M., & Szente, J. J. (1996). The Acetylperoxy Radical: Its UV Spectrum, Self-Reaction Kinetics, and Reaction with Methylperoxy Radical. *J. Phys. Chem.*, *100*, 4507–4513. https://doi.org/10.1021/jp9533234

Maricq, M. M., Szente, J. J., Kaiser, E. W., & Shi, J. (1994). Reaction of chlorine atoms with methylperoxy and ethylperoxy radicals. *Journal of Physical Chemistry*, *98*, 2083–2089. https://doi.org/10.1021/j100059a017

McCaulley, J., N, K., MF, G., & F, K. (1989). Kinetics Studies of the Reactions of F and OH with CH_3OH. *Journal of Physical Chemistry*, *93*, 1014–1018. https://doi.org/10.1021/j100340a002

Meier, U., Grotheer, H. H., & Just, T. (1984). Temperature dependence and branching ratio of the CH_3OH+OH reaction. *Chemical Physics Letters*, *106*, 97–101. https://doi.org/10.1016/0009-2614(85)80684-9

Melnik, D., Chhantyal-Pun, R., & Miller, T. A. (2010). Measurements of the absolute absorption cross sections of the $\tilde{A} \leftarrow \tilde{X}$ Transition in organic peroxy radicals by dual-wavelength cavity ring-down spectroscopy. *Journal of Physical Chemistry A*, *114*, 11583–11594. https://doi.org/10.1021/jp107340a

Melnik, D., & Miller, T. A. (2013). Kinetic measurements of the $C_2H_5O_2$ radical using time-

resolved cavity ring-down spectroscopy with a continuous source. *Journal of Chemical Physics*, *139*, 094201. https://doi.org/10.1063/1.4819474

Moortgat, G. K., Veyret, B., & Lesclaux, R. (1989). Kinetics of the reaction of HO_2 with $CH_3C(O)O_2$ in the temperature range 253-368 K. *Chemical Physics Letters*, *160*, 443–447. https://doi.org/10.1016/0009-2614(89)87624-9

Morin, J., Bedjanian, Y., & Kalyan, C. (2017). Rate constants of the reactions of $O(^3P)$ atoms with Br_2 and NO_2 over the temperature range 220-950 K. *International Journal of Chemical Kinetics*, *51*, 476–483. https://doi.org/10.1002/kin.21270

Müller, J. F., Liu, Z., Nguyen, V. S., Stavrakou, T., Harvey, J. N., & Peeters, J. (2016). The reaction of methyl peroxy and hydroxyl radicals as a major source of atmospheric methanol. *Nature Communications*, *7*. https://doi.org/10.1038/ncomms13213

Munk, J., Pagsberg, P., Ratajczak, E., & Sillesen, A. (1986). Spectrokinetic studies of ethyl and ethylperoxy radicals. *American Chemical Society*, *90*, 2752–2757. https://doi.org/10.1021/j100403a038

Nielsen, O. J., Johnson, M. S., Wallington, T. J., Christensen, L. K., & Platz, J. (2002). UV absorption spectra of HO_2, CH_3O_2, $C_2H_5O_2$, and $CH_3C(O)CH_2O_2$ radicals and mechanism of the reactions of F and Cl atoms with $CH_3C(O)CH_3$. *International Journal of Chemical Kinetics*, *34*, 283–291. https://doi.org/10.1002/kin.10037

Niki, H., Maker, P. D., Savage, C. M., & Breitenbach, L. P. (1982). Fourier Transform Infrared Studies of the Self-Reaction of $C_2H_5O_2$ Radicals. *J. Phys. Chem.*, *86*, 3825–3829. https://doi.org/10.1021/j100216a023

Niki, H., Maker, P. D., Savage, C. M., & Breitenbach, L. P. (1985). FTIR study of the kinetics and mechanism for Cl-atom-initiated reactions of acetaldehyde. *Journal of Physical Chemistry*, *89*, 588–591. https://doi.org/10.1021/j100250a008

Noell, A. C., Alconcel, L. S., Robichaud, D. J., Okumura, M., & Sander, S. P. (2010). Near-Infrared Kinetic Spectroscopy of the HO_2 and $C_2H_5O_2$ Self-Reactions and Cross Reactions. *Journal of Physical Chemistry A*, *114*, 6983–6995. https://doi.org/10.1021/jp912129j

O'Keefe, A., & Deacon, D. A. G. (1988). Cavity ring-down optical spectrometer for absorption measurements using pulsed laser sources. *Review of Scientific Instruments*, *59*, 2544–2551. https://doi.org/10.1063/1.1139895

Onel, L., Brennan, A., Gianella, M., Hooper, J., Ng, N., Hancock, G., Whalley, L., Seakins, P. W., Ritchie, G. A. D., & Heard, D. E. (2017). An intercomparison of CH_3O_2 measurements by fluorescence assay by gas expansion and cavity ring-down spectroscopy within HIRAC (Highly Instrumented Reactor for Atmospheric Chemistry). *Atmospheric Measurement Techniques*, *10*, 4877–4894. https://doi.org/10.5194/amt-10-4877-2017

Orlando, J. J., & Tyndall, G. S. (2012). Laboratory studies of organic peroxy radical cemistry: an overview with emphasis on recent issues of atmospheric significance. *Chemical Society Reviews*, *41*, 6294–6317. https://doi.org/10.1039/C2CS35166H

Orlando, J. J., Tyndall, G. S., Vereecken, L., & Peeters, J. (2000). The Atmospheric Chemistry of the Acetonoxy Radical. *Journal of Physical Chemistry A*, *104*, 11578–11588.

https://doi.org/10.1021/jp0026991

Parker, A. E., Jain, C., Schoemaecker, C., Szriftgiser, P., Votava, O., & Fittschen, C. (2011). Simultaneous, time-resolved measurements of OH and HO_2 radicals by coupling of high repetition rate LIF and cw-CRDS techniques to a laser photolysis reactor and its application to the photolysis of H_2O_2. *Applied Physics B: Lasers and Optics*, *103*, 725–733. https://doi.org/10.1007/s00340-010-4225-1

Pushkarsky, M. B., Zalyubovsky, S. J., & Miller, T. A. (2000). Detection and characterization of alkyl peroxy radicals using cavity ringdown spectroscopy. *Journal of Chemical Physics*, *112*, 10695–10698. https://doi.org/10.1063/1.481705

Raventós-Duran, M. T., McGillen, M., Percival, C. J., Hamer, P. D., & Shallcross, D. E. (2007a). Kinetics of the CH_3O_2 + HO_2 Reaction: A Temperature and Pressure Dependence Study Using Chemical Ionization Mass Spectrometry. *International Journal of Chemical Kinetics*, *39*, 571–579. https://doi.org/10.1002/kin

Raventós-Duran, M. T., Percival, C. J., McGillen, M. R., Hamer, P. D., & Shallcross, D. E. (2007b). Kinetics and branching ratio studies of the reaction of $C_2H_5O_2$ + HO_2 using chemical ionisation mass spectrometry. *Physical Chemistry Chemical Physics*, *9*, 4338–4348. https://doi.org/10.1039/B703038J

Ren, Y., Grosselin, B., Daële, V., & Mellouki, A. (2017). Investigation of the reaction of ozone with isoprene, methacrolein and methyl vinyl ketone using the HELIOS chamber. *Faraday Discussions*, *200*, 289–311. https://doi.org/10.1039/c7fd00014f

Ridenti, M. A., De Amorim, J., & Dal Pino, A. (2015). Equilibrium and Nonequilibrium Features in a Warm He+H_2O Microwave Plasma at Atmospheric Pressure. *IEEE Transactions on Plasma Science*, *43*, 4066–4076. https://doi.org/10.1109/TPS.2015.2496870

Rohrer, F., Bohn, B., Brauers, T., Brüning, D., Johnen, F. J., Wahner, A., & Kleffmann, J. (2005). Characterisation of the photolytic HONO-source in the atmosphere simulation chamber SAPHIR. *Atmospheric Chemistry and Physics*, *5*, 2189–2201. https://doi.org/10.5194/acp-5-2189-2005

Romanini, D., Kachanov, A. A., Sadeghi, N., & Stoeckel, F. (1997). CW cavity ring down spectroscopy. *Chemical Physics Letters*, *264*, 316–322. https://doi.org/10.1016/S0009-2614(96)01351-6

Rupper, P., Sharp, E. N., Tarczay, G., & Miller, T. A. (2007). Investigation of ethyl peroxy radical conformers via cavity ringdown spectroscopy of the Ã-X̃ electronic transition. *Journal of Physical Chemistry A*, *111*, 832–840. https://doi.org/10.1021/jp066464m

Seakins, P. W., Woodbridge, E. L., & Leone, S. R. (1993). A laser flash photolysis, time-resolved fourier transform infrared emission study of the reaction Cl + C_2H_5 → HCl(v) + C_2H_4. *Journal of Physical Chemistry*, *97*, 5633–5642. https://doi.org/10.1021/j100123a029

Seinfeld, J. H., & Pandis, S. N. (2016). Atmospheric Chemistry and Physics: From Air Pollution to Climate Change. *John Wiley & Sons*.

Showman, A. P., & Dowling, T. E. (2014). Chapter 20-Earth as a Planet: Atmosphere and Oceans. In *Encyclopedia of the Solar System* (Third Edit). Elsevier Inc. https://doi.org/10.1016/b978-

0-12-415845-0.00020-7

Slade, J. H., & Knopf, D. A. (2013). Heterogeneous OH oxidation of biomass burning organic aerosol surrogate compounds: Assessment of volatilisation products and the role of OH concentration on the reactive uptake kinetics. *Physical Chemistry Chemical Physics*, *15*, 5898–5915. https://doi.org/10.1039/c3cp44695f

So, P. T., & Dong, C. Y. (2001). Fluorescence Spectrophotometry. *Methods of Air Sampling and Analysis*, 187–190. https://doi.org/10.1038/npg.els.0002978

Spittler, M., Barnes, I., Becker, K. H., & Wallington, T. J. (2000). Product study of the $C_2H_5O_2$ + HO reaction in 760 Torr of air at 284–312 K. *Chemical Physics Letters*, *321*, 57–61. https://doi.org/10.1016/S0009-2614(00)00315-8

Stevens, P. S., Brune, W. H., & Anderson, J. G. (1989). Kinetic and mechanistic investigations of F + H_2O/D_2O and F + H_2/D_2 over the temperature range 240-373 K. *J. Phys. Chem.*, *93*, 4068–4079. https://doi.org/10.1021/j100347a040

Su, M. C., Kumaran, S. S., Lim, K. P., Michael, J. V., Wagner, A. F., Harding, L. B., & Fang, D. C. (2002). Rate constants, $1100 \leq T \leq 2000$ K, for H + NO_2 → OH + NO using two shock tube techniques: Comparison of theory to experiment. *Journal of Physical Chemistry A*, *106*, 8261–8270. https://doi.org/10.1021/jp0141023

Tang, Y., Tyndall, G. S., & Orlando, J. J. (2010). Spectroscopic and kinetic properties of HO_2 radicals and the enhancement of the HO_2 Self reaction by CH_3OH and H_2O. *Journal of Physical Chemistry A*, *114*, 369–378. https://doi.org/10.1021/jp905279b

Thiebaud, J., Crunaire, S., & Fittschen, C. (2007). Measurements of line strengths in the $2v_1$ band of the HO_2 radical using laser photolysis/Continuous Wave Cavity Ring-Down Spectroscopy (cw-CRDS). *Journal of Physical Chemistry A*, *111*, 6959–6966. https://doi.org/10.1021/jp0703307

Thiébaud, J., & Fittschen, C. (2006). Near infrared cw-CRDS coupled to laser photolysis: Spectroscopy and kinetics of the HO_2 radical. *Applied Physics B: Lasers and Optics*, *85*, 383–389. https://doi.org/10.1007/s00340-006-2304-0

Thüner, L. P., Bardini, P., Rea, G. J., & Wenger, J. C. (2004). Kinetics of the gas-phase reactions of OH and NO_3 radicals with aromatic aldehydes. *Journal of Photochemistry and Photobiology A: Chemistry*, *108*, 11019–11025. https://doi.org/10.1021/jp046358p

Tsang, W. (1988). Chemical Kinetic Data Base for Combustion Chemistry. Part 3. Propane. *Journal of Physical and Chemical Reference Data*, *17*, 887. https://doi.org/10.1063/1.555806

Tuazon, E. C., & Atkinson, R. (1989). A product study of the gas-phase reaction of methyl vinyl ketone with the OH radical in the presence of NOx. *International Journal of Chemical Kinetics*, *21*, 1141–1152. https://doi.org/10.1002/kin.550211207

Villenave, E., & Lesclaux, R. (1996). Kinetics of the cross reactions of CH_3O_2 and $C_2H_5O_2$ radicals with selected peroxy radicals. *Journal of Physical Chemistry*, *100*, 14372–14382. https://doi.org/10.1021/jp960765m

Votava, O., Mašát, M., Parker, A. E., Jain, C., & Fittschen, C. (2012). Microcontroller based

resonance tracking unit for time resolved continuous wave cavity-ringdown spectroscopy measurements. In *Review of Scientific Instruments* (Vol. 83, p. 043110). https://doi.org/10.1063/1.3698061

Wallington, T. J., Dagaut, P., & Kurylo, M. J. (1988). Measurements of the gas phase UV absorption spectrum of $C_2H_5O_2$· radicals and of the temperature dependence of the rate constant for their self-reaction. *Journal of Photochemistry and Photobiology, A: Chemistry*, *42*, 173–185. https://doi.org/10.1016/1010-6030(88)80061-3

Wallington, T. J., Dagaut, P., & Kurylo, M. J. (1992). Ultraviolet Absorption Cross Sections and Reaction Kinetics and Mechanisms for Peroxy Radicals in the Gas Phase. *Chemical Reviews*, *92*, 667–710. https://doi.org/10.1021/cr00012a008

Wallington, T. J., Gierczak, C. A., Ball, J. C., & Japar, S. M. (1989). Fourier transform infrared study of the self reaction of $C_2H_5O_2$ radicals in air at 295 K. *International Journal of Chemical Kinetics*, *21*, 1077–1089. https://doi.org/10.1002/kin.550211109

Wallington, T. J., & Japar, S. M. (1990b). FTIR product study of the reaction of $C_2H_5O_2 + HO_2$ in air at 295 K. *Chemical Physics Letters*, *166*, 495–499. https://doi.org/10.1016/0009-2614(90)87140-M

Wallington, T. J., & Japar, S. M. (1990a). Reaction of $CH_3O_2 + HO_2$ at 295 K: A product study. *Chemical Physics Letters*, *167*, 513–518. https://doi.org/10.1016/0009- 2614(90)85461-K

Wen, Z., Tang, X., Fittschen, C., Zhang, C., Wang, T., Wang, C., Gu, X., & Zhang, W. (2020). Online analysis of gas-phase radical reactions using vacuum ultraviolet lamp photoionization and time-of-flight mass spectrometry. *Review of Scientific Instruments*, *91*, 043201. https://doi.org/10.1063/1.5135387

Wen, Z., Tang, X., Wang, C., Fittschen, C., Wang, T., Zhang, C., Yang, J., Pan, Y., Liu, F., & Zhang, W. (2019). A vacuum ultraviolet photoionization time-of-flight mass spectrometer with high sensitivity for study of gas-phase radical reaction in a flow tube. *International Journal of Chemical Kinetics*, *51*, 178–188. https://doi.org/10.1002/kin.21241

Wennberg, P. O. (2013). Let's abandon the "High NOx" and " low NO x " terminology. *IGACnews*, *50*, 3–4.

Whalley, L. K., Edwards, P. M., Furneaux, K. L., Goddard, A., Ingham, T., Evans, M. J., Stone, D., Hopkins, J. R., Jones, C. E., Karunaharan, A., Lee, J. D., Lewis, A. C., Monks, P. S., Moller, S. J., & Heard, D. E. (2011). Quantifying the magnitude of a missing hydroxyl radical source in a tropical rainforest. *Atmospheric Chemistry and Physics*, *11*, 7223–7233. https://doi.org/10.5194/acp-11-7223-2011

Whalley, L. K., Furneaux, K. L., Goddard, A., Lee, J. D., Mahajan, A., Oetjen, H., Read, K. A., Kaaden, N., Carpenter, L. J., Lewis, A. C., C. Plane, J. M., Saltzman, E. S., Wiedensohler, A., & Heard, D. E. (2010). The chemistry of OH and HO_2 radicals in the boundary layer over the tropical Atlantic Ocean. *Atmospheric Chemistry and Physics*, *10*, 1555–1576. https://doi.org/10.5194/acp-10-1555-2010

WHO, Air pollution [WWW Document]. WHO. https://www.who.int/health-topics/air-pollution.

Winiberg, F. A. F., Dillon, T. J., Orr, S. C., Groß, C. B. M., Bejan, I., Brumby, C. A., Evans, M.

J., Smith, S. C., Heard, D. E., & Seakins, P. W. (2016). Direct measurements of OH and other product yields from the HO_2 + $CH_3C(O)O_2$ reaction. *Atmospheric Chemistry and Physics*, *16*, 4023–4042. https://doi.org/10.5194/acp-16-4023-2016

Yan, C., Kocevska, S., & Krasnoperov, L. N. (2016). Kinetics of the Reaction of CHO Radicals with OH Studied Over the 292 – 526 K Temperature Range. *The Journal of Physical Chemistry A*, *120*, 6111–6121. https://doi.org/10.1021/acs.jpca.6b04213

Zádor, J., Turányi, T., Wirtz, K., & Pilling, M. J. (2006). Measurement and investigation of chamber radical sources in the European Photoreactor (EUPHORE). *Journal of Atmospheric Chemistry*, *55*, 147–166. https://doi.org/10.1007/s10874-006-9033-y

Zuraski, K., Hui, A. O., Grieman, F. J., Darby, E., Møller, K. H., Winiberg, F. A. F., Percival, C. J., Smarte, M. D., Okumura, M., Kjaergaard, H. G., & Sander, S. P. (2020). Acetonyl Peroxy and Hydro Peroxy Self- And Cross-Reactions: Kinetics, Mechanism, and Chaperone Enhancement from the Perspective of the Hydroxyl Radical Product. *Journal of Physical Chemistry A*, *124*, 8128–8143. https://doi.org/10.1021/acs.jpca.0c06220

List of Reactions

$O_3 + h\upsilon_{<310nm} \rightarrow O(^1D) + O_2\ (^1\Delta g)$ (R 1)

$O(^1D) + M \rightarrow O(^3P) + M$ (R 2)

$O(^1D) + H_2O \rightarrow 2\ OH$ (R 3)

$O(^3P) + O_2 \rightarrow O_3$ (R 4)

$HONO + h\upsilon_{<400nm} \rightarrow OH + NO$ (R 5)

$HO_2 + HO_2 \rightarrow H_2O_2 + O_2$ (R 6)

$H_2O_2 + h\upsilon_{<360nm} \rightarrow 2\ OH$ (R 7)

$OH + CO + O_2 \rightarrow HO_2 + CO_2$ (R 8)

$OH + RH + O_2 \rightarrow RO_2 + H_2O$ (R 9)

$OH + NO_2 + M \rightarrow HNO_3 + M$ (R 10)

$RO_2 + NO \rightarrow RO + NO_2$ (R 11)

$HO_2 + NO \rightarrow OH + NO_2$ (R 12)

$RO + O_2 \rightarrow R_{-H}{=}O + HO_2$ (R 13)

$RO_2 + RO_2 \rightarrow 2\ RO + O_2$ (R 14)

$HO_2 + HO_2 \rightarrow H_2O_2 + O_2$ (R 15)

$RO_2 + HO_2 \rightarrow ROOH + O_2$ (R 16)

$HO_2 + OH \rightarrow H_2O + O_2$ (R 17)

$RO_2 + HO_2 \rightarrow ROOH + O_2$ (R 18a)

$\rightarrow ROH + O_3$ (R 18b)

$\rightarrow RO + OH + O_2$ (R 18c)

$CH_3O_2 + HO_2 \rightarrow CH_3OOH + O_2$ (R 19a)

$\rightarrow HCHO + O_2 + H_2O$ (R 19b)

$C_2H_5O_2 + HO_2 \rightarrow C_2H_5OOH + O_2$ (R 20a)

$\rightarrow CH_3CHO + O_2 + H_2O$ (R 20b)

$CH_3C(O)O_2 + HO_2 \rightarrow CH_3C(O)O_2H + O_2$ (R 21a)

$\rightarrow CH_3C(O)OH + O_3$ (R 21b)

$\rightarrow CH_3C(O)O + OH + O_2$ (R 21c)

$CH_3C(O)CH_2O_2 + HO_2 \rightarrow CH_3C(O)CH_2OOH + O_2$ (R 22a)

$\rightarrow CH_3C(O)CH_2O + OH + O_2$ (R 22b)

$CH_3O_2 + OH \rightarrow CH_2O_2 + H_2O$ (R 23a)

$\rightarrow CH_3O + HO_2$ (R 23b)

$\rightarrow CH_3OH + O_2$ (R 23c)

$\rightarrow$ Products (R 23d)

$\rightarrow CH_3OOOH$ (R 23e)

$C_2H_5O_2 + OH \rightarrow$ Products (R 24)

$C_3H_7O_2 + OH \rightarrow$ Products (R 25)

$C_4H_9O_2 + OH \rightarrow$ Products (R 26)

$RO_2 + RO_2 \rightarrow RO + RO + O_2$ (R 27a)

$\rightarrow R_{-H}=O + ROH + O_2$ (R 27b)

$\rightarrow ROOR + O_2$ (R 27c)

$RO_2 + R'O_2 \rightarrow RO + R'O + O_2$ (R 28a)

$\rightarrow R_{-H}=O + R'OH + O_2$ (R 28b)

$\rightarrow R'_{-H}=O + ROH + O_2$ (R 28c)

$\rightarrow ROOR' + O_2$ (R 28d)

$C_2H_5O_2 + C_2H_5O_2 \rightarrow C_2H_5O + C_2H_5O + O_2$ (R 29a)

$\rightarrow C_2H_5OH + CH_3CHO + O_2$ (R 29b)

$\rightarrow C_2H_5O_2C_2H_5 + O_2$ (R 29c)

$C_2H_5O + O_2 \rightarrow CH_3CHO + HO_2$ (R 30)

OH or Cl + Reactant $\rightarrow$ Product 1 (R 31)

OH or Cl + Reference $\rightarrow$ Product 2 (R 32)

$M + e^- \rightarrow M^+ + 2\ e^-$ (R 33)

$F_2 \xrightarrow[\text{discharge}]{\text{microwave}} 2\ F$ (R 34)

$F + H_2O \rightarrow OH + HF$ (R 35)

$H_2 \xrightarrow[\text{dicharge}]{\text{microwave}} 2\ H$ (R 36)

$H + NO_2 \rightarrow OH + NO$ (R 37)

$F + D_2O \rightarrow OD + DF$ (R 38)

$CH_3OH + OH \rightarrow CH_2OH + H_2O$ (R 39)

$CH_3OH + OH \rightarrow CH_3O + H_2O$ (R 40)

$CH_2OH + O_2 \rightarrow HO_2 + CH_2O$ (R 41)

$CH_3O + O_2 \rightarrow HO_2 + CH_2O$ (R 42)

$NO_2 + OH + M \rightarrow HONO_2 + M$ (R 43)

$C_2H_5O_2 + C_2H_5O \rightarrow$ products (R 44)

$Cl_2 + h\upsilon_{351\ nm} \rightarrow 2\ Cl$ (R 45)

$C_2H_6 + Cl \rightarrow C_2H_5 + HCl$ (R 46)

$C_2H_5 + O_2 + M \rightarrow C_2H_5O_2 + M$ (R 47a)

$\rightarrow C_2H_4 + HO_2$ (R 47b)

$CH_3OH + Cl \rightarrow CH_2OH + HCl$ (R 48)

$2\ HO_2 \rightarrow H_2O_2 + O_2$ (R 49)

$C_2H_5O_2 + Cl \rightarrow$ products (R 50)

$C_2H_5O + HO_2 \rightarrow$ products (R 51)

$C_2H_5O_2 \rightarrow$ diffusion (R 52)

$HO_2 \rightarrow$ diffusion (R 53)

$C_2H_5O_2C_2H_5 + h\upsilon \rightarrow 2C_2H_5O$ (R 54)

Nomenclature

List of symbols

r’	Branching ratio	-
[A]	Concentration of species A	molecules cm^{-3}
k	Rate constant	cm^3 $molecule^{-1}s^{-1}$
k’	Pseudo-first order rate constant	s^{-1}
k_{wall}	First order rate constant for wall recombination	s^{-1}
N_x	Population of an energy level	-
A_{xy}	Einstein coefficient of spontaneous emission	s^{-1}
B_{xy}	Einstein’s coefficient	$m^3J^{-1}s^{-2}$
Q_{xy}	Rate of collisional relaxation	s^{-1}
U_υ	Spectral energy density of the laser	J $m^{-3}s$
U_v^S	Saturation energy density of the laser	J $m^{-3}s$
τ_{eff}	Fluorescence lifetime	s
τ	Lifetime of photons in a CRDS cavity	s
I_0	Incident beam intensity	-
I(t)	Intensity of the light beam after absorption	-
L	Distance between the two cavity mirrors	cm
R	Reflectivity coefficient of the mirrors	-
c	Speed of light	cm s^{-1}
α (λ)	Absorption coefficient	cm^{-1}
σ (λ)	Absorption cross section	cm^2
l	Length of the absorbent medium	cm
R_l	Ratio between the length of the cavity L and the length of the absorbent medium l	-
Kn	Knudsen number	-
L_m	Mean free path of a molecule	cm
r	Radius of the reactor	cm
< c >	Average speed of movement due to thermal agitation	m s^{-1}

Z	Frequency of collisions	s^{-1}
k_B	Boltzmann constant	$J\ K^{-1}$
T	Temperature	K
σ_{He}	Effective collision diameter of helium	m
P	Pressure	Pa or Torr
Re	Reynolds number	-
ρ	Density	$g\ cm^{-3}$
v	Velocity	$cm\ s^{-1}$
μ	Dynamic viscosity	$g\ cm^{-1}s^{-1}$
R_z	Distance between the point considered of the reactor and the axis of the tube	cm
D_{coeff}	Diffusion coefficient	cm^2s^{-1}
d	Distance between the end of the injector and the measured point	cm

Abstract

In the atmosphere, organic pollutants such as Volatile Organic Compounds (VOCs) from biogenic or anthropogenic sources are oxidized by OH radicals leading to the formation of peroxy radicals RO_2 and HO_2, which play a major role in tropospheric chemistry. Their reactivity controls the oxidative capacity of the atmosphere (cycling of reactive radicals) and the formation of tropospheric ozone and other secondary pollutants. While the reactivity of these peroxy radicals is well known in polluted environments (high NO_X concentrations), it is still poorly known in a remote environments containing low concentrations of NOx (ex: tropical forests, marine boundary layer).
The aim of the present work is to study the kinetics of some of these peroxy radicals to better understand the radical + radical reactions in clean atmosphere. Two experimental set-ups have been used. First a fast discharge flow reactor, originally designed to complement an existing photolysis cell set-up, was continued to be developed in the frame of this work. This fast flow reactor is coupled to three complementary techniques: the continuous-wave Cavity Ring-Down Spectroscopy (cw-CRDS) for the measurement of the HO_2 radical, the Laser Induced Fluorescence (LIF) for the detection of the OH radical and Mass spectrometry with Molecular Beam sampling (MB/MS) for the measurement of stable reaction products and radical species. An unexplained OH re-formation phenomenon has been observed in the previous work done during the validation of this recently developed experimental set-up. In this work, different tests were carried out to explain this OH re-formation phenomenon and will be described here. Meanwhile a laser photolysis cell coupled to a double cw-CRDS paths for the simultaneous measurements of RO_2 and HO_2 radicals was used to determine the absorption cross-section of $C_2H_5O_2$ radical, the rate constant of $C_2H_5O_2$ + HO_2, and the rate constant and branching ratios for the $C_2H_5O_2$ self-reaction.

Keywords: tropospheric chemistry, volatile organic compounds, free radical reactions, hydroxyl, mass spectroscopy, laser induced fluorescence, flash photolysis, peroxyl radicals, optical cavity spectroscopy

Résumé

Dans l'atmosphère, les polluants tels que les Composés Organiques Volatils (COV) provenant de sources biogéniques ou anthropiques sont oxydés par les radicaux OH conduisant à la formation de radicaux péroxyles RO_2 et HO_2, qui jouent un rôle majeur dans la chimie de la troposphère. Leur réactivité contrôle la capacité oxydante de l'atmosphère (cycle des radicaux) et la formation d'ozone troposphérique et d'autres polluants secondaires. Si la réactivité de ces radicaux péroxyles est bien connue dans les environnements pollués (fortes concentrations de NOx), elle est encore mal connue dans les environnements propres contenant de faibles concentrations de NOx (ex : forêts tropicales, couche limite marine).
Le but de ce travail est d'étudier la cinétique de certains de ces radicaux péroxyles afin de mieux comprendre les réactions radical + radical en atmosphère propre. Deux montages expérimentaux ont été utilisés. Tout d'abord, un réacteur à écoulement rapide, conçu à l'origine pour compléter une cellule de photolyse existante, a été utilisé dans le cadre de ce travail. Ce réacteur à écoulement rapide est couplé à trois techniques complémentaires : la spectroscopie à temps de déclin d'une cavité optique en anneau de cavité à ondes continues (cw-CRDS, continuous-wave Cavity Ring-Down Spectroscopy) pour la mesure du radical HO_2, la fluorescence induite par laser (LIF) pour la détection du radical OH et la spectrométrie de masse avec prélèvement par faisceau moléculaire (MB/MS) pour la mesure des produits de réaction stables et des espèces radicalaires. Un phénomène inexpliqué de re-formation de OH a été observé dans les travaux précédents effectués lors de la validation de ce dispositif expérimental récemment développé. Dans ce travail, différents tests ont été effectués pour expliquer ce phénomène de re-formation OH et seront décrits ici. Parallèlement, une cellule de photolyse laser couplée à une double détection par cw-CRDS pour les mesures simultanées des radicaux RO_2 et HO_2 a été utilisée pour déterminer la section efficace d'absorption du radical $C_2H_5O_2$, la constante de vitesse de la réaction $C_2H_5O_2$ + HO_2, ainsi que la constante de vitesse et les rapports de branchement pour l'« auto-réaction » de $C_2H_5O_2$.

Mots-clés : chimie troposphérique, composés organiques volatils, réactions radicalaires, hydroxyle, spectroscopie de masse, fluorescence induite par laser, photolyse éclair, radicaux peroxyles, spectroscopie à cavité optique